The influence of the land-sea breeze on coastal upwelling systems

Giles Fearon

A thesis submitted in fulfillment of the requirements
for the degree of Doctor of Philosophy

July 7, 2021

UNIVERSITY OF CAPE TOWN
IYUNIVESITHI YASEKAPA • UNIVERSITEIT VAN KAAPSTAD

Declaration of Authorship

I, Giles Fearon, declare that this thesis is a presentation of my own original research. Wherever contributions of others are involved, every effort has been made to acknowledge this clearly, with due reference to the literature. Aside from guidance from my supervisors, I have received no assistance, except as acknowledged.

Supervisors

Marcello Vichi [1,2]
Steven Herbette [3]
Jennifer Veitch [4,5]

[1] *Department of Oceanography, University of Cape Town, Rondebosch, South Africa*
[2] *Marine and Antarctic Research centre for Innovation and Sustainability (MARIS), University of Cape Town, Rondebosch, South Africa*
[3] *Laboratoire d'Océanographie Physique et Spatiale (LOPS), IUEM, Univ. Brest - CNRS - IRD - Ifremer, Brest, France*
[4] *South African Environmental Observation Network, Egagasini Node, Cape Town, South Africa*
[5] *Nansen-Tutu Centre, Marine Research Institute, Department of Oceanography, University of Cape Town, South Africa*

Abstract

Doctor of Philosophy

The influence of the land-sea breeze on coastal upwelling systems

by Giles Fearon

The land-sea breeze is resonant with the inertial response of the ocean at the critical latitude of 30° N/S, however its role in the physical and biogeochemical functioning of eastern boundary upwelling systems (EBUS) is often over-looked. Here, we present a series of 1D, 2D, and 3D numerical experiments which elucidate the drivers of diurnal-inertial variability and vertical mixing in EBUS due to land-sea breeze forcing near the critical latitude. The amplitude of the diurnal anticyclonic rotary component of the wind stress (τ^{ac0}) is shown to be a good predictor of the locally forced response. The water depth plays an important role, where for shallow water depths ($<\sim$100 m) surface oscillations are dampened and shear-driven mixing at the thermocline is reduced. Convergence/ divergence of the forced surface oscillations drive evanescent internal waves which elevate local vertical mixing above that from the forced response alone. The internal wave response is dampened by a gradually sloping bottom topography. St Helena Bay ($\sim$32.5° S), in the southern Benguela upwelling system, possesses a combination of physical characteristics which favour an enhanced response to the land-sea breeze, namely a near-critical latitude, a local enhancement of τ^{ac0}, and a tendency for the development of a shallow stratified surface layer. Here, land-sea breeze forcing contributes to large diurnal variability in sea surface temperatures (SST's). During relaxation events, mean SST's are notably reduced due to land-sea breeze-driven vertical mixing. During upwelling events, the land-sea breeze drives a net warming of inner shelf waters primarily due to enhanced retention of the deepened surface mixed layer. The deepened thermocline impacts geostrophically-driven alongshore currents within St Helena Bay, which are strengthened (weakened) during upwelling (relaxation) events. It appears likely that the land-sea breeze plays an important role in the productivity of the system.

Acknowledgements

I would like to thank the South African Environmental Observation Network (SAEON) for providing funding towards this research (2017-2018), as well as providing me with stimulating work opportunities in parallel to the completion of this thesis (2019-2020). Thank you to my primary supervisor, Marcello Vichi, for investing much time and effort in my journey through ocean science thus far. Both your high level guidance and critical eye for detail have been extremely helpful over the course of the PhD. Your assistance with additional funding is also much appreciated. To Steven Herbette, I wish to thank you for your valuable insights which were crucial in shaping some of the main ideas of the PhD. Your assistance in facilitating two visits to Brest, France, were particularly instrumental. I wish to acknowledge ICEMASA, LabexMER and the French Embassy in South Africa for providing travel grants for these visits. To Jennifer Veitch, I am very lucky to have had you play the dual role of both a PhD supervisor and my work manager at SAEON. Your assistance and encouragement on both fronts is much appreciated.

Thank you to Charine Collins for facilitating my initial engagement with SAEON and for providing supervision during the early stages of this research. A sincere thank you to Gildas Cambon for taking a keen interest in my research, and for always being available to assist with any and all of my CROCO related questions. I wish to express my gratitude to Grant Pitcher for some interesting discussions and for making observational data available which proved to be extremely useful. I am indebted to Drew Lucas for making his Wirewalker mooring data available for my research- these data motivated many questions which are addressed in this PhD. I would like to thank Florian Lemarié for making his 1D CROCO python code available. I am grateful to the Department of Environment Forestry and Fisheries (DEFF) for making the St Helena Bay Monitoring Line Data available. Thank you to the Climate Systems Analysis Group (CSAG) for the provision of their WRF atmospheric model output, and specifically Chris Lennard and Pierre Kloppers for their assistance in this regard. This research benefitted from the provision of bathymetric data from the South African Navy Hydrographic Office (SANHO). Computations were performed using facilities provided by the University of Cape Town's ICTS High

Performance Computing team: hpc.uct.ac.za.

I would like to thank everyone at the Oceanography Department at UCT for creating an enjoyable working environment. Thanks to my old office partner, Marie-Lou Bachèlery, for our interesting chats and for your assistance with CROCO in the early days. A big thank you to my current SAEON colleagues, Matt Carr and Cristina Russo, for your friendship and encouragement over the last couple of years.

Lastly, and most importantly, I would like to thank my wife, Shelley, for sharing this journey with me. Your love and support has been a well of stability through the highs and lows of the last four years. I look forward to our many journeys to come.

Contents

List of Figures

List of Tables

Chapter 1

Introduction

Eastern Boundary Upwelling Systems (EBUS) are regions along the eastern land boundaries of the Pacific and Atlantic Oceans where the upwelling of cold nutrient-rich waters to the euphotic zone promotes phytoplankton growth. The four major EBUS are located along the coastal regions of California/Oregon/Washington in the North Pacific, Peru and Chile in the South Pacific, northwest Africa and Portugal in the North Atlantic, and South Africa and Namibia in the South Atlantic (Figure 1.1). Although they account for less than 1% of the ocean surface area, coastal upwelling systems are responsible for about a third of global primary productivity (Pauly and Christensen, 1995). The productivity of these systems is largely understood in terms of the upwelling/relaxation paradigm, where nutrients are upwelled to the coastal zone during periods of sustained equatorward alongshore winds, while retention mechanisms during wind relaxation are important for the accumulation of high biomass coastal blooms (Pitcher et al., 2010). Diurnal wind variability associated with the land-sea breeze, common to all EBUS, is often assumed to be of lower importance for understanding the productivity of these systems, relative to the sub-diurnal wind variability governing upwelling dynamics.

Some observational evidence has suggested that the land-sea breeze could play an important role in nutrient enrichment of the surface layer in upwelling systems through diapycnal mixing, particularly near the critical latitude of 30°N/S where the land-sea breeze is near-resonant with the inertial response of the ocean (Aguiar-González et al., 2011; Lucas et al., 2014). The critical latitude of 30°N/S is shown in Figure 1.1, highlighting its intersection with all four major EBUS. The influence

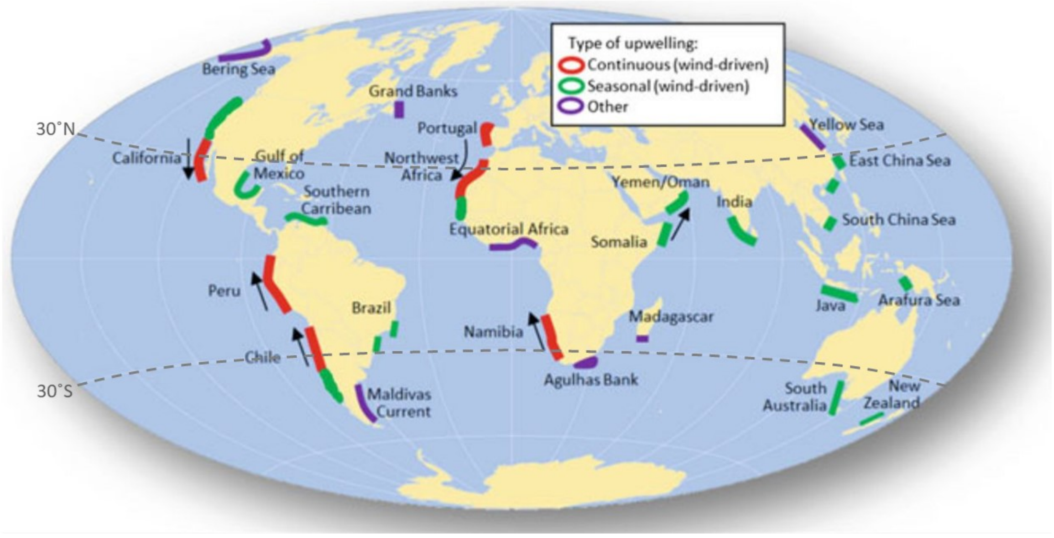

FIGURE 1.1: Locations of significant coastal upwelling systems (adapted from Kämpf and Chapman, 2016). The four major EBUS are shown in red. The black arrows indicate the prevailing wind direction. The grey dotted lines denote the critical latitude of 30°N/S, where the land-sea breeze is resonant with the inertial response of the ocean.

of the land-sea breeze within the context of the physical and biological functioning of EBUS however remains largely unknown. The over-arching aim of this thesis is to improve our understanding of the physical response of EBUS to land-sea breeze forcing near the critical latitude, and consider how these processes may impact the productivity of these systems.

In this chapter we provide a brief overview of upwelling dynamics in EBUS (Section 1.1), discuss processes associated with the land-sea breeze near the critical latitude for diurnal-inertial resonance (Section 1.2), and introduce St Helena Bay, in the southern Benguela upwelling system, as an appropriate case study for a detailed assessment of these processes (Section 1.3). The study objectives are then laid out in Section 1.4.

It is perhaps necessary to clarify at this point how we refer to time scales of wind-driven phenomena in this thesis. We use sub- and super-diurnal variability to refer to variability with frequencies (as opposed to timescales) below and above the diurnal frequency, respectively. Similarly, sub- and super-inertial variability refers to variability with frequencies below and above the local inertial frequency, respectively.

1.1 Eastern Boundary Upwelling Systems (EBUS)

Surface wind stress injects momentum into the upper few tens of meters of the ocean through internal fluid friction, parameterised as vertical eddy viscosity (K_{Mv}). For timescales longer than a day, the vertical momentum transfer is greatly affected by the Coriolis parameter, a local measure of Earth's effective rotation:

$$f = 2\Omega \sin \phi \tag{1.1}$$

where Ω is the angular frequency of the Earth rotating about its axis and ϕ is the latitude. According to classical Ekman theory (Ekman, 1905), a constant wind stress ($\overrightarrow{\tau_s}$) acting on an infinite homogenous ocean generates a depth-veering current resulting in vertically integrated transport ($\overrightarrow{M_E}$) which is exactly perpendicular to the left (right) of the surface wind stress in the southern (northern) hemisphere. In the case of a sustained surface wind stress acting parallel to a north-south aligned coastline (τ_s^y), the cross-shore surface layer Ekman transport per unit length of coastline (M_E^x) can be estimated as:

$$M_E^x = \frac{\tau_s^y}{\rho f} \tag{1.2}$$

where ρ is the water density. Continuity at the coastal boundary dictates that offshore surface transport must be compensated by onshore subsurface transport, and the consequent upwelling of subsurface water at the coast.

Large-scale wind variability in EBUS is primarily governed by atmospheric pressure gradients set up by permanent but seasonally migrating subtropical high pressure systems over the Atlantic and Pacific oceans, as well as the land-based thermal low pressure systems which develop to the east of the oceanic highs (García-Reyes et al., 2013). The result is predominantly equatorward winds which blow parallel to the mostly north-south aligned coastlines of EBUS (Figure 1.1). Equation 1.2 dictates that equatorward alongshore wind stress drives westward (offshore) surface layer transport in both hemispheres, resulting in the upwelling of cold nutrient rich subsurface waters which support the primary productivity of these systems. The seasonal variability in the winds is driven by the seasonality of the oceanic and terrestrial pressure systems. In the higher latitude regions of EBUS, summer months are characterised by stronger alongshore winds, increased upwelling and enhanced productivity, while lower latitudes display less seasonality (Chavez and Messié, 2009).

The interaction of the large-scale atmospheric circulation with the coast can result in high spatial and temporal variability in the nearshore winds, with consequences for upwelling dynamics. In general, nearshore winds tend to be lower than those offshore, resulting in cyclonic wind stress curl in the nearshore regions of EBUS. The mechanisms driving the so-called wind drop-off at the coast include local orographic features, coastline shape and sea surface temperature gradients (Renault et al., 2016). Although the nearshore Ekman transport is reduced due to the wind drop-off, continuity dictates that the local divergence of Ekman transport ($\nabla \cdot \overrightarrow{M_E}$) must be compensated by a vertical velocity known as Ekman pumping (w_E), which can be computed directly from the wind stress curl:

$$w_E = \nabla \times -\frac{\overrightarrow{\tau_s}}{\rho f} \tag{1.3}$$

Both the alongshore wind stress and wind stress curl induced by the wind drop-off play important roles in wind-driven upwelling dynamics of EBUS (e.g. Capet et al., 2004) as well as the overall productivity of these systems (Rykaczewski and Checkley, 2008).

In addition to wind-driven processes, upwelling and coastal circulation is largely controlled by local topographic features. The orientation of the coastline relative to the wind stress governs offshore Ekman transport, while narrower shelf widths enhance upwelling. Upwelling fronts are associated with strong equatorward jets, in geostrophic balance with the steep horizontal pressure gradients set up by the upwelled waters. Divergence of the equatorward jet downstream of capes can further enhance shelf-edge upwelling (e.g. Veitch et al., 2010). The spatial variability in both the winds and topography within EBUS give rise to high spatial variability in upwelling and productivity within these systems. However, increased upwelling of subsurface waters does not generally translate into locally enhanced productivity (Gruber et al., 2011). For example, the Lüderitz upwelling cell is the location of greatest upwelling in the southern Benguela upwelling system, but is coincident with a local minimum in coastal productivity, explained by increased turbulence and offshore advective losses associated with upwelling (Demarcq et al., 2007). The development of high biomass coastal blooms requires the retention of upwelled waters during wind relaxation, so that the upwelled nutrients can be efficiently utilised. Such regions are often found in bays formed by capes, where poleward inner shelf counter-currents may coexist with equatorward offshore flow during wind relaxation, promoting the retention and accumulation of phytoplankton blooms (Pitcher et al., 2010).

1.2 The influence of the land-sea breeze

1.2.1 Inertial oscillations

Ekman (1905) showed that the response of the ocean to a surface wind stress takes the form of both rotary and non-rotary components, with the wind-driven dynamics described in Section 1.1 corresponding to the non-rotary response to a sustained wind. The rotary response refers to inertial oscillations (Equations 1.4 and 1.5), which can be described as anticyclonic circular motions with a frequency equal to the Coriolis parameter f:

$$\frac{\partial u}{\partial t} = fv \tag{1.4}$$

$$\frac{\partial v}{\partial t} = -fu \tag{1.5}$$

While inertial oscillations become damped when the wind forcing remains constant over the full duration of an inertial period, they can be excited by shorter duration pulses in wind stress. In the case of a constant wind stress, a forcing duration of half the inertial period (less than one day at all latitudes by definition) is optimal for imparting energy into the inertial response (Pollard, 1970). Impulsive wind forcing associated with the passage of storm events is a common mechanism for the generation of inertial motions, which are often observed in their wake (e.g. D'Asaro et al., 1995). The most efficient way of imparting energy into surface mixed layer inertial currents is in the form of an anticyclonically rotating wind stress with a frequency ω equal to the inertial frequency f, as in this case the wind stress and surface current vectors are always aligned (Pollard and Millard, 1970; D'Asaro, 1985; Alford, 2001).

1.2.2 Diurnal-inertial resonance

At latitudes of 30° N/S the inertial frequency is diurnal (Equation 1.1), leading to resonance between the inertial response of the ocean and any forcing with a diurnal frequency; a phenomenon known as diurnal-inertial resonance (Craig, 1989; Simpson et al., 2002). Such a mechanism can be found in the land-sea breeze, driven by differential heating over the land and the ocean. During the day, the land surface warms more rapidly than over the adjacent ocean and the resulting air density gradient drives an onshore wind. Similarly, the land cools more rapidly at night, setting up an offshore wind. The land-sea breeze phenomenon results in statistically significant wind variability at the diurnal frequency along most of the world's coastlines, and is detectable several hundred kilometres from the coast (Gille, 2003; Gille, 2005). Near the critical latitude of 30° N/S, land-sea breeze forcing can give rise to significant amplitude inertial oscillations due to the continual injection of near-inertial energy into the surface mixed layer. Indeed, many documented observations of surface rotary diurnal currents in EBUS have been attributed to land-sea breeze wind forcing (Hyder et al., 2011, and references therein). It should however be noted that the phenomenon of diurnal-inertial resonance is present in all regions where a periodic forcing is at or near the local inertial frequency, including tidally dominated systems near 74.5° N/S where the inertial frequency is equal to the M_2 tidal constituent (e.g. Furevik and Foldvik, 1996).

1.2.3 The land boundary effect

In proximity to a land boundary, near-inertial motions commonly exhibit a two layer vertical current structure, with a 180° phase shift between surface and subsurface layers (e.g. Millot and Crépon, 1981; Shearman, 2005; Simpson et al., 2002; Lucas et al., 2014). This phenomenon has in part been explained using an analytical model for the first order coast-normal surface elevation gradient response imposed by the barotropic no-flow condition perpendicular to the land boundary (Craig, 1989; Simpson et al., 2002). Considering a coastline along the y axis, a cross-shore wind stress (τ_s^x), and ignoring bottom friction, the so-called 'Craig approximation' is expressed as (Craig, 1989):

$$\frac{\partial \eta}{\partial x} = \frac{\tau_s^x}{\rho g H} \tag{1.6}$$

The implication of Equation 1.6 is that the cross-shore pressure gradient force induced by the surface slope is in the opposite direction to the cross-shore component of the wind stress. The pressure gradient force acts throughout the water column while the surface stress acts on the surface mixed layer alone, resulting in surface and subsurface currents in the opposite direction and a net effect of zero depth-averaged coast-normal transport. Simpson et al. (2002) extended the 'Craig approximation' to include the effect of the alongshore component of a rotating surface stress vector, which serves to amplify the barotropic response in the case of anticyclonically rotating winds near the critical latitude. While the 'Craig approximation' is able to provide an explanation for the 180° phase shift between surface and subsurface oscillations near a land boundary, it should be highlighted that the two layer current structure produced in this way is not a true first baroclinic mode, but rather the superposition of the forced surface mixed layer response and the opposing barotropic pressure gradient. Indeed, the two layer current structure can be produced in a vertically homogeneous water column (Pettigrew, 1980; Chen et al., 2017). Throughout this thesis we refer to the nearshore ocean response as described in this paragraph as the 'forced response'.

1.2.4 Coastally generated internal waves

Once inertial motions are excited in the surface layer by an applied wind stress, horizontal convergences and divergences then pump the stratified base of the mixed layer, thereby initiating near-inertial internal waves which can propagate away from the generation zone (Alford et al., 2016). Near-inertial motions near coastlines therefore result from the combined effect of the locally forced response and the offshore propagating internal wave response generated by vertical displacements of the pycnocline due to convergence/divergence at the coastal boundary (Millot and Crépon, 1981; Tintoré et al., 1995; Orlić and Pasarić, 2011; Kelly, 2019). The propagation of the internal wave energy away from the coastline is dictated by the dispersion relation for Poincare waves, which must be satisfied for propagating wave solutions to exist:

$$\omega^2 = f^2 + c_1^2 k^2 \tag{1.7}$$

where ω is the frequency of the waves, k is the horizontal wavenumber and c_1 is the phase speed of the first baroclinic mode internal wave. An implication of Equation 1.7 is that displacements of the pycnocline forced by the land-sea breeze, which will by definition have a diurnal frequency, are able to propagate freely away from the generation zone only for latitudes equatorward of the critical latitude of 30° N/S, where $f < \omega$ (Zhang et al., 2010). Poleward of 30° N/S, internal waves are evanescent and the energy imparted to the ocean by the land-sea breeze must be dissipated locally.

1.2.5 Diapycnal mixing

Both the locally forced response and the first baroclinic mode internal wave response to land-sea breeze forcing introduce vertical current profiles which enhance shear at the pycnocline, leading to turbulence and diapycnal mixing. Observations of wind-driven inertial oscillations in shallow stratified shelf seas have been shown to produce bursts of enhanced shear at the inertial frequency, termed ‘shear spikes’, which promote vertical mixing and deepening of the thermocline (Burchard and Rippeth, 2009; Lincoln et al., 2016). The analytical shear production theory of Burchard and Rippeth (2009) has been shown to provide a good explanation for these observations. For a two layer system, the theory dictates that vertical shear between the two layers will increase when the shear vector is aligned with the surface wind stress and/or bottom stress, while interfacial mixing between the layers reduces shear production. 'Shear spikes' are produced when the inertial oscillations and the sub-inertial Ekman transport become aligned. Such 'shear spikes' have been further shown to contribute significantly to diapycnal mixing, driving surface layer nutrient availability and therefore the primary productivity in shelf seas (Williams et al., 2013). The theory of Burchard and Rippeth (2009) is however yet to be applied in the context of diurnal-inertial resonance forced by the land-sea breeze.

1.2.6 Modelling the inertial response

As inertial oscillations have been observed to be tightly coupled to the local wind forcing, salient features of the observations have been reasonably reproduced by linearly damped slab models of the surface layer (e.g. Pollard and Millard, 1970; Pollard, 1980; Alford, 2001; Jarosz et al., 2007). Such models however do not account for the deepening of the surface layer due to diapycnal mixing and explicitly ignore subsurface effects. 1D-vertical models equipped with a vertical turbulence closure scheme for the parameterisation of vertical mixing have been employed to study the surface layer inertial response of the ocean, but are limited in their ability to reproduce the first baroclinic mode vertical current structure of nearshore oscillations, and lack vertical mixing due to the internal wave response (Xing et al., 2004; Zhang et al., 2010). Hyder et al. (2011) showed that a land-sea breeze forced 1D-vertical model including the 'Craig approximation' is able to qualitatively reproduce the observed 180° phase shift between surface and subsurface layer inertial oscillations off the Namibian coastline in 175 m water depth. The extent to which the 'Craig approximation' can be used to describe the forced response of the coastal ocean to land-sea breeze forcing however remains largely untested. 2D-vertical models are capable of including both the forced and cross-shore internal wave response in the presence of a land boundary, and have proven useful in providing insight into the cross-shore variability in the inertial response to an impulsive wind stress (e.g. Tintoré et al., 1995; Chen and Xie, 1997; Xing et al., 2004; Chen et al., 2017). The 3D numerical experiments of Zhang et al. (2010) elucidated the latitudinal dependence in the inertial response and associated diapycnal mixing due to land-sea breeze forcing. They found that diapycnal mixing is maximised near the critical latitude of 30° N/S, where internal wave energy is trapped at the coastline due to the low group speed of Poincare waves, while mixing is reduced at lower latitudes although energy is able to propagate offshore in the form of Poincare waves. Quantifying the relative contribution of the forced and the internal wave response on near-inertial motions and diapycnal mixing is complicated by their similar vertical current structures and frequencies. Analytical models have however been used to separate the forced and wave motions for estimates of wind work and wave radiation (Kelly, 2019).

1.2.7 Relevance to EBUS

Figure 1.1 highlights that all four major EBUS are intersected by the critical latitude of 30° N/S. As these regions are known to be characterised by a pronounced land-sea breeze, the phenomena described above are expected to be present in these systems. Indeed, diapycnal mixing associated with land-sea breeze forcing near the critical latitude has been identified as a potential mechanism for enhanced nutrient flux to the surface layer in EBUS (e.g. Fawcett et al., 2008; Aguiar-González et al., 2011; Nam and Send, 2013; Lucas et al., 2014). The overall contribution of the land-sea breeze to primary productivity within these systems however remains largely unknown. Perhaps the clearest demonstration of primary productivity enhancement by diurnal winds are the nearshore measurements of Lucas et al. (2014) in St Helena Bay, located in the southern Benguela upwelling system (Figure 1.2). St Helena Bay is used as a case study in this thesis and is introduced in more detail in Section 1.3. A further consequence of enhanced diapycnal mixing within the context of EBUS is the effect on pressure gradients due to a significantly altered vertical water column structure. Land-sea breeze forcing near the critical latitude has been observed to enhance sub-diurnal alongshore flows in EBUS (Nam and Send, 2013), however the effect of land-sea breeze forcing on sub-inertial processes in EBUS remains largely unstudied.

1.3 St Helena Bay as a case study

Here we provide a brief overview of the relevant dynamics of the St Helena Bay, located in the southern Benguela EBUS, thereby motivating its selection as the case study for this thesis.

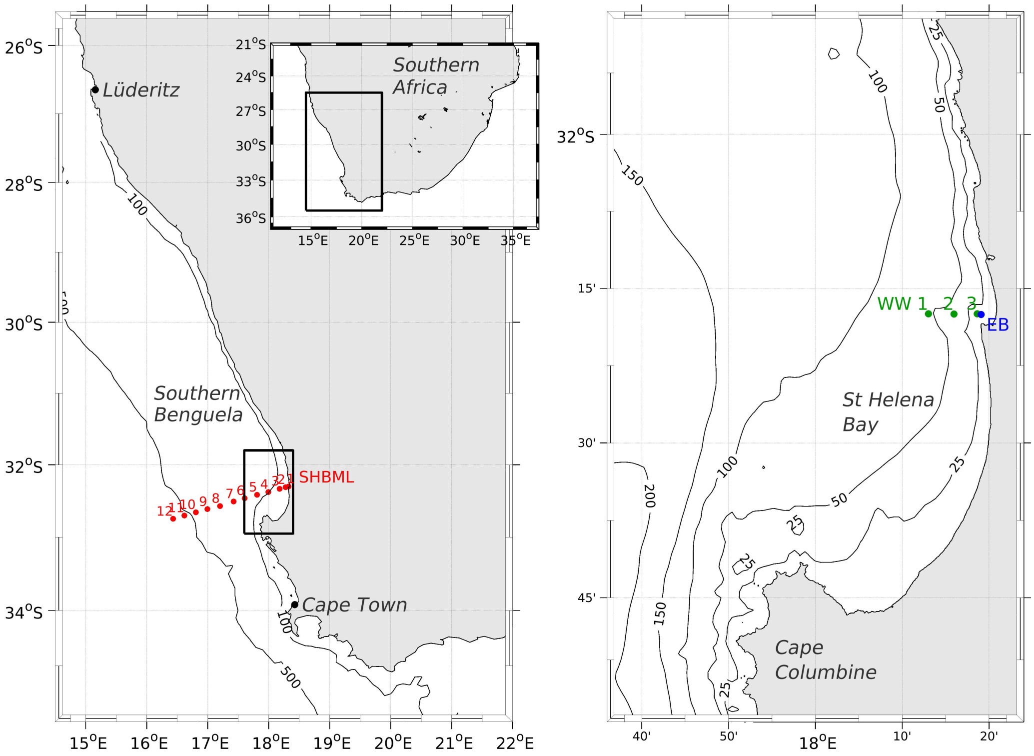

FIGURE 1.2: Locality map for St Helena Bay and various previously published in-situ observational datasets used in this thesis. The red dots denote the St Helena Bay Monitoring Line (SHBML, Lamont et al., 2015), the green dots provide locations of Wirewalker moorings (WW, Lucas et al., 2014), while the blue dot represents the Elands Bay fixed mooring (EB, Pitcher et al., 2014). Bathymetric contours are derived from digital navigational charts for the region provided by the Hydrographer of the SA Navy.

1.3.1 Regional context

The southern Benguela upwelling system extends along the west coast of southern Africa, with a natural northern boundary defined by the perennial upwelling cell at Lüderitz (Figure 1.2). The offshore waters of the southern Benguela are warm, saline and highly turbulent due to the intrusion of rings and filaments emanating from the Agulhas retroflection, south of Cape Town (Garzoli and Gordon, 1996; Veitch and Penven, 2017). This produces a perennial cross-shelf density front which defines the offshore extent of the upwelling zone, sometimes referred to as the oceanic front (e.g. Lamont et al., 2015). The nearshore is characterised by strong upwelling events which coincide with enhanced equatorward winds, typically occurring during austral spring and summer at intervals of 3–10 days (Nelson and Hutchings, 1983; Shannon, 1985; Shannon and Nelson, 1996). Spatial variability in coastal upwelling within the region is high, characterised by a number of discrete cells of enhanced activity, driven by a combination of enhanced cyclonic wind stress curl and/or wind stress, coastline orientation, and the narrowing of the continental shelf (e.g. Lutjeharms and Meeuwis, 1987; Shannon and Nelson, 1996). Upwelling cells within the southern Benguela have been identified at Cape Peninsula (∼34° S), Cape Columbine (∼33° S), Namaqualand (∼30° S) and Lüderitz (∼27° S). The upwelling of cold water into the nearshore sets up a shelf edge front which extends along the steep shelf edge from the Cape Peninsula to Cape Columbine. Associated with the front is the Goodhope Jet, a strong equatorward current in geostrophic balance with the cross-shore pressure gradient set up by the front (Strub et al., 1998; Veitch and Penven, 2017). Subsurface flow over the continental shelf in the region is predominantly poleward, which has been linked to the nearshore negative wind stress curl through the Sverdrup balance (Veitch et al., 2010). North of Cape Columbine, the Goodhope Jet tends to bifurcate due to shelf widening, resulting in offshore and alongshore components (Shannon and Nelson, 1996), the latter corresponding to the Columbine Jet which effectively defines a dynamic boundary between the nearshore waters of St Helena Bay and those offshore (Lamont et al., 2015).

1.3.2 Inner shelf dynamics

Figure 1.2 shows St Helena Bay to be the largest embayment on the west coast of southern Africa, defined by the prominent Cape Columbine headland to the south and the significant broadening of the continental shelf to the north. Periods of sustained alongshore winds lead to upwelling along a narrow belt on the eastern periphery of the bay and the formation of an inner shelf upwelling front (Jury, 1985; Taunton-Clark, 1985). Surface flow on the inner shelf during active upwelling is typically equatorward, changing to onshore and poleward flow during periods of wind relaxation (Fawcett et al., 2008). The Columbine Jet at the western periphery of the bay physically separates coastal waters from those offshore, leading to a cyclonic retentive flow pattern within the bay during relaxation events. Penven et al. (2000) showed that a barotropic model forced by an equatorward wind stress is able to produce cyclonic circulation in St Helena Bay, regulated by a balance between bottom friction and advection. Further numerical experiments have however indicated that stratification is also important in generating a poleward inshore current, as inner shelf horizontal pressure gradients originally set up by upwelling reverse during the onset of wind relaxation (Viljoen, 2006).

The retentive circulation within St Helena Bay during wind relaxation provides conditions which are conducive for the development of high biomass coastal blooms, as evidenced by a clear peak in coastal chlorophyll derived from satellite data (Weeks et al., 2006; Demarcq et al., 2007). The phytoplankton blooms nourish a productive zooplankton community, thereby supporting several fish species which spawn on the Agulhas Bank and are transported by the aforementioned alongshore jet currents to the west coast, with St Helena Bay being the main nursery ground (Shelton and Hutchings, 1982; Ragoasha et al., 2019). While most phytoplankton blooms make a positive contribution to the ecosystem, St Helena Bay is also particularly susceptible to the development of Harmful Algal Blooms (HABs) (Pitcher and Calder, 2000). HABs can occur as a result of the decay of high biomass non-toxic blooms within the shallow nearshore environment, leading to anoxia in bottom waters through microbial respiration (Pitcher and Probyn, 2011; Pitcher et al., 2014), as well as directly due to the toxigenicity of certain species (e.g. Hubbart et al., 2012). Negative impacts of HABs can be severe, including mass mortality of fish, shellfish, marine mammals, seabirds and other animals, with significant commercial implications (e.g. Cockcroft et al., 2000).

The development of phytoplankton blooms within St Helena Bay has been shown to be closely linked to the prevailing winds which govern the sub-inertial hydrodynamic processes on the inner shelf (Pitcher et al., 1998; Fawcett et al., 2007). The highest number of blooms occur in late austral summer and autumn, the latter part of the upwelling season, which is characterised by diminished upwelling and extended relaxation events (Pitcher and Calder, 2000). Blooms tend to develop along the inner shelf upwelling front and are advected onshore and poleward during relaxation events, in accordance with the bay-scale circulation already described (Pitcher and Boyd, 1996; Pitcher et al., 1998). The retentive properties of the bay in conjunction with solar irradiance allow for the development of a warm shallow stratified surface layer, providing conditions particularly favourable for productivity (Pitcher and Nelson, 2006; Fawcett et al., 2007).

1.3.3 Evidence for the influence of the land-sea breeze

Analysis of land-based wind measurements near Lamberts Bay indicate that St Helena Bay is exposed to significant diurnal wind variability, particularly during upwelling favourable conditions, and that the winds follow an elliptical anticlockwise (anticyclonic) rotating path, with the major ellipse axis aligned from southwest to northeast (Fawcett et al., 2008; Lucas et al., 2014). Further evidence for strong diurnal wind variability over the Southern Benguela has been found in land-based meteorological stations along the Namibian coastline as well as scatterometer satellite wind observations (Hyder et al., 2011). A detailed assessment of the spatial and seasonal variability in the land-sea breeze over St Helena Bay is however still outstanding. Given that St Helena Bay is located at a latitude of $\sim$32.5° S (inertial period of $\sim$22 hr), resonance between the diurnal periodicity in the wind forcing and the inertial response is to be expected. Indeed, Acoustic Doppler Current Profiler (ADCP) measurements indicate the ubiquitous presence of energetic inertial oscillations (amplitude $>$0.5 m s^{-1}) within the bay, driven by diurnal-inertial resonance (Fawcett et al., 2008; Lucas et al., 2014). The energetic inertial response of the ocean is embedded within the sub-inertial processes which are most commonly understood to govern bloom development within St Helena Bay, as described in Section 1.3.2.

Figure 1.3 presents a subset of the observations of Lucas et al. (2014), revisited in this thesis for the validation and interpretation of numerical experiments. The onset of upwelling-favourable winds with strong diurnal variability is shown to drive surface and subsurface inertial oscillations with opposite phase, leading to shear-driven diapycnal mixing, deepening of the thermocline and cooling of surface waters. The observed enhancement of productivity over the event, as revealed through Chl *a* fluorescence, was attributed in part to diapycnal nutrient flux induced by the inertial response of the ocean to the land-sea breeze. This suggests that the land-sea breeze could play a major role in bloom phenomenology in the bay. Many processes are however at play, and the relative importance of each is not easily discernible from the observations. For example, the spatial variability in the inertial oscillations is unknown, while diapycnal mixing associated with these motions cannot be computed directly from the observations alone. Furthermore, it is not clear to what

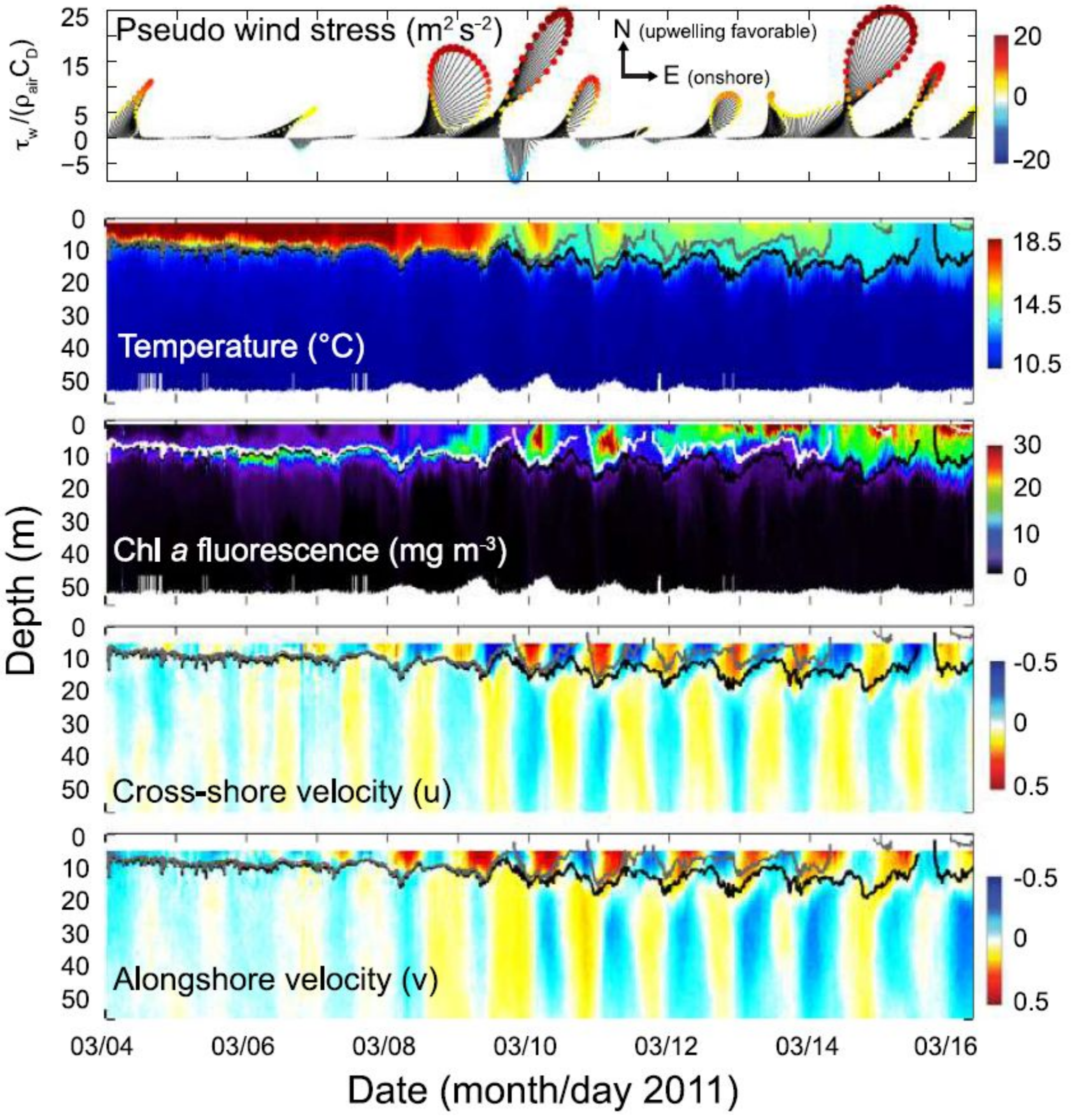

FIGURE 1.3: A 12.5 day time-series of (a) wind stress, (b) temperature, (c) Chl *a* fluorescence, (d) cross-shore, and (e) alongshore velocity at the outer wirewalker mooring ('WW' Station 1 in Figure 1.2) (from Lucas et al. (2014)).

extent the locally forced response and internal wave response contribute to the observed diurnal-inertial variability in currents and associated shear-driven diapycnal mixing. A further complication is that it is impossible to discern the relative contributions of both sub-inertial and super-inertial advection on the observed tracers (i.e. temperature and Chl *a* fluorescence). Numerical models represent useful tools for addressing some of these issues, thereby building on the insights already gained through the observations.

1.3.4 Modelling the dynamics of St Helena Bay

Previous modelling studies have been valuable in elucidating various dynamic processes of the southern Benguela upwelling system. As time-averaged wind stress is sufficient for modelling net upwelling, monthly climatological atmospheric forcing has been appropriate for the modelling of sub-inertial processes (e.g. Penven et al., 2001; Veitch et al., 2010). Modelling studies aimed at elucidating dynamics specific to St Helena Bay have focused on processes governing the return current on the inner shelf, and have as such been forced with constant winds (Penven et al., 2000) or filtered winds to remove the diurnal variability (Viljoen, 2006). Such studies therefore explicitly excluded the influence of the land-sea breeze. To our knowledge no previous modelling studies have considered the effect of the land-sea breeze on the dynamics of the system.

The strong dependence of bloom dynamics on local wind-driven phenomena suggest that hydrodynamic models are likely to be very useful in predicting the timing, location and duration of bloom events in St Helena Bay (Pitcher and Weeks, 2006). Preliminary efforts towards this goal, using the Delft3D-FLOW numerical model, indicated that the salient event-scale upwelling/relaxation dynamics were included in the model (Viljoen and Monteiro, 2004). The simulations were however limited by the availability of realistic boundary conditions and space varying atmospheric forcing. The development of an appropriately configured regional ocean model, forced with boundary conditions from a larger scale model and high resolution atmospheric forcing, has been actively recommended for the St Helena Bay region (Viljoen and Monteiro, 2004; Bernard et al., 2006). The development of such a model configuration would be beneficial both for addressing outstanding research questions and assisting in operational requirements for the effective management of the coastal environment. This research effort is however still outstanding.

1.4 Study objectives

This chapter has identified various gaps in our knowledge with respect to how the land-sea breeze may impact the physical and biogeochemical dynamics of EBUS near the critical latitude of 30°N/S. While limited observations have provided some insights into the possible influence of these processes, their importance with respect to the overall functioning of EBUS remains relatively unstudied. The objective of this thesis is to improve our understanding of the physical response of EBUS to land-sea breeze forcing near the critical latitude. To this end we present a series of numerical experiments of increasing complexity, starting with a 1D-vertical model, then moving to a 2D-vertical model, and finally adopting a realistically configured 3D model. Each set of experiments is designed to illustrate different processes of interest, thereby highlighting their importance within the context of EBUS. We use St Helena Bay as a case study throughout and rely heavily on the observations of Lucas et al. (2014) as a ground truth for comparison with the numerical experiments. Additional longer term observations are further used for the assessment of sub-inertial processes in the realistically configured 3D model.

In Chapter 2 we describe various in-situ, global ocean reanalysis and atmospheric forcing datasets used in the configuration and validation of a 3D hydrodynamic model designed to capture both the sub-inertial and super-inertial dynamics of the southern Benguela. The datasets and methods presented in this chapter provide a useful reference for the following chapters which are aimed at addressing a number of scientific questions, as outlined below.

In Chapter 3 we begin by considering the reduced physics of a 1D-vertical model, allowing us to isolate the locally forced response of the ocean to land-sea breeze forcing. Questions we address in this chapter are:

- What are the key physical drivers which lead to an enhancement of the forced inertial response to the land-sea breeze?
- How do these physical drivers relate to shear-driven diapycnal mixing?
- To what extent can the observations of Lucas et al. (2014) be explained by the limited physics of the 1D-vertical model, and what processes are missing?
- What is the spatial and seasonal variability in the land-sea breeze over the southern Benguela, and what inferences can be made from the 1D model experiments with respect to the spatial and seasonal variability in the forced response?

In Chapter 4 we use a 2D-vertical model to build on the fundamental insights gained with the 1D-vertical model. The introduction of the cross-shore dimension allows for the analysis of internal wave generation at the coastal boundary, as well as the inclusion of sub-inertial upwelling in the model. Questions we address in this chapter are:

- Is the internal wave response to land-sea breeze forcing generated in the 2D-vertical model configuration?
- What are the key drivers of the internal wave response to the land-sea breeze?
- What is the cross-shore variability in near-inertial currents and diapycnal mixing in response to the land-sea breeze, and how does this compare with the locally forced response predicted by the 1D model?
- How does the response to the land-sea breeze influence sub-inertial upwelling?
- How do the 2D model experiments improve our understanding of the observations of Lucas et al. (2014)?

In Chapter 5 we carry out numerical experiments with the realistically configured and validated 3D model of the southern Benguela to isolate the influence of the land-sea breeze on driving variability of the system. Questions we address in this chapter are:

- What is the spatial variability in the ocean response to the land-sea breeze over the southern Benguela, and is St Helena Bay anomalous in this respect?
- How does the ocean response to the land-sea breeze contribute to driving diurnal variability in sea surface temperatures in the region?
- To what extent can the event-scale diapycnal mixing dynamics of the system be explained in terms of the reduced physics experiments?
- How does the land-sea breeze impact the longer term vertical water water column structure and circulation?

Chapter 6 provides a summary of the main findings of the previous chapters, and identifies future research questions.

Chapter 2

A shelf model of the southern Benguela

2.1 Introduction

In this chapter we present the configuration and validation of a shelf model of the southern Benguela. A dynamical downscaling approach is adopted, whereby boundary conditions for the model are obtained from a global ocean reanalysis product and atmospheric forcing is obtained from a high resolution ($\sim$3 km) atmospheric model for the region. The model is comprised of a $\sim$1 km resolution child domain over St Helena Bay nested with a $\sim$3 km parent domain. The model validation explores the extent to which the model captures both the sub-inertial and super-inertial variability within St Helena Bay. Both time-scales are important within the context of this study as the inertial response to the land-sea breeze is dependent on the longer term vertical water column structure and circulation which is in turn affected by sub-inertial processes. Preference is given to in-situ data over satellite observations for the validation of the model owing to the nearshore and high-frequency nature of the processes of interest. The importance of diurnal wind variability in driving inertial currents and associated diapycnal mixing in St Helena Bay is highlighted by comparing model output from simulations forced with both hourly and daily averaged winds. This comparison provides further motivation for a detailed analysis of the processes at play, as laid out in the following chapters. The model configuration presented in this chapter also forms the basis for the 3D experiments presented in

Chapter 5.

Section 2.2 describes the various previously published in-situ observations used to assess the model performance (observation locations are shown in Figure 1.2). A description of the model is provided in Section 2.3, while Section 2.4 describes the model grid, bathymetry, atmospheric forcing and lateral boundary conditions. A formal assessment of the model is provided in Section 2.5, while a synthesis of the results is provided in Section 2.6.

2.2 In-situ data for model assessment

The hydrographic variability across the continental shelf has been informed from approximately monthly Conductivity-Temperature-Depth (CTD) casts along the St Helena Bay Monitoring Line (SHBML) from March 2000 to August 2017 (Oceans and Coastal Research, 2017). The transect is comprised of twelve stations orientated approximately perpendicular to the isobaths off Elands Bay (red points labelled 1-12 in Figure 1.2). A detailed description of the data is provided in Lamont et al. (2015). For this study, the measurements from all available cruises were used to calculate monthly climatologies of temperature and salinity at each station on a 1 m vertical grid, providing insight into the seasonal and spatial variability of the water column structure accross the continental shelf.

A fixed mooring in Eland's Bay provides a time-series of temperature, salinity, dissolved oxygen and chlorophyll fluorescence near the surface ($\sim$5 m water depth) and at the seabed ($\sim$20 m water depth) over the three year period from November 2008 to November 2011 ('EB' in Figure 1.2). Daily averaged temperatures were computed from the observations for direct comparison with daily averaged model output. These data, described in more detail in Pitcher et al. (2014), provide a good indication of the inter-annual and event-scale upwelling/relaxation dynamics in the nearshore region of St Helena Bay.

Concurrent deployments of Wirewalker wave-powered profilers (Rainville and Pinkel, 2001; Pinkel et al., 2011) and bottom-mounted Acoustic Doppler Current Profilers (ADCP) provide high-frequency nearshore measurements of velocity, temperature, salinity, dissolved oxygen and Chl *a* fluorescence within St Helena Bay ('WW' in Figure 1.2). The full dataset is described in detail in Lucas et al. (2014), although only the velocity and temperature data over the February-April 2011 deployment are revisited in this study. The vertical resolution of the ADCP velocity data is 1 m while temperature is available at 0.25 m intervals. All data from the Wirewalker and ADCP moorings presented herein were filtered in time to provide a two hour running mean at 30 min intervals, sufficient for analysing processes at the diurnal-inertial frequency of interest for this study.

2.3 Model description

2.3.1 Equations of motion

The ocean model employed in this study is the V1.0 official release of the Coastal and Regional Ocean COmmunity model (CROCO[1]), an ocean modelling system built upon ROMS_AGRIF (Shchepetkin and McWilliams, 2005). CROCO is a free-surface, terrain-following coordinate oceanic model which solves the Navier-Stokes primitive equations by following the Boussinesq and hydrostatic approximations. The model solves equations governing the conservation of horizontal momentum (2.1 and 2.2), hydrostatic balance (Equation 2.3), incompressibility (Equation 2.4), conservation of heat and salt (Equations 2.5 and Equations 2.6), and a non-linear equation of state (Equation 2.7):

---

[1] `http://www.croco-ocean.org/`

$$\begin{aligned}
\frac{\partial u}{\partial t} + \vec{u}.\nabla u &= fv - \frac{1}{\rho_0}\frac{\partial P}{\partial x} + \nabla_h\left(K_{Mh}.\nabla_h u\right) + \frac{\partial}{\partial z}\left(K_{Mv}\frac{\partial u}{\partial z}\right), && (2.1)\\
\frac{\partial v}{\partial t} + \vec{u}.\nabla v &= -fu - \frac{1}{\rho_0}\frac{\partial P}{\partial y} + \nabla_h\left(K_{Mh}.\nabla_h v\right) + \frac{\partial}{\partial z}\left(K_{Mv}\frac{\partial v}{\partial z}\right), && (2.2)\\
0 &= -\frac{\partial P}{\partial z} - \rho g, && (2.3)\\
0 &= \frac{\partial u}{\partial x} + \frac{\partial v}{\partial y} + \frac{\partial w}{\partial z}, && (2.4)\\
\frac{\partial T}{\partial t} + \vec{u}.\nabla T &= \nabla_h\left(K_{Th}.\nabla_h T\right) + \frac{\partial}{\partial z}\left(K_{Tv}\frac{\partial T}{\partial z}\right) + \frac{1}{\rho_0 C_p}\left(\frac{\partial Q}{\partial z}\right), && (2.5)\\
\frac{\partial S}{\partial t} + \vec{u}.\nabla S &= \nabla_h\left(K_{Th}.\nabla_h S\right) + \frac{\partial}{\partial z}\left(K_{Tv}\frac{\partial S}{\partial z}\right), && (2.6)\\
\rho &= \rho(T, S, P), && (2.7)
\end{aligned}$$

where $\vec{u} = (u, v, w)$ is the velocity vector in a cartesian reference frame, P is the pressure, f is the Coriolis parameter, ρ is water density with ρ_0 is a constant reference density (1024 kg m^{-3}), T is the potential temperature, and S is salinity, Q is a solar flux, and C_p is the specific heat coefficient (3985 J kg^{-1} K^{-1}). K_{Mv} and K_{Tv} are the vertical turbulent viscosity and diffusivity, respectively, which are computed in this study using a k-ε turbulent closure parameterisation within the Generic Length-Scale (GLS) formulation (Umlauf and Burchard, 2003; Umlauf and Burchard, 2005). The GLS parameterisation of vertical mixing is considered appropriate for the simulation of wind-driven mixing in shallow surface mixed layers, as required for this study (Robertson and Hartlipp, 2017). Minimum values for K_{Mv} and K_{Tv} are taken as 10^{-4} m^2 s^{-1} and 10^{-5} m^2 s^{-1}, respectively, representing background values for molecular viscosity and diffusivity. Horizontal eddy viscosity (K_{Mh}) and diffusivity (K_{Th}) are commonly ignored in regional configurations using ROMS (e.g. Marchesiello et al., 2003; Veitch et al., 2010). Instead, horizontal dissipation at the grid scale is determined by dissipation associated with a third-order upstream biased horizontal advection scheme. A nonlinear equation of state adapted from Jackett and Mcdougall (1995) is used for the computation of density.

2.3.2 Vertical boundary conditions

The surface ($z = \eta$) boundary conditions are defined as:

$$
\begin{aligned}
\frac{\partial \eta}{\partial t} + \overrightarrow{u}.\nabla \eta &= w, && (2.8)\\
K_{Mv}\frac{\partial u}{\partial z} &= \frac{\tau_s^x}{\rho_0}, && (2.9)\\
K_{Mv}\frac{\partial v}{\partial z} &= \frac{\tau_s^y}{\rho_0}, && (2.10)\\
K_{Tv}\frac{\partial T}{\partial z} &= \frac{Q}{\rho_0 C_p}, && (2.11)\\
K_{Tv}\frac{\partial S}{\partial z} &= S(E-P), && (2.12)
\end{aligned}
$$

where η is the surface elevation, $\overrightarrow{\tau_s} = (\tau_s^x, \tau_s^y)$ is the surface wind stress vector, and $S(E-P)$ is the virtual salt flux due to the difference between evaporation (E) and precipitation (P). Bulk parameterisation is adopted for the computation of surface wind stress and surface net heat fluxes (Fairall et al., 1996; Fairall et al., 2003).

The bottom ($z = -H$) boundary conditions are defined as:

$$
\begin{aligned}
\overrightarrow{u}.\nabla H &= w, && (2.13)\\
K_{Mv}\frac{\partial u}{\partial z} &= \frac{\tau_b^x}{\rho_0}, && (2.14)\\
K_{Mv}\frac{\partial v}{\partial z} &= \frac{\tau_b^y}{\rho_0}, && (2.15)\\
K_{Tv}\frac{\partial T}{\partial z} &= 0, && (2.16)\\
K_{Tv}\frac{\partial S}{\partial z} &= 0, && (2.17)
\end{aligned}
$$

where $\overrightarrow{\tau_b} = (\tau_b^x, \tau_b^y)$ is the bottom shear stress vector, computed from a quadratic drag law:

$$
\begin{aligned}
\tau_b^x &= C_d\sqrt{u^2+v^2}u, && (2.18)\\
\tau_b^y &= C_d\sqrt{u^2+v^2}v, && (2.19)\\
C_d &= \left(\frac{\kappa}{\ln(z_b/z_0)}\right)^2, && (2.20)
\end{aligned}
$$

where κ is the von Kármán constant (0.4), z_0 is the bottom roughness length parameter (taken as 0.1 m) and z_b is the thickness of the bottom layer of the model. Upper and lower limits for C_d were applied as 0.02 and 0.0025, respectively.

2.3.3 Lateral boundary conditions

Open boundary conditions (OBCs) are implemented at the lateral boundaries of the model as described in Marchesiello et al. (2001). The model solution is 'nudged' to the specified boundary values (T, S, u, v, η) using relaxation times 1 day and 1 year for inward and outward radiation, respectively. Nudging is applied within the sponge layer of the model (10 grid cells wide) using a gradual decrease (cosine profile) from the open boundary to the inner border of the sponge layer.

2.3.4 Spatial and temporal discretisation

The vertical grid of the model is discretised using a terrain-following (σ) coordinate reference system. A curvilinear Arakawa C-grid is used for the discretisation of the horizontal plane. In order to improve computational efficiency, the model allows for the specification of separate time-steps for the computation of the barotropic and baroclinic modes.

2.4 Model Configuration

2.4.1 Grid

The model is comprised of a $\sim$3 km horizontal resolution parent domain as well as a $\sim$1 km horizontal resolution child domain, both centred around St Helena Bay and aligned according to the approximate orientation of the coastline (Figure 2.1). 2-way nesting is implemented between the parent and child domains, whereby at each time-step the parent domain provides boundary conditions for the child domain, which in turn provides feedback to the parent domain (Debreu et al., 2012). 50 levels are used to define the vertical grid of both domains. Baroclinic time-steps of 6 min and 2 min are adopted for the temporal integration of the parent and child domains,

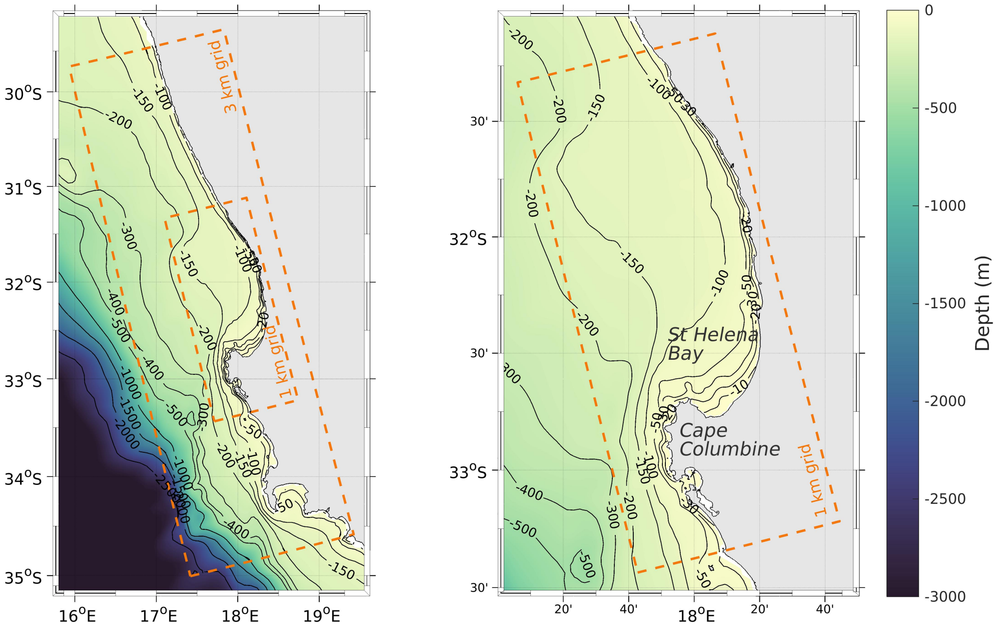

FIGURE 2.1: Model bathymetry and grid extents. A 1 km resolution child domain, centred over St Helena Bay, is nested within a 3 km resolution parent domain. The shown bathymetry within the model domains is derived from digital navigation charts for the region provided by the Hydrographer of the SA Navy, while data outside the model is from the 30-arc second GEBCO dataset.

respectively, reflecting the factor 3 difference in the spatial resolution of the domains. 60 barotropic time-steps are computed within each baroclinic time-step.

2.4.2 Bathymetry

The bathymetry assigned to the model grids has been interpolated from digital versions of the most detailed available navigation charts for the region, as provided by the Hydrographer of the South African Navy. The interpolated bathymetry has been smoothed to maintain a slope parameter ($r = \frac{\nabla H}{H}$) of less than 0.25 everywhere in the domain in an attempt to circumvent the well-known horizontal pressure gradient errors associated with σ-coordinate models with steep slopes (e.g. Haney, 1991). Minimum depths of 20 m and 5 m are enforced for the parent and child domains, respectively, to avoid vertical advection errors associated with thin vertical layers in shallow water. A semi-implicit vertical advection scheme is adopted to further assist in this regard. A hyperbolic tangent function was used over the sponge layer of the parent domain to gradually ramp up the model bathymetry to the 30-arc second

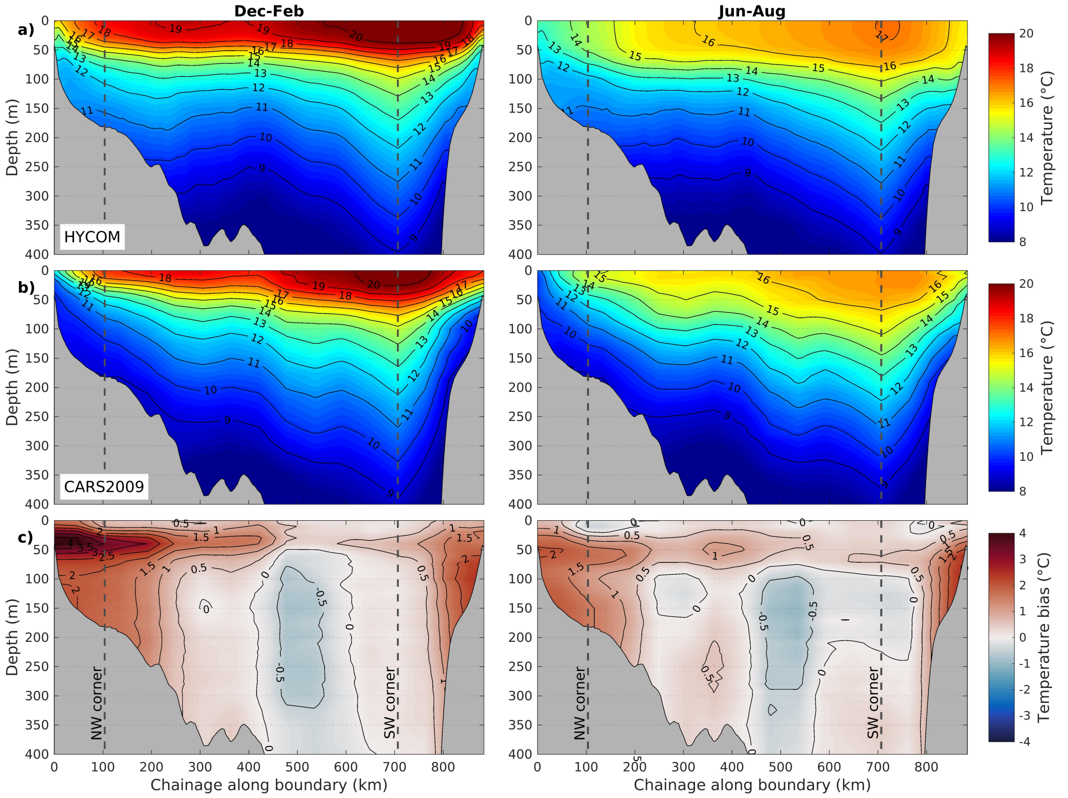

FIGURE 2.2: Seasonal temperature climatologies computed from the global HYCOM 1/12° reanalysis product (a), CARS2009 (b) and the computed bias in the HYCOM reanalysis product (c). Each panel presents data for the northen (chainage 0 - 104 km), western (chainage 104 - 707 km) and southern (chainage 707 - 884 km) boundaries of our CROCO parent domain (Figure 2.1).

GEBCO[2] dataset at the open boundaries of the model. This was done to match the internal bathymetry at the model boundaries with that of the global model providing lateral boundary forcing conditions (Section 2.4.3). The resulting model bathymetry is shown in Figure 2.1.

2.4.3 Initial condition and lateral boundary forcing

Boundary conditions for the parent domain are interpolated from daily η, T, S, u and v obtained from a 1/12° (∼9 km) global ocean reanalysis product provided by the HYCOM consortium[3] as part of the U.S. Global Ocean Data Assimilation Experiment (GODAE). Our model configuration effectively constitutes a dynamical downscaling of the global reanalysis product to ∼1 km resolution over St Helena Bay, so

---

[2] `https://www.gebco.net/`

[3] `https://www.hycom.org/data/glbu0pt08/expt-19pt1`

that the high-frequency bay-scale processes can be better assessed. The specified water levels exclude tidal variability, which has been shown to make an insignificant contribution to observed currents within St Helena Bay (Fawcett et al., 2008).

Due to the limited spatial extent of the model, the solution over our area of interest is largely influenced by the applied boundary conditions. The monthly temperature climatology computed from the HYCOM reanalysis product (based on daily output over years 2000 to 2012) was therefore compared against the monthly temperature climatology derived from observations, as provided by the CSIRO Atlas of Regional Seas (CARS2009[4]). Figure 2.2 presents the comparison along the full extent of the open boundaries of our CROCO parent domain for the seasons of austral summer (December - February) and winter (June - August). The comparison is favourable over much of the model boundaries, although the HYCOM reanalysis product exhibits a warm bias in the nearshore regions, particularly at the northern boundary during summer, where the bias exceeds 4°C in some places. Warm sea surface temperature biases within the nearshore regions of EBUS are a common shortcoming of large-scale ocean models (Richter, 2015; Small et al., 2015). To improve the nearshore water column structure of our simulation, the temporally and spatially interpolated monthly temperature bias, relative to CARS2009, was removed from the daily boundary conditions applied to the model. An analogous approach was adopted for the debiasing of the salinity boundary conditions. Model sensitivity experiments revealed that the debiasing of the model boundaries in this way removed a persistent warm bias in the nearshore subsurface waters within St Helena Bay, thereby improving the simulated vertical water column structure over our area of interest.

2.4.4 Atmospheric forcing

Atmospheric forcing (wind stress, heat and fresh water fluxes) for the model has been obtained from a Weather Research and Forecasting (WRF) model configuration developed by the Climate Systems Analysis Group (CSAG) at the University of Cape Town (UCT). The atmospheric simulation forms part of the Wind Atlas for

---

[4] `https://www.cmar.csiro.au/cars`

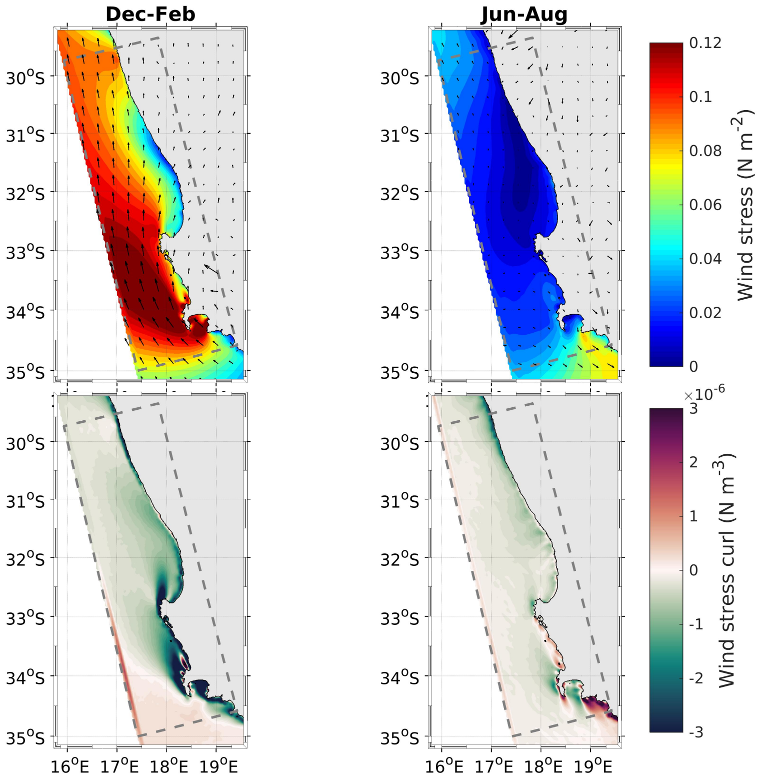

FIGURE 2.3: Seasonal climatology of wind stress and wind stress curl for the ~3 km resolution CSAG atmospheric product. The dashed grey line denotes the extent of our CROCO model configuration.

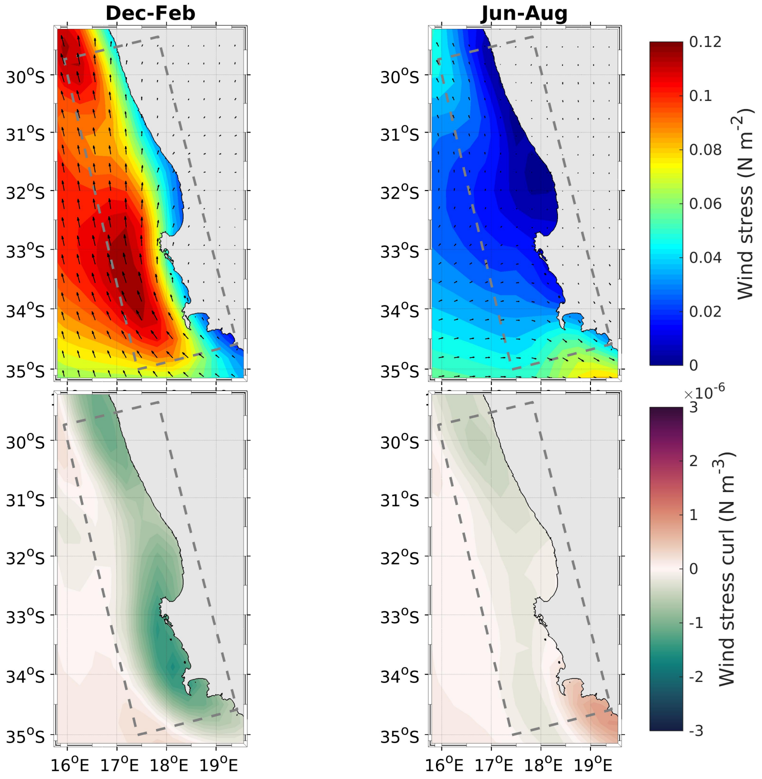

FIGURE 2.4: As per Figure 2.3 but for the CFSR atmospheric product.

South Africa (WASA[5]) project and has been validated against a number of land-based weather stations, including one deployed at the southern end of St Helena Bay over a three year period (Lennard et al., 2015). Model output is available on a 3 km horizontal resolution grid at hourly intervals for the period November 2005 to October 2013 (8 years). The offshore extent and orientation of our parent grid coincides with that of the WRF model grid.

Figure 2.3 presents seasonal climatologies of the wind stress and wind stress curl computed from the CSAG atmospheric product. Surface wind stresses for this analysis were derived from the hourly 10 m wind speeds using the empirical drag formulation of Large and Pond (1981). The analysis reflects the well-known seasonality in the mean winds over the southern Benguela, with the austral summer months dominated by alongshore upwelling-favourable winds (e.g. Shannon, 1985). The interaction of the large scale atmospheric circulation with the coast is shown to result in high spatial variability in the near-coastal winds, particularly during austral summer. The mechanisms driving the so-called wind drop-off at the coast are the local orographic features, coastline shape and sea surface temperature gradients (Burls and Reason, 2008; Renault et al., 2016). The resulting steep horizontal gradients in the wind stresses lead to locally enhanced cyclonic (negative) wind stress curl, particularly in the lee of the Cape Peninsula ($\sim$34° S) and Cape Columbine ($\sim$33° S). This result is consistent with limited airborne observations and high resolution atmospheric model simulations for these regions (Jury, 1985; Burls and Reason, 2008). The locally enhanced Ekman suction driven by the cyclonic wind stress curl is thought to contribute to the formation of upwelling cells in these regions, along with other factors such as the orientation of the coastline, the narrowing of the continental shelf, and enhanced alongshore wind stress (e.g. Lutjeharms and Meeuwis, 1987; Shannon and Nelson, 1996).

By way of comparison, Figure 2.4 presents the same analysis as shown in Figure 2.3, but for data over a 10 year period (2000 to 2010) obtained from the National Centers for Environmental Prediction (NCEP) Climate Forecast System Reanalysis (CFSR)

---

[5] `http://www.wasaproject.info/`

(Saha et al., 2010). The spatial resolution of the CFSR product is ∼0.3°, being typical of atmospheric forcing adopted for regional simulations of upwelling dynamics. Note that it is also the atmospheric product used to force the HYCOM global ocean reanalysis product used for the lateral boundaries of our model. The comparison highlights the inability of the CFSR atmospheric forcing product to capture the fine-scale near-coastal wind variability which can play an important role in upwelling and circulation over the area of interest (Desbiolles et al., 2016).

It is again noted that the wind stress applied as the vertical momentum boundary condition in the model is computed from hourly 10 m wind speed components using bulk parameterisation (Section 2.3.2). The hourly temporal resolution of the wind forcing is considered sufficient to resolve the land-sea breeze component of the winds, of particular interest in this study (the seasonal and spatial variability in the land-sea breeze component of the winds will be addressed in Section 3). In order to highlight the effect of the land-sea breeze on the ocean response, the model has been re-run with forced daily averaged wind stresses, determined from the output of the bulk parameterisation of the simulation using hourly averaged winds. In so doing, the simulation forced with daily averaged winds maintains net Ekman dynamics and surface heat fluxes, but the impact of the high-frequency component of the wind stress is removed.

2.5 Model assessment

The model has been integrated over the period 01 November 2005 to 31 December 2012 (7 years), spanning the duration over which all forcing data are available. Daily averaged output was generated over the entire simulation period for the assessment of sub-inertial Ekman dynamics, while hourly averaged output was generated for the month of March 2011 for comparison with the high-frequency observations of Lucas et al. (2014). Three hourly 'snapshots' of temperature were additionally generated over the entire simulation period, allowing for the assessment of super-diurnal tracer dynamics (these output are analysed further in Chapter 5).

Figure 2.5 shows the hourly averaged surface temperature and horizontal current

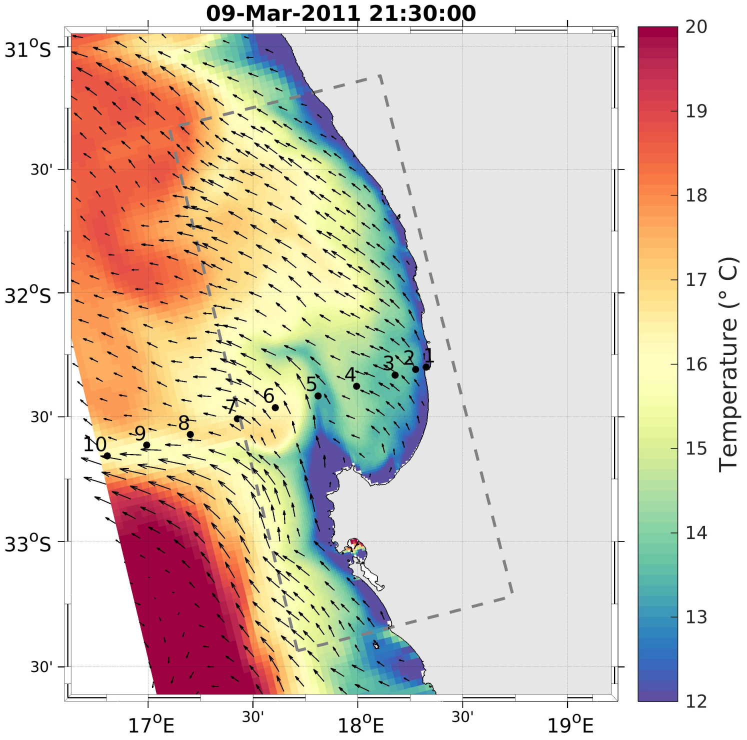

FIGURE 2.5: Hourly averaged surface temperature and horizontal current vectors during an upwelling event. The numbered points denote the St Helena Bay Monitoring Line sample stations.

vectors from the model during an upwelling event included in the observations of Lucas et al. (2014) (this event is given particular attention in Chapters 3 and 4). The event displays some typical features of the upwelling system, as documented in the literature and summarised in Chapter 1.3. For instance, intensified upwelling associated with the Cape Columbine upwelling cell is evident, as is the bifurcation of the equatorward Goodhope Jet into offshore and alongshore components north of Cape Columbine, with the alongshore component corresponding to the Columbine Jet. The surface waters within St Helena Bay are shown to be flanked by the Columbine Jet at the offshore boundary and a narrow strip of upwelling along the inner shelf.

Figure 2.6 presents a comparison of modelled and observed seasonal temperature climatologies along the St Helena Bay Monitoring Line (SHBML). A comprehensive analysis of the spatial and seasonal variability along the SHBML is provided in Lamont et al. (2015), while we provide a brief summary here. The offshore vertical water column characteristics are shown to be distinct from those in the nearshore. Offshore surface water temperatures (Stations 7 to 10) display strong seasonality, with

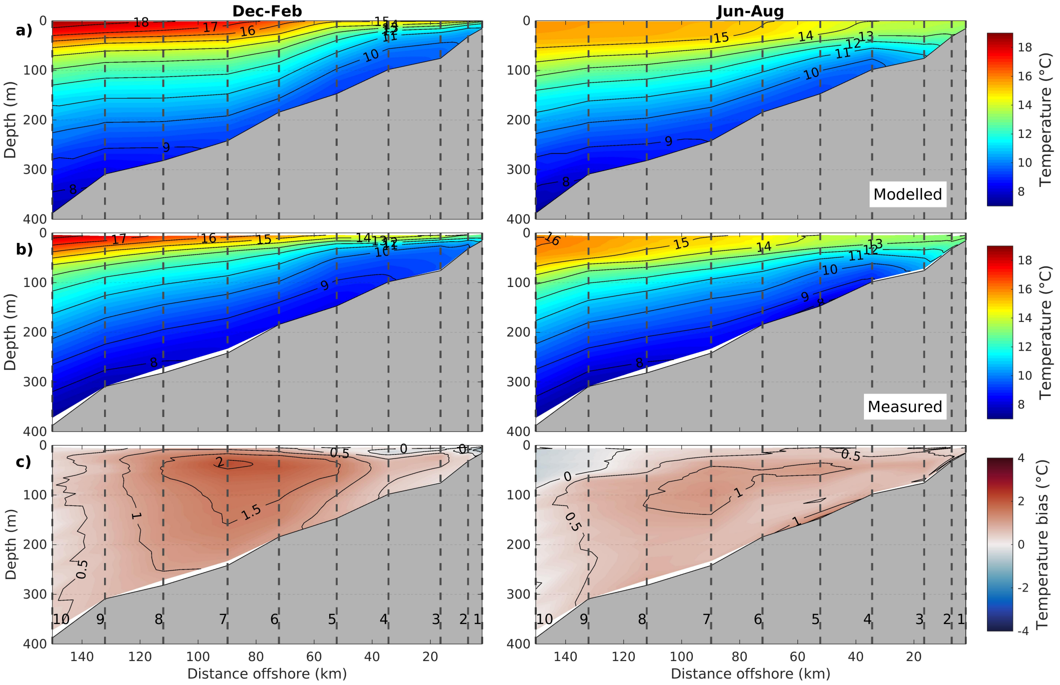

FIGURE 2.6: Seasonal temperature climatologies for the St Helena Bay Monitoring Line (SHBML) as computed from the model (a), from the observations (b) and the resulting model bias (c). The numbered vertical dashed lines denote the station locations shown in Figure 2.5.

warmer waters in summer following the seasonal variation in solar insolation. Subsurface water temperature at these stations however exhibit much less seasonality. Nearshore temperatures are cooler than those offshore, particularly during summer months, in line with the seasonal variability in upwelling-favourable winds (Figure 2.3). Within St Helena Bay (Stations 3 and 4) the mean vertical water column structure during summer is shown to be charaterised by a highly stratified shallow surface mixed layer overlaying cool subsurface waters. In contrast, winter months at these stations are characterised by a nearly fully mixed water column. Mean temperature profiles in the near-coastal zone (Stations 1 and 2) are cooler in summer than in winter, corresponding to enhanced inner shelf upwelling at these stations during summer. The model is shown to compare well against the observations, although an overall warm bias is evident (it should be noted that the nearshore warm bias was reduced due to the debiasing of the model boundaries as described in Section 2.4.3). The model bias within St Helena Bay (Stations 1 to 4) is shown to be below 1°C for both summer and winter seasons, indicating that the described seasonal variability of the vertical water column structure over the area of interest is well represented in the model.

Figure 2.7 presents a 3 year time-series of measured and modelled daily averaged temperature at the Elands Bay fixed mooring ('EB' in Figure 1.2). Table 2.1 provides summary statistics for the nominally winter (April - September) and summer (October - March) periods. In addition to the mean and standard deviation (σ) of both the measured and modelled time-series, the model performance is quantified through the centered root mean square difference ($RMSDC$) and Pearson's correlation coefficient. For a series of N measured values x and the corresponding model values y, the performance metrics are computed as follows:

$$RMSDC = \sqrt{\frac{\sum\limits_{i=1}^{N}\left((y_i - \overline{y}) - (x_i - \overline{x})\right)^2}{N}}, \tag{2.21}$$

$$Correlation = \frac{\sum\limits_{i=1}^{N}\left((y_i - \overline{y})(x_i - \overline{x})\right)}{N\sigma_x\sigma_y}, \tag{2.22}$$

where $\overline{x}$ and $\overline{y}$ are the mean values over the measurements and model output, respectively. The presented statistics are limited to periods where both measurements and model output are available.

The data reflects the seasonal variability in the near-coastal water column as elucidated in the model comparison with the SHBML, but provides some further insight into the inter-annual and event-scale variability. The nearshore water column is shown to be well mixed over the nominally winter months of June-August, with

TABLE 2.1: Seasonal summary statistics for the time-series shown in Figure 2.7.

	Dec-Feb			Jun-Aug		
	5 m	20 m	Strat.	5 m	20 m	Strat.
Observed mean	13.67	11.09	2.5	12.9	12.65	0.38
Observed σ	2.34	1.84	1.2	0.98	1.06	0.42
Modelled mean	12.43	10.98	1.45	13.34	13.2	0.22
Modelled σ	2.13	1.95	1.1	0.91	0.99	0.31
RMSDC	1.42	0.93	1.04	0.39	0.49	0.37
Correlation	0.8	0.88	0.6	0.92	0.89	0.54

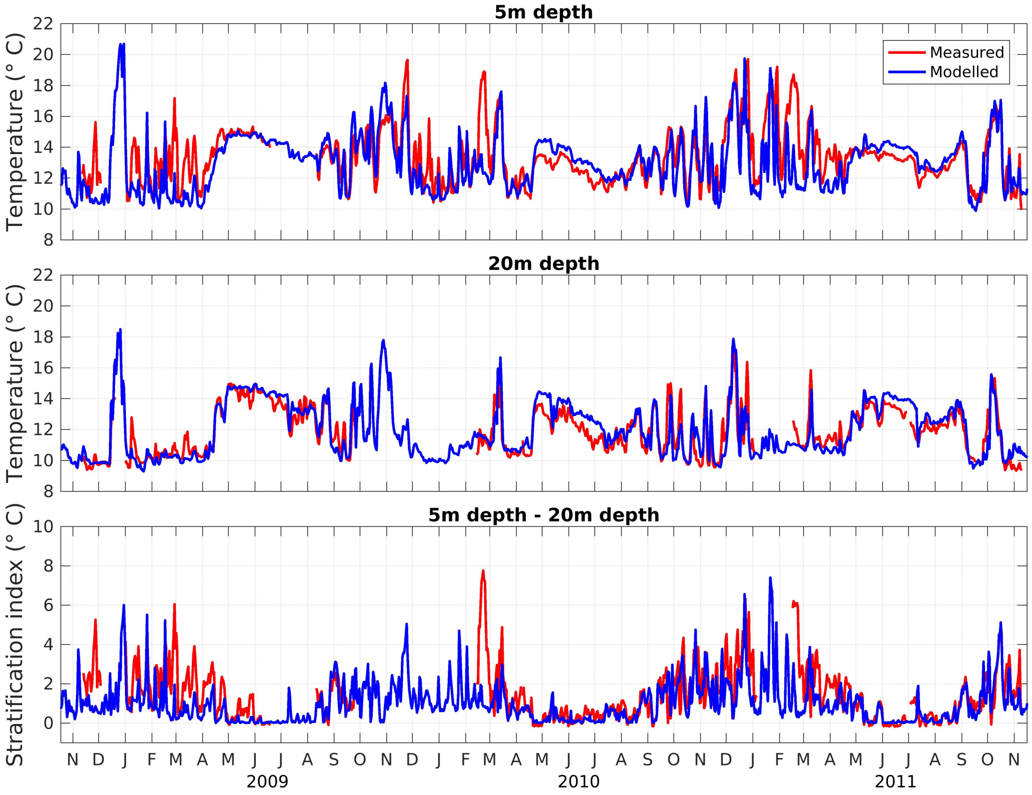

FIGURE 2.7: Time-series comparison of daily averaged measured and modelled temperature at 5 m and 20 m depths at the Elands Bay fixed mooring ('EB' in Figure 1.2), located in 20 m water depth). The stratification index is simply the difference between the temperature at 5 m and 20 m depths.

relatively little variability (observed stratification of 0.38 ± 0.42°C). In contrast, the nominally summer months of December-February are characterised by an increase in stratification events and also larger variability in nearshore temperatures (observed stratification of 2.5 ± 1.2°C). The enhancement of both stratification and variability during summer reflects the dynamics of upwelling/relaxation events, where periods of active upwelling give rise to a cold homogenous water column, while relaxation and associated retention can warm surface waters and stratify the water column. Warm waters formed during relaxation events can extend to the bottom, as reflected in the time-series at 20 m depth. As such, both the warmest and coldest temperatures occur during summer months, both at the surface and at the bottom. The model is shown to under-predict surface warming for some relaxation events (top panel of Figure 2.7), resulting in a cool bias (∼1.2°C) in the surface waters during summer which is reflected in a commensurate under-prediction in mean stratification. This suggests that upwelling may be somewhat over-estimated in the model

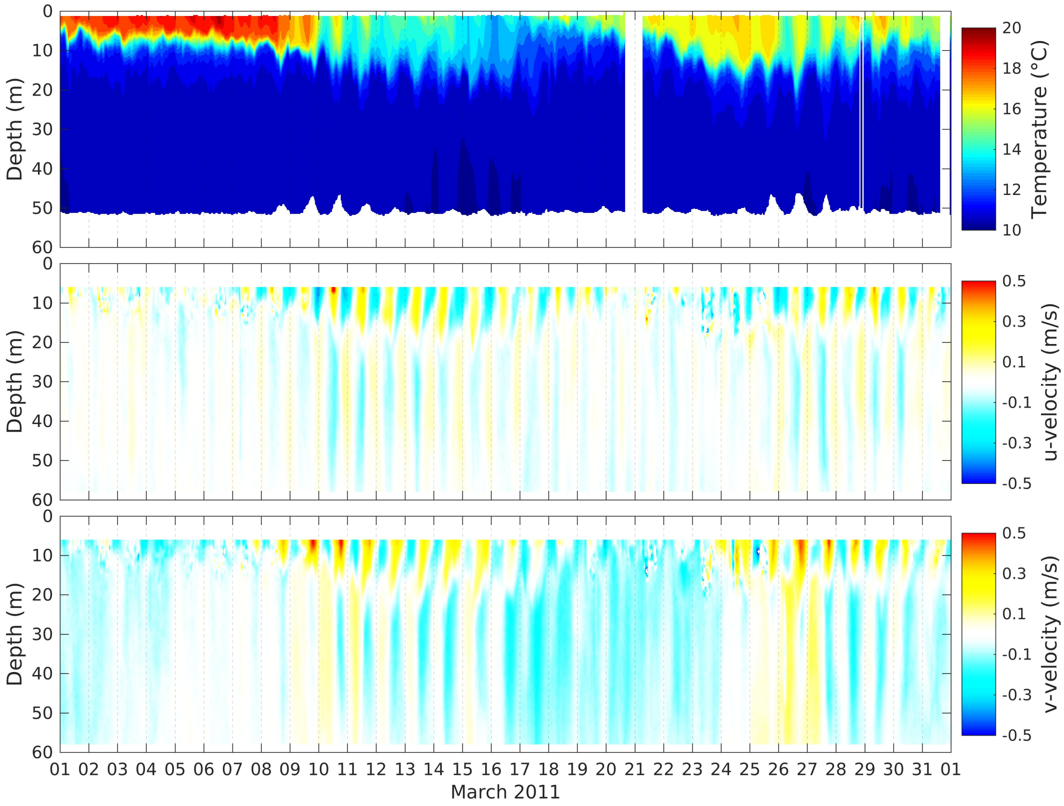

FIGURE 2.8: Observed temporal evolution of temperature and horizontal velocity components for March 2011 from the Wirewalker fixed mooring in 60 m water depth ('WW' Station 1 in Figure 1.2).

and/or local heating and bay retention may be under-estimated. Surface model temperatures achieve correlation coefficients of 0.8 and 0.92 for the summer and winter periods, respectively. Subsurface bias is low throughout the year (<0.6°C) and correlation coefficients are 0.88 and 0.89 for the summer and winter periods, respectively. Overall, these results indicate that the model shows acceptable skill at capturing the salient features of upwelling/relaxation dynamics in St Helena Bay.

Figure 2.8 presents the observed temporal evolution of temperature and horizontal velocity profiles for a 1 month period at the Wirewalker Station 1 fixed mooring in 60 m water depth ('WW' Station 1 in Figure 1.2), while the hourly averaged model output is shown in Figure 2.9. The comparison provides some insight into the extent to which the observed super-inertial variability, embedded within the sub-inertial upwelling dynamics, is captured by the model. The considered period begins with a relaxation event characterised by a highly stratified two layer system and a weak poleward sub-inertial current. The onset of an upwelling event on 07 March 2011 is shown to be accompanied by strong variability at the diurnal-inertial frequency

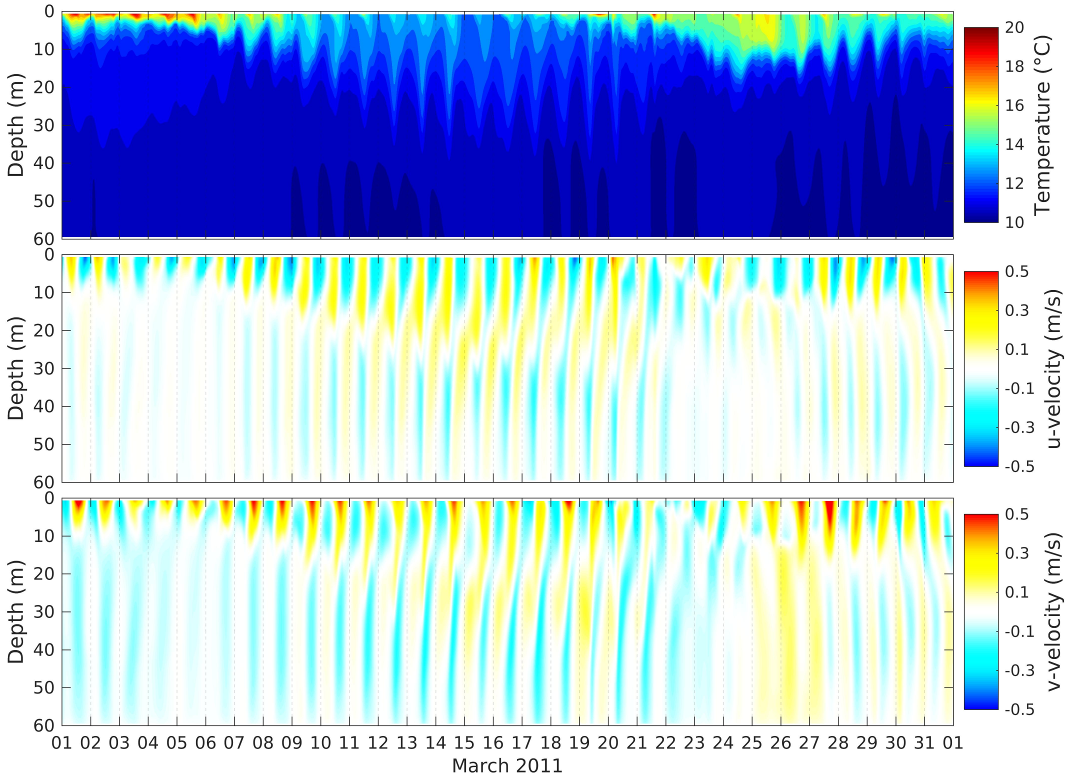

FIGURE 2.9: As per Figure 2.8 but for the hourly averaged model output.

in both the temperature and horizontal velocity profiles, with a 180° phase shift between the surface and subsurface currents. The restratification of the water column (17-25 March 2011) is again accompanied by a poleward sub-inertial current, followed by the onset of strong variability at the diurnal-inertial frequency, as described for the previous event. The model is shown to include both the salient features of the sub-inertial upwelling/relaxation dynamics of the observations, as well as the significant diurnal-inertial variability of the temperature and horizontal velocity profiles.

The model performance over the shown 1 month period is summarised in Figure 2.10 through depth varying summary statistics of temperature and horizontal velocity components (refer to Equations 2.21 and 2.22). Surface temperatures are shown to be under-estimated over the considered period while the subsurface ($>\sim$20 m depth) bias is low ($<$0.5°C), in general agreement with the previously shown results. Although temperature correlation in the subsurface is low (even negative), this is attributed to the lack of a meaningful temperature signal over the considered period, as evidenced by the low RMSDC in this region of the water column

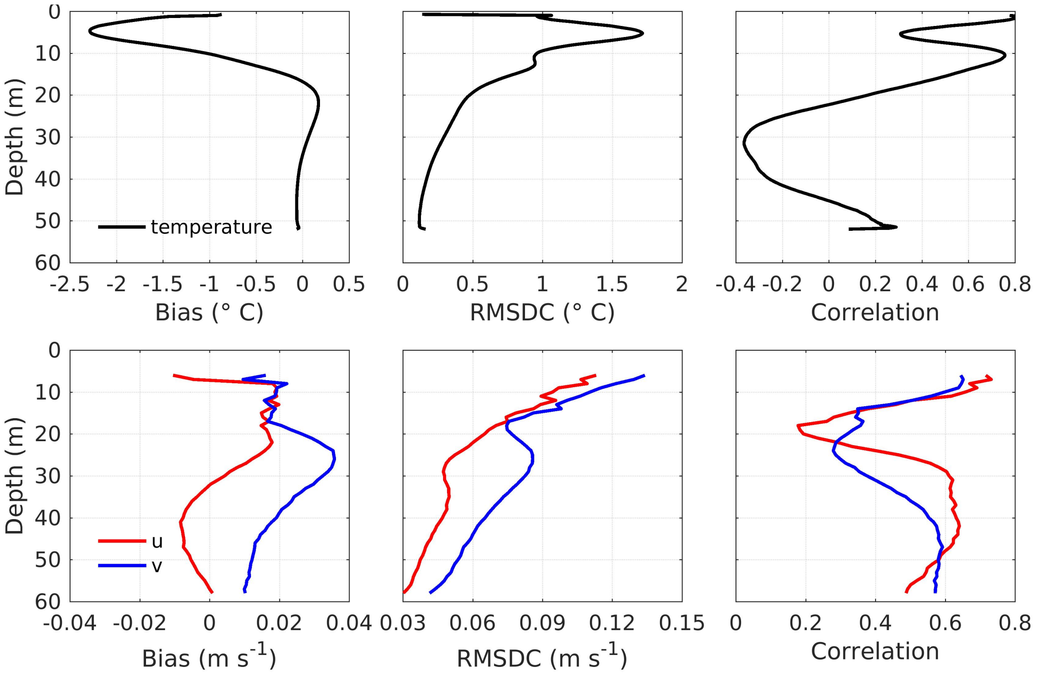

FIGURE 2.10: Summary statistics as a function of depth for the temperature and horizontal current velocity model output shown in Figure 2.9 compared with the observations shown in Figure 2.8.

(<0.5°C for depths greater than ∼20 m). Temperature correlations are higher near the surface, attaining a maximum correlation coefficient of ∼0.8 in the surface layer of the model. Temperature correlations are however clearly hampered by the misrepresentation of the depth of the thermocline, which is generally under-estimated in the model, particularly over the initial stratification event. The model tends to over-estimate the persistence of diurnal-inertial variability in the horizontal current velocities. Maximum correlation coefficients of between ∼0.5 and ∼0.7 are attained for both near-surface and near-bottom horizontal current velocities. These correlation coefficients show a minimum near ∼20 m depth, which is not surprising given that this region is located at the base of the thermocline where the 180° phase shift between the surface and subsurface currents is observed. Misrepresentation in the depth of the thermocline therefore particularly impacts the horizontal current correlations in this region of the water column.

The observed energetic diurnal-inertial response of the ocean has been attributed to resonance between the land-sea breeze and the inertial response of the ocean, as described in Section 1.3.3. Figure 2.11 provides insight into the impact of the high frequency component of the winds, by presenting the model solution when forced

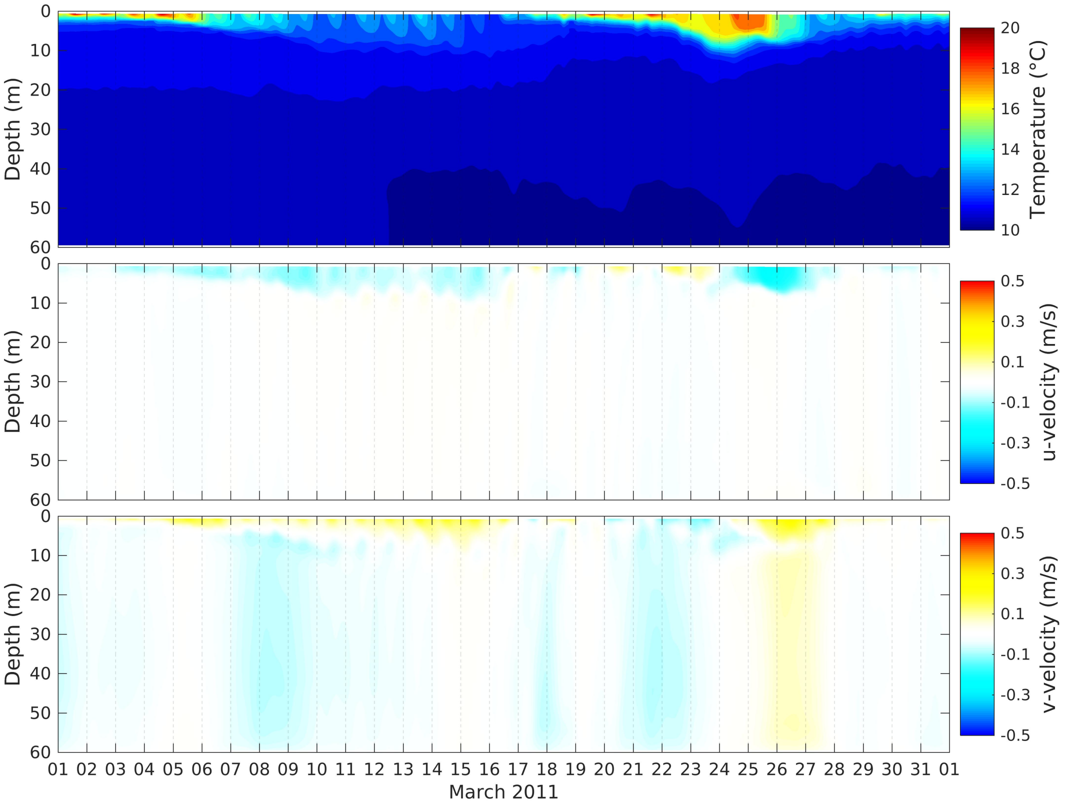

FIGURE 2.11: As per Figure 2.9 but for the model forced with daily averaged wind stress.

with daily averaged wind stresses. The results indicate that the sub-inertial upwelling/relaxation dynamics are retained, however the diurnal-inertial response of the ocean is completely removed. A further observation is that the surface mixed layer of the simulation forced with daily averaged winds is notably warmer and shallower, indicating that the high-frequency component of the winds plays an important role in the modulation of the surface mixed layer through shear-induced diapycnal mixing of surface and subsurface waters.

2.6 Discussion and conclusions

In this chapter we have presented a downscaling methodology for the simulation of the bay-scale processes of St Helena Bay. Hourly atmospheric forcing from a high resolution ($\sim$3 km) WRF model configuration ensures that the land-sea breeze is resolved and that important local orographic effects on the winds are included in the model forcing. The methodology of downscaling a global model to higher resolution will always be hampered by any errors/biases in the adopted global model. The removal of monthly temperature and salinity biases in the 1/12° HYCOM reanalysis product adopted in this study has provided an effective means of circumventing some of the shortcomings in the global model. It is however noted that only one global ocean reanalysis product was considered in this study, and that other large scale ocean models may in fact provide more suitable lateral boundary conditions for our shelf model. While outside the scope of this study, future studies in this region would benefit from a thorough assessment of global ocean reanalysis products to determine the most appropriate product(s) to be used for forcing shelf and coastal models in the southern Benguela upwelling system (e.g. de Souza et al., 2020, in the context of New Zealand waters).

Comparison of the seasonally averaged model output against observations from the SHBML indicate that the model displays reasonable skill in reproducing the seasonal means in the vertical water column structure within St Helena Bay. This is considered particularly important within the context of this study, as the model is used to assess the extent to which the vertical water column structure within St Helena Bay is modulated by the land-sea breeze (Chapter 5). It is also encouraging to note that a 3 year time-series comparison of temperature from the Elands Bay fixed mooring, in 20 m water depth, indicates that the model shows reasonable skill in reproducing event-scale upwelling/relaxation dynamics. While not the focus of this thesis, the results suggest that the methodology described in this chapter may provide a good basis for the development of an operational ocean forecast system for the bay. Such an advancement has been actively encouraged for the effective management of the coastal environment in this region (Bernard et al., 2006).

Comparison of model output from simulations forced with hourly and daily averaged wind stress has highlighted the significant extent to which the land-sea breeze can impact the vertical water column structure and currents within St Helena Bay. This result provides further evidence that inertial oscillations triggered by diurnal wind variability near the critical latitude are responsible for shear-induced diapycnal mixing and the deepening of the thermocline. Associated with the diapycnal mixing is enhanced subsurface nutrient flux to the surface layer, which Lucas et al. (2014) argued is likely to have a significant impact on the phenomenology of phytoplankton blooms within St Helena Bay. In light of this, the results provide further motivation for a detailed investigation into the physical processes driven by the land-sea breeze in upwelling systems near the critical latitude. The model presented in this chapter provides a useful basis from which to carry out numerical experiments to this end, as presented in Chapter 5. We first however turn to reduced physics experiments which allow us to provide a clearer understanding of the fundamental processes governing the forced response (Chapter 3) and internal wave response (Chapter 4) to land-sea breeze forcing of EBUS.

Chapter 3

The forced response to the land-sea breeze near the critical latitude

Publication based on the content of this chapter:

Fearon, G., Herbette, S., Veitch, J., Cambon, G., Lucas, A. J., Lemarié, F., & Vichi, M. (2020). Enhanced vertical mixing in coastal upwelling systems driven by diurnal-inertial resonance: Numerical experiments. Journal of Geophysical Research: Oceans, 125, e2020JC016208.

3.1 Introduction

In this chapter we carry out 1D-vertical numerical experiments with the aim of elucidating diapycnal mixing dynamics of a coastal system characterised by two layers separated by strong stratification and forced by a land-sea breeze near the critical latitude of 30°N/S. The use of a 1D-vertical model precludes the internal wave response, allowing us to isolate the impact of the locally forced response. The no-flow condition perpendicular to the land boundary is included in the model through the 'Craig approximation' (Section 1.2.3), although the formulation presented in Simpson et al. (2002) is extended here to include the effect of bottom friction terms. The bulk shear production theory of Burchard and Rippeth (2009) is compared with both the model and observations, providing a useful lens through which to interpret the event-scale mixing dynamics. Diapycnal mixing is further diagnosed through the initialisation of the model with a passive tracer below the surface layer, used to represent a reservoir of subsurface nutrients. The model is used to undertake a series of experiments to explore the physical processes and key drivers of enhanced vertical mixing in coastal upwelling systems due to diurnal-inertial resonance. Comparison of the model with the observations of Lucas et al. (2014) provides insight into the strengths and limitations of the model. Implications of the model results for surface layer nutrient enhancement in St Helena Bay and other EBUS is then inferred.

3.2 Methods

3.2.1 Atmospheric forcing

Atmospheric forcing data for the 1D-vertical experiments have been obtained from the CSAG WRF model described in Section 2.4. Surface wind stresses shown in this chapter are derived from the CSAG 10 m wind speeds using the empirical drag formulation of Large and Pond (1981). Rotary analyses have been carried out on the wind stress data to extract the diurnal anticyclonic (anticlockwise in the southern hemisphere) rotary component of the wind stress (τ^{ac}). Near latitudes of 30° N/S, τ^{ac} represents the component of the wind stress which rotates in the same direction and frequency as the inertial oscillation, and so energy flux from the wind is at all times positive (in the absence of background currents).

The complex function $\tau^{ac} = \tau^{ac0} e^{i(\omega t + \phi^{ac})}$ defines a wind stress vector rotating in an anticlockwise direction with a diurnal frequency ω, a constant amplitude τ^{ac0}, and a phase angle ϕ^{ac}. The purpose of the rotary analysis is to compute the parameters τ^{ac0} and ϕ^{ac} from the time-series of wind stress components. To do this, the wind ellipse parameters were firstly determined via a diurnal least squares fit (lsf) harmonic analysis on each of the wind stress components, from which the parameters τ^{ac0} and ϕ^{ac} were extracted using standard conversion techniques provided in the tidal_ellipse Matlab package (Xu, 2002). As the periodicity of the wind stress varies over time (unlike a tidal constituent whose phase and amplitude are constant), the result of the rotary analysis is particularly sensitive to the time window over which

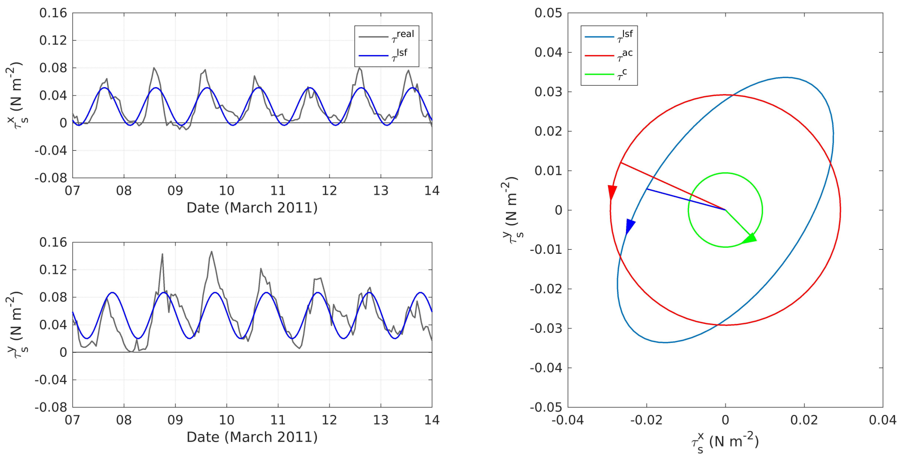

FIGURE 3.1: Rotary analysis of wind stress over an example 7 day period used to carry out realistically forced 1D simulations. The blue time-series are the diurnal least squares fit curves to the wind stress components which sweep the blue ellipse (τ^{lsf}). The ellipse is decomposed into clockwise (τ^{c}) and anticlockwise (τ^{ac}) rotating components. The radial lines indicate the associated phase angles.

the analysis is carried out. Longer windows lead to smaller amplitude rotary components and a poorer fit to inter-diurnal variability. All rotary analyses presented in this chapter have been carried out on 7 day windows, representative of the timescale of individual upwelling events. The methodology described above is depicted in Figure 3.1 for the period used to compare observed event-scale mixing dynamics with the model. The WRF model output was extracted at the location of the observations ('WW' Station 1 in Figure 1.2), providing the wind stress and heat flux input for the ocean model.

3.2.2 Ocean model

The ocean model employed in this chapter is a standalone 1D-vertical version of the model described in Section 2.3, in which we retain the horizontal pressure gradient term normal to the coast. The primitive equations governing the conservation of horizontal momentum and tracers reduce to the following:

$$\frac{\partial u}{\partial t} = fv + \frac{\partial}{\partial z}\left(K_{Mv}\frac{\partial u}{\partial z}\right) - g\frac{\partial \eta}{\partial x}, \tag{3.1}$$

$$\frac{\partial v}{\partial t} = -fu + \frac{\partial}{\partial z}\left(K_{Mv}\frac{\partial v}{\partial z}\right), \tag{3.2}$$

$$\frac{\partial T}{\partial t} = \frac{\partial}{\partial z}\left(K_{Tv}\frac{\partial T}{\partial z}\right) + \frac{1}{\rho_0 C_p}\left(\frac{\partial Q}{\partial z}\right), \tag{3.3}$$

$$\frac{\partial S}{\partial t} = \frac{\partial}{\partial z}\left(K_{Tv}\frac{\partial S}{\partial z}\right), \tag{3.4}$$

$$\frac{\partial C}{\partial t} = \frac{\partial}{\partial z}\left(K_{Tv}\frac{\partial C}{\partial z}\right), \tag{3.5}$$

In addition to the variables described in Section 2.3, we include a passive tracer C (Equation 3.5) used to represent the concentration of subsurface nutrients. Surface and bottom boundary conditions for the model are as described in Section 2.3, but we assume zero water flux at the surface since temperature is the major driver for density in the region.

3.2.3 'Craig approximation'

The effect of the land boundary (assumed to be orientated along the y-axis for the purposes of these experiments) is implicitly included in the model through the surface elevation gradient term ($\frac{\partial \eta}{\partial x}$) in Equation 3.1, being a user-specified input to the model. This term has been determined according to Craig (1989) and Simpson et al. (2002), however here we extend the formulation to include the effect of bottom friction. The governing equations for depth-averaged velocity components (U, V) can be written as:

$$\frac{\partial U}{\partial t} = fV - g\frac{\partial \eta}{\partial x} + \frac{\tau_s^x}{\rho H} - \frac{\tau_b^x}{H}, \tag{3.6}$$

$$\frac{\partial V}{\partial t} = -fU - g\frac{\partial \eta}{\partial y} + \frac{\tau_s^y}{\rho H} - \frac{\tau_b^y}{H}, \tag{3.7}$$

where H is the water depth. If U and V are taken to represent the cross-shore and alongshore depth-averaged velocity components, respectively, then the condition of zero depth-average flow perpendicular to the coast dictates that $U = 0$ and therefore $\frac{\partial U}{\partial t} = 0$. Assuming zero alongshore pressure gradients ($\frac{\partial \eta}{\partial y} = 0$) and a wave solution for the alongshore depth-averaged velocity ($\frac{\partial V}{\partial t} = -i\omega V$), then Equation 3.7 can be recast as $V = \frac{i}{\omega H}(\frac{\tau_s^y}{\rho} - \tau_b^y)$. Substitution of V into Equation 3.6 yields the surface elevation gradient response:

$$\frac{\partial \eta}{\partial x} = \frac{\tau_s^x + i(f/\omega)\tau_s^y}{\rho g H} - \frac{\tau_b^x + i(f/\omega)\tau_b^y}{g H}. \tag{3.8}$$

The wind stress terms $\left(\frac{\tau_s^x + i(f/\omega)\tau_s^y}{\rho g H}\right)$ correspond to the 'Craig approximation' as presented in Simpson et al. (2002). As we aim to force the model with realistic wind stresses, and do not have an a priori analytical solution for bottom shear stresses, the complex terms in Equation 3.8 preclude an analytical solution for $\frac{\partial \eta}{\partial x}$. The assumption of diurnal variability as the dominant signal in both surface and bottom stress is however made, being valid in the case of land-sea breeze forcing near the critical latitude, as the periodicity in both the forcing and the ocean response can be assumed to be near-diurnal. In the case of periodically oscillating wind and bottom stress, the complex terms in Equation 3.8 correspond to a $\frac{\pi}{2}$ phase shift in these variables. We therefore assign the terms $i\tau_s^y$ and $i\tau_b^y$ to be equal to the values of τ_s^y and τ_b^y at a time 6 hours prior to the given time-step, respectively.

3.2.4 Model configuration

The number of vertical layers was assigned to be equal to the water depth in metres, ensuring the same vertical grid resolution for all simulations. A time-step of 10 s was used to integrate the model solution over a period of 7 days from initialisation, typical of the time-scale of upwelling events. Model output at 30 min intervals was filtered in time to provide a two hour running mean at each time-step, consistent with the processing of observations. Both analytical and realistic model configurations were employed. Simulations were initialised from rest using a constant salinity of 35 and a temperature profile defined either analytically or from observations, as described below.

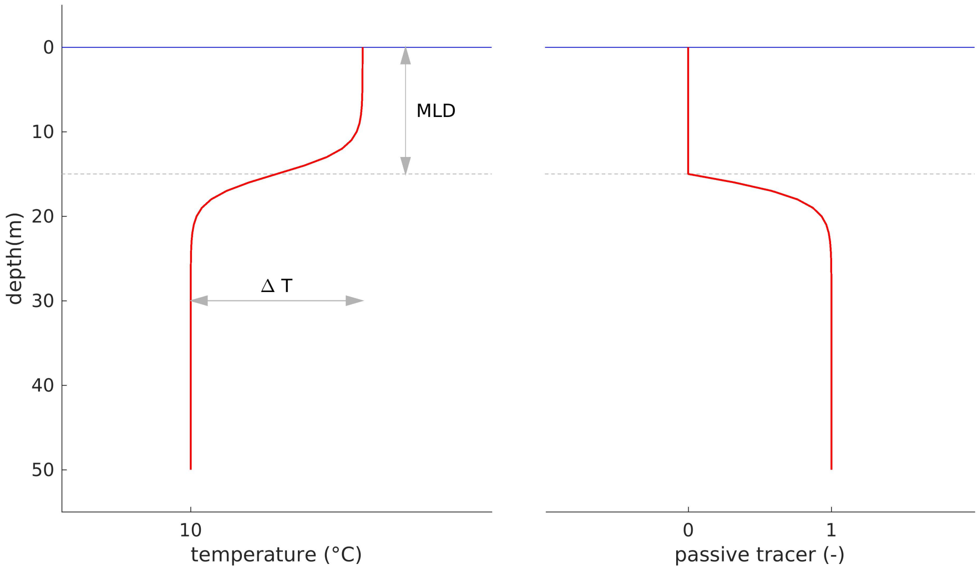

FIGURE 3.2: Schematic of analytical initial conditions for temperature and a passive tracer. The temperature profile is a hyperbolic tangent function centred around the initial MLD, while the passive tracer profile adopts the same profile shape as temperature below the initial MLD

The purpose of the analytical model configurations was to explore the physical processes and key drivers of enhanced vertical mixing in a two layer coastal system due to diurnal-inertial resonance. The initial temperature profile for these experiments was specified according to a hyperbolic tangent function as follows:

$$T(z) = 10 + \Delta T/2(1 - \tanh(((z - \text{MLD})/3)), \tag{3.9}$$

where ΔT is the difference between surface and subsurface temperatures and MLD the initial mixed layer depth, corresponding to the depth of maximum stratification. As shown in Figure 3.2, the resulting profile increases from 10° C in the subsurface to a specified surface layer temperature. Higher ΔT's imply higher levels of stratification. Surface wind stress forcing took the form of constant amplitude rotating winds at a diurnal frequency (representative of the land-sea breeze), constant winds (representative of a mean alongshore wind), or a combination of the two. Surface heat fluxes were ignored in the analytical configurations.

A realistic model configuration was use to compare the model with the observations of Lucas et al. (2014) over the period 7-14 March 2011, having been identified as a period which clearly demonstrates the response of a highly stratified two layer system to the onset of upwelling favourable winds with an anticlockwise sense of rotation (Figure 1.3). The initial temperature profile for this simulation was interpolated directly from the observations. Surface wind stress forcing took the form of both realistic wind stresses derived from the WRF model output as well as the diurnal anticlockwise rotary component of the wind stress (τ^{ac}), as shown in Figure 3.1. Surface heat flux forcing was estimated as the net heat flux derived from short and long wave radiation output from the WRF model, ignoring contributions of latent and sensible heat. This yielded daily peaks in positive heat flux of approximately 800 $\mathrm{W/m^2}$ over the simulation period.

3.2.5 Diapycnal mixing diagnostics

As this chapter focusses on diapycnal mixing at the interface of a two layer system, we use the bulk shear vector $\overrightarrow{S} = (S_u, S_v)$ as defined by Burchard and Rippeth (2009) as an indicator of shear between the surface and bottom layers:

$$S_u = \frac{u_s - u_b}{1/2H}, \qquad S_v = \frac{v_s - v_b}{1/2H}, \tag{3.10}$$

where $\overrightarrow{u_s} = (u_s, v_s)$ and $\overrightarrow{u_b} = (u_b, v_b)$ are the depth-averaged velocity vectors for the surface and bottom layers, respectively. Based on the one-dimensional momentum equations for a two layer system, Burchard and Rippeth (2009) derived the dynamical equation for bulk shear squared ($S^2 = S_u^2 + S_v^2$), used in this chapter as a tool for interpreting event-scale mixing dynamics:

$$\frac{\partial S^2}{\partial t} = \frac{4}{H}\overrightarrow{S} \cdot \left(\frac{\overrightarrow{\tau_s}}{H_s} + \frac{\overrightarrow{\tau_b}}{H_b}\right) - c_i \frac{H^2}{H_s H_b} S^3, \tag{3.11}$$

where H_s and H_b are the depths of the surface and subsurface layers, respectively, $\overrightarrow{\tau_s} = (\tau_s^x, \tau_s^y)$ is the surface shear stress vector, $\overrightarrow{\tau_b} = (\tau_b^x, \tau_b^y)$ is the bottom shear stress vector and c_i is the interfacial drag coefficient. Here, H_s is computed from a defined isotherm (varying depending on the configuration), used as a proxy for the interface between the upper and lower layers. c_i may be roughly estimated as follows:

$$c_i = K_{Mv} \frac{4S_i}{H^2 S^2}, \tag{3.12}$$

where S_i is the interfacial shear estimated locally at the interface of the two layers (Burchard and Rippeth, 2009). Estimates of c_i from the model output were computed using the K_{Mv} returned from the k-ε turbulent closure scheme, while a constant value of $K_{Mv} = 1.5 \times 10^{-4}$ m^2 s^{-1} was adopted for processing of the observations. Equation 3.11 dictates that bulk shear is generated when the bulk shear vector is in alignment with the surface and/or bottom shear stress vectors. The last term on the right hand side of Equation 3.11 represents the loss of bulk shear due to interfacial mixing between the two layers. In this chapter we compare the theoretical bulk shear production of Equation 3.11 with that computed directly from the model output and from the observations. $\frac{\partial S^2}{\partial t}$ from both the model output and observations is computed as the gradient of a least squares fit straight line for data within a 2 hour window of each 30 min time-step.

The quantification of diapycnal mixing over the simulations was further aided by initialising the model with a passive tracer (C) below the surface mixed layer, representing a reservoir of subsurface nutrients. The cumulative diapycnal mixing of the passive tracer to the surface layer has been computed by vertically integrating the passive tracer over the surface layer:

$$C_s = \int_{-H_s}^{0} C \, dz. \tag{3.13}$$

C_s provides an indicator of enhanced availability of surface layer nutrients for primary productivity.

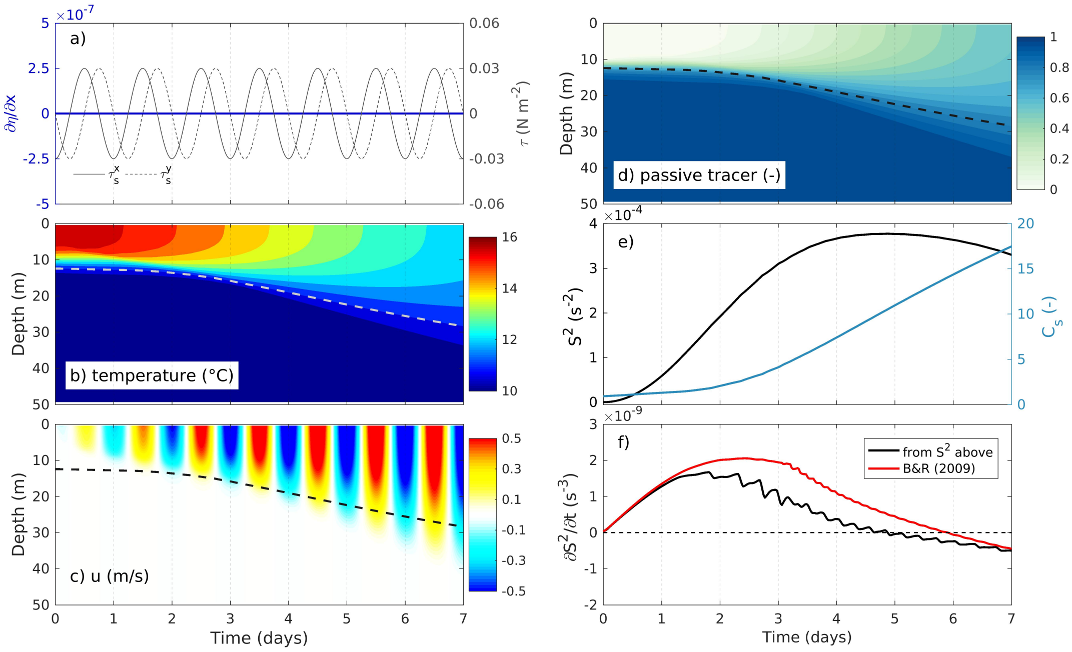

FIGURE 3.3: Open Ocean Case. (a) Wind stress components (τ_s^x, τ_s^y) and cross-shore surface elevation gradient forcing ($\partial\eta/\partial x$); (b) Vertical profile of temperature (the dotted line denotes the 11° C isotherm used as a proxy for the interface between the upper and lower layers); (c) Vertical profile of the cross-shore component of velocity (u); (d) Vertical profile of passive tracer concentration; (e) Bulk shear (S^2) and passive tracer integrated over the surface layer (C_s); (f) Bulk shear production ($\frac{\partial S^2}{\partial t}$) computed from both the model output and from the theory of Burchard and Rippeth (2009) (Equation 3.11). Results are computed from a 7 day integration of the 1D-vertical model with input parameters τ^{ac0} = 0.03 N m^{-2}, $\frac{\partial \eta}{\partial x} = 0$ (excluding the land boundary effect), latitude = 30° S, initial MLD =10 m, initial stratification = 6° C, water depth = 50 m.

3.3 Results

3.3.1 Diurnal-inertial resonance and mixing

Open ocean case

We begin by considering a two layer system forced by a constant amplitude diurnal anticlockwise rotating wind stress at 30° S, in the absence of a land boundary ($\partial\eta/\partial x = 0$). The amplitude of the applied wind stress is 0.03 N m^{-2}, being typical of the amplitude of the diurnal anticlockwise rotary component of the wind stress (τ^{ac0}) over St Helena Bay (Figure 3.14). Figure 3.3 shows the input forcing time-series for the model, the evolution of the resulting temperature and cross-shore velocity profiles, and the diapycnal mixing diagnostics described in Section 3.2.5. A diurnal anticlockwise rotating wind stress at 30° S represents the pure case of diurnal-inertial resonance, as the wind stress is always aligned with the surface inertial oscillation and so the energy flux from the wind to the ocean ($\overrightarrow{\tau_s}.\overrightarrow{u_s}$) is maximised. Stratification between the surface and subsurface layers restricts the generation of wind-driven currents to within the surface mixed layer. In the absence of the land boundary effect subsurface currents are not generated. The impact of water depth is therefore negligible in this experiment. The enhancement of the surface inertial oscillation is accompanied by the deepening of the thermocline and the cooling of the surface waters due to the entrainment of sub-thermocline waters. The simulation indicates a steady enrichment of the surface layer with the subsurface tracer, as evidenced by the increase in C_s over the simulation. The enhanced diapycnal mixing is driven by elevated bulk shear, which is shown to increase rapidly over the first few days of the simulation, peaking at day $\sim$5, before decreasing thereafter.

Although the bulk shear production computed directly from the model is consistently higher than that predicted by the analytical theory of Burchard and Rippeth (2009) (Figure 3.3f), the results suggest that Equation 3.11 provides a useful lens through which to interpret the results. The initial increase in bulk shear is explained by the perfect alignment of the surface wind stress ($\overrightarrow{\tau_s}$) with the surface current ($\overrightarrow{u_s}$) and therefore the bulk shear vector ($\overrightarrow{S}$). The enhanced bulk shear drives an increase in interfacial mixing (represented by the last term in Equation 3.11) as well as an increased depth of the surface layer (H_s), both of which serve to reduce bulk shear production. The bottom shear stress term is negligible in this simulation due to the absence of a subsurface oscillation. Bulk shear production lowers to zero when the interfacial mixing term balances the wind stress input term. In this way interfacial mixing represents a mechanism which limits the amplitude of the surface layer inertial oscillation.

It should be noted that simulations forced with a diurnal clockwise rotating wind stress at 30° S yield negligible current response as the winds continually dampen the rotating surface inertial oscillation, which by definition has an anticlockwise sense of rotation in the southern hemisphere. Figure 3.4 provides an example of such a case, and serves as a reference experiment for background levels of mixing in the

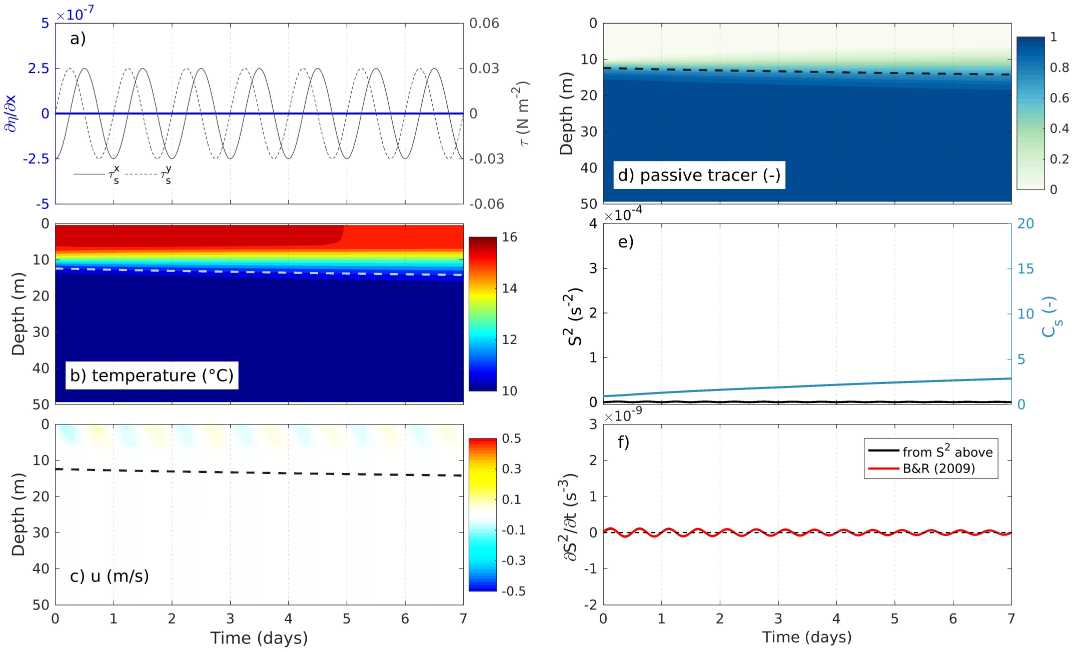

FIGURE 3.4: As per Figure 3.3, but with the 1D-vertical model now integrated with clockwise rotating wind stress forcing. Inertial oscillations are not generated.

absence of any notable current forcing.

The land boundary effect

Figure 3.5 builds on the model presented in Figure 3.3 by including the effect of the land boundary through the ‘Craig approximation’ for coast-normal surface elevation gradient response (Equation 3.8). For the considered case of pure diurnal-inertial resonance, $\frac{\partial \eta}{\partial x}$ is in phase with the cross-shore component of the wind stress (τ_s^x), generating a barotropic current response in the opposite direction to the surface inertial oscillation. The result is a significantly weakened surface inertial oscillation when compared to Figure 3.3, and the generation of a subsurface oscillation with a 180° phase shift to the surface layer. At the start of the simulation, bottom friction is negligible and $\frac{\partial \eta}{\partial x}$ is determined from the wind stress terms of Equation 3.8 alone. As the subsurface oscillation increases in amplitude, so do bottom friction losses, serving to further enhance $\frac{\partial \eta}{\partial x}$ (as dictated by Equation 3.8), thereby dampening the surface oscillation. For the shown example, the bottom friction terms of Equation 3.8 approximately double the amplitude of $\frac{\partial \eta}{\partial x}$ before the solution stabilises.

A comparison of the mixing diagnostics from Figures 3.3 and 3.5 shows that forcing

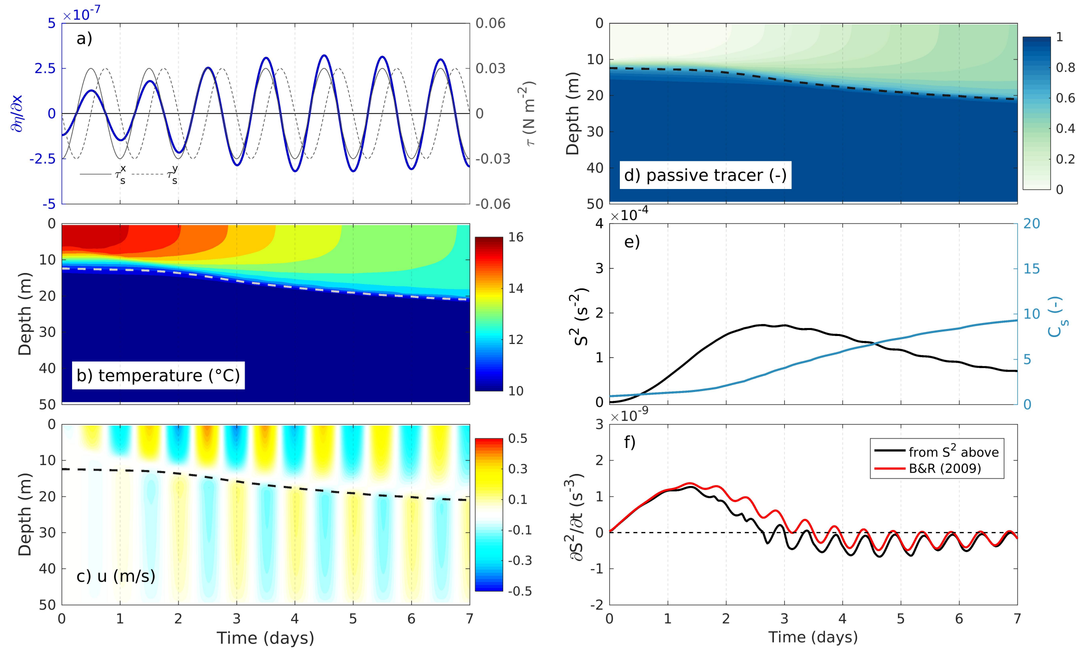

FIGURE 3.5: Effect of land boundary. Same as Figure 3.3 but with the 1D-vertical model now integrated including the 'Craig approximation' for coast-normal surface elevation gradient response (Equation 3.8).

the model with the 'Craig approximation' serves to significantly reduce bulk shear and therefore diapycnal mixing. For the shown example, C_s at 7 days is approximately halved through the inclusion of the land boundary effect. The evolution of bulk shear can again be interpreted using the bulk shear production theory of Burchard and Rippeth (2009). In addition to the processes already described for Figure 3.3, the subsurface oscillation generated by the 'Craig approximation' introduces a non-negligible bottom shear stress ($\overrightarrow{\tau_b}$) which is at all times directly opposed to the surface shear stress ($\overrightarrow{\tau_s}$). Equation 3.11 dictates that bulk shear production, and therefore diapycnal mixing, will be reduced as the cross-shore surface elevation gradient is enhanced.

It is important to note that the model solution results in near-zero depth averaged cross-shore transport, in line with the assumptions made in the formulation of the analytical theory for $\frac{\partial \eta}{\partial x}$ (Section 3.2.3). The bottom friction terms in Equation 3.8 are instrumental in this regard, as they account for bottom friction losses in the subsurface layer by amplifying $\frac{\partial \eta}{\partial x}$. In the absence of bottom friction terms in Equation 3.8, surface layer current velocities are over-estimated leading to a violation of the assumption of zero cross-shore transport, and the over-prediction of diapycnal mixing,

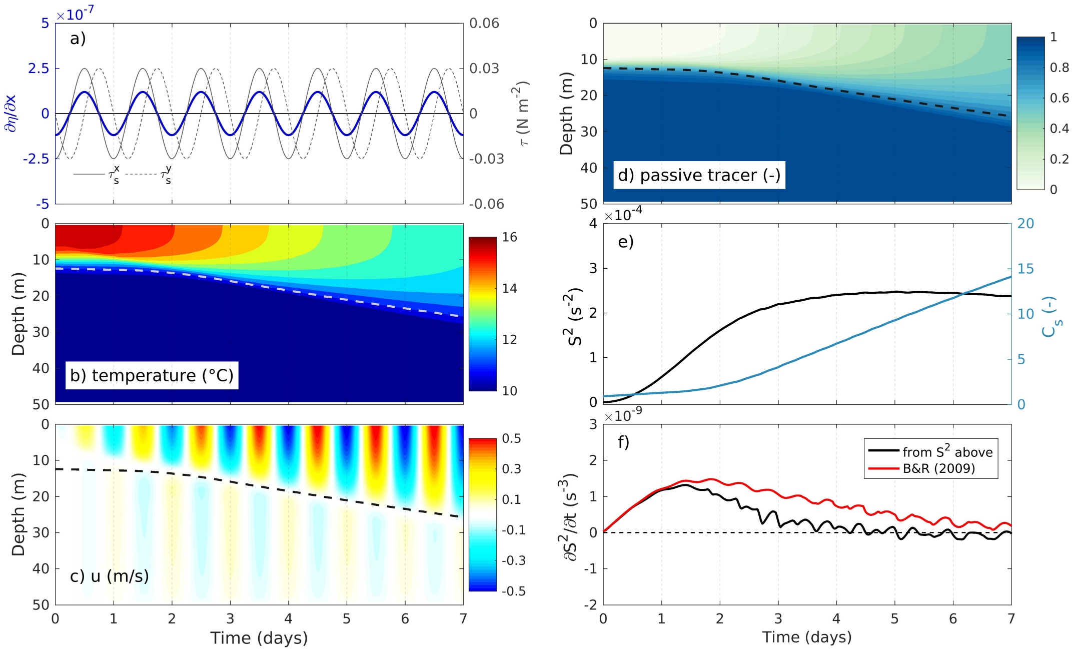

FIGURE 3.6: As per Figure 3.5, but with the 1D-vertical model now integrated excluding bottom friction terms in computing $\frac{\partial \eta}{\partial x}$ from Equation 3.8. The zero depth-average cross-shore transport assumption is violated.

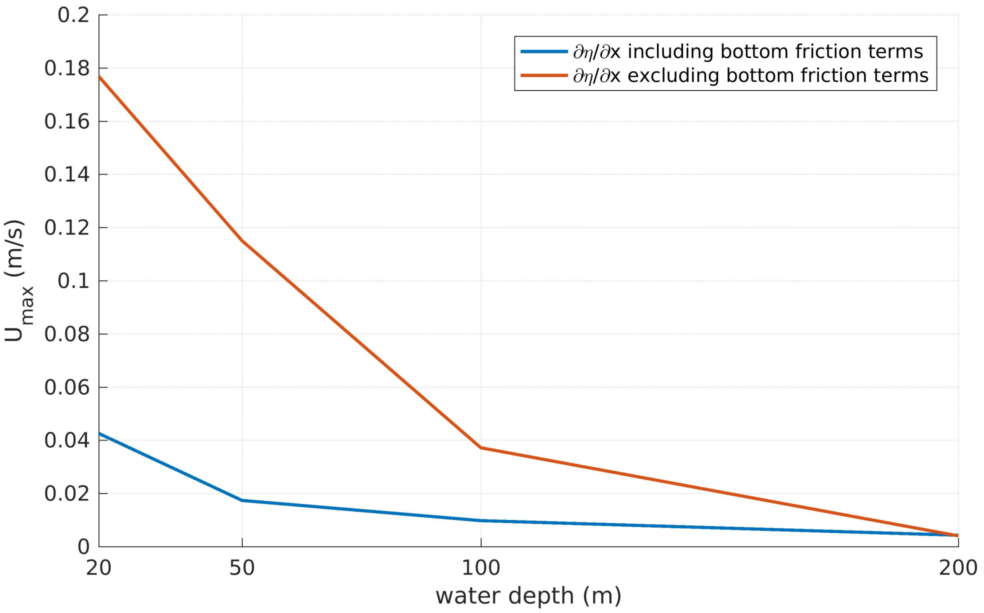

FIGURE 3.7: Sensitivity of the depth averaged velocity U_{max} to water depth for experiments shown in Figures 3.5 and 3.6. U_{max} is computed as the maximum depth averaged cross-shore velocity over the fifth day of the simulation. Note that $\frac{\partial \eta}{\partial x}$ is derived under the assumption of zero depth averaged cross-shore velocity and significant deviation of U_{max} from zero represents a violation of this assumption.

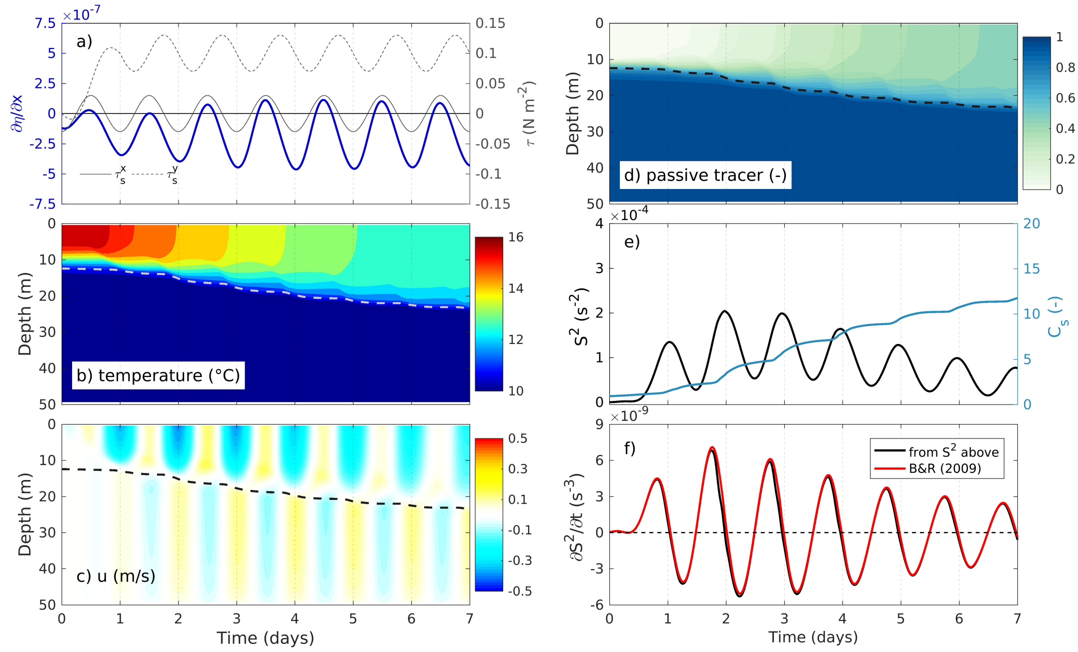

FIGURE 3.8: Effect of Ekman transport. Same as Figure 3.5, but with the 1D-vertical model now integrated including a mean alongshore wind stress ($\overline{\tau}_s^y$) of 0.1 N m^{-2}.

as shown in Figure 3.6. Sensitivity tests indicate that bottom friction terms become negligible for maintaining near-zero cross-shore transport for water depths greater than ∼200 m (Figure 3.7).

Effect of Ekman transport

The results thus far have considered only a diurnally rotating wind stress of constant amplitude, representative of the land-sea breeze. Upwelling systems are however also defined by sustained alongshore wind stresses. Figure 3.8 builds on the model presented in Figure 3.5 by including the effect of a mean alongshore wind stress ($\overline{\tau}_s^y$) of 0.1 N m^{-2}, representative of a relatively strong alongshore wind stress over St Helena Bay (Figure 3.14). The classic case of Ekman transport in response to a constant τ_s^y of 0.1 N m^{-2} is provided in Figure 3.9. The inclusion of a mean alongshore wind stress is shown to introduce a mean surface transport in the offshore direction, consistent with Ekman theory, with the surface inertial oscillation superimposed onto the offshore transport (Figure 3.8c). The bulk shear time-series (Figure 3.8e) is characterised by a pronounced diurnal signal, or 'shear spikes' at the inertial frequency to use the terminology of Burchard and Rippeth (2009). The diurnal variability in bulk shear is superimposed onto a sub-inertial signal similar to that shown in Figure 3.5, namely that of an initial increase in shear followed by a subsequent decrease from day ∼3 onwards. The sub-inertial variability in shear has been explained above, while the diurnal variability can again be interpreted using the bulk shear production theory of Burchard and Rippeth (2009). Bulk shear production (Figure 3.8f) is shown to be maximised when the y component of the wind stress (τ_s^y) is highest, as at these times $\overrightarrow{\tau_s}.\overrightarrow{S}$ is maximised. Bulk shear production becomes negative at times when the surface current and wind stress are opposed. Bulk shear is maximised at a phase $\frac{\pi}{2}$ (6 hours) after the peak in bulk shear production, as this is when the surface inertial oscillation is aligned with the sub-inertial Ekman transport. The diurnal peaks in bulk shear are coincident with bursts of diapycnal mixing that inject the subsurface tracer into the surface layer. Although the impact on bulk shear and diapycnal mixing is significant at the diurnal time-scale, the net tracer injection into the surface layer (C_s) is very similar to the simulation excluding the alongshore wind stress (Figure 3.5).

3.3.2 Case study of St Helena Bay

Comparison with observations

We now turn to the nearshore observations in St Helena Bay and assess the extent to which the simple 1D-vertical model dynamics described above can explain the observations. Figure 3.10 presents the evolution of observed and modelled temperature and velocity through the water column over the considered upwelling/mixing event. This event was specifically identified as a period where the observations clearly demonstrate the response of a highly stratified two layer system to the onset of upwelling favourable winds with an anticlockwise sense of rotation (Lucas et al., 2014). The temperature initial condition for the model was interpolated directly from the observations, while hourly wind stress and heat flux forcing for the model were derived from the CSAG WRF simulation at the location of the observations (τ^{real} in Figure 3.1).

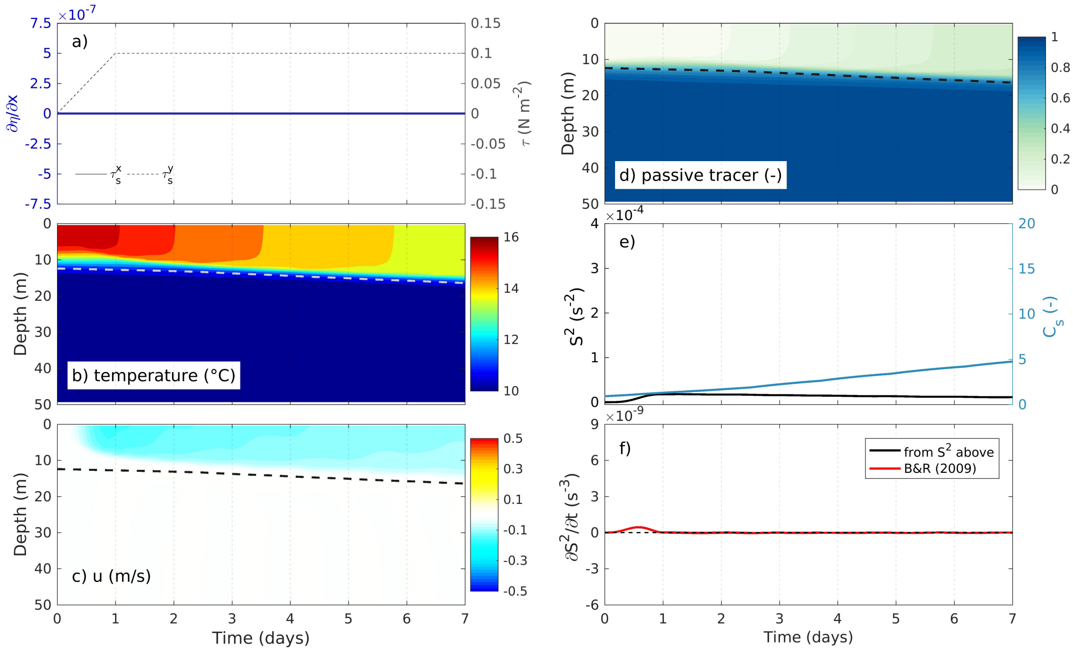

FIGURE 3.9: As per Figure 3.8, but with the 1D-vertical model now integrated with a constant alongshore wind stress and ignoring the land boundary effect. Classic Ekman theory predicts a cross-shore surface layer transport ($M_E^x = \frac{\tau_s^y}{\rho f}$) of -1.34 m^2 s^{-1}, which is predicted by the model to within 1.5%. The constant wind stress is spun-up smoothly from rest over 1 day.

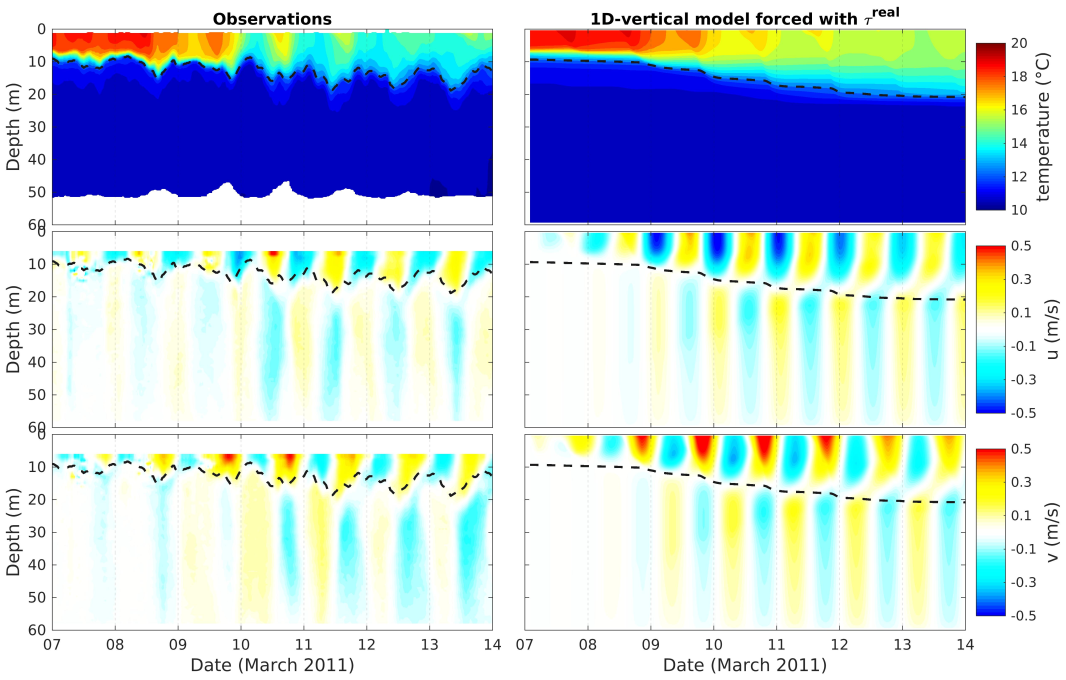

FIGURE 3.10: Observed (left) and modelled (right) temperature and velocity components over an upwelling event accompanied by diapycnal mixing in ~60 m water depth in St Helena Bay ('WW' Station 1 in Figure 1.2). The dotted line denotes the 12.5° C isotherm used as a proxy for the interface between the upper and lower layers.

The model reproduces the observed two layer system comprised of anticlockwise oscillations at the diurnal-inertial frequency in both surface and subsurface layers with a 180° phase shift between the two. The contamination of the surface ADCP data complicates a direct comparison of modelled and measured surface currents, however the amplitudes and phases are shown to be in surprisingly good agreement, considering the simplified physics of the model. The reasonable representation of subsurface velocities through the 'Craig approximation' provides some confidence in the methodology as applied in this chapter. The good agreement may be surprising given that the 2D model experiments of Hyder et al. (2011) suggested that the 'Craig approximation' is not valid near the coast ($<$ 140 km) where non-linear terms cannot be ignored. Given that the observations are $\sim$12.7 km from the coast, significant deviations in surface elevation gradient from linear theory are expected at this location, however our results suggest that the net subsurface current response is predominantly driven by the linear physics of the theory. It is noted that the inclusion of the bottom friction terms in Equation 3.8 significantly improved the realism of the model, given the $\sim$60 m water depth of the observations.

Both the observations and the model indicate a rapid increase in surface current amplitude until $\sim$11 March, followed by a subsequent decrease. The onset of enhanced surface currents is accompanied by a deepening of the thermocline and a lowering of surface layer temperatures, consistent with the effects of diapycnal mixing. The model over-estimates the deepening of the thermocline, however the net cooling of the surface layer is somewhat contradictorily under-estimated. The observations reveal strong diurnal-inertial variability in surface temperature, particularly over the period 09-12 March, which is not reproduced in the model. The model does include a diurnal signal of surface layer warming due to the heat flux input, however the combination of mixing and heating alone cannot explain the observed diurnal variability. These discrepancies point to the presence of vertical and horizontal advection driven variability in the observations which is not included in the physics of the model. A further important difference between the model and the observations is that the observations include significant vertical displacements of the thermocline

($\sim$5 m amplitude) with a diurnal frequency which are absent in the model. This indicates the presence of near-inertial internal waves, generated by the convergence and divergence of the forced response near the land boundary, which are by definition not included in the physics of the model.

Figure 3.11 presents the evolution of bulk shear (S^2) as derived from the data shown in Figure 3.10. The computation of $\overrightarrow{u_s}$ from the ADCP data required the filling of contaminated surface layers with data from the uppermost bin considered to contain good data. This is likely to result in an under-estimation of surface layer velocities (and therefore bulk shear) computed from the observations. The bulk shear vector computed from the measurements was low-pass filtered to remove frequencies higher than 12 hours. The progressive displacement plots show the surface layer currents to be comprised of inertial oscillations superimposed onto a background mean flow. The modelled mean flow is perpendicular to the left of the major axis of the wind variability (Figure 3.1), consistent with Ekman transport. There is a difference in the orientation of the mean flow between the observations and the model, likely reflecting an error in the mean wind direction of the WRF model with respect to the actual winds over this event. Both the observations and the model show strong diurnal variability in bulk shear. The amplitude and timing of the 'shear spikes' in the model and the observations are in reasonable agreement. Four 'shear spikes' have been identified (labelled 1-4) and are indicated on the progressive displacement plots. In both the observations and the model, the 'shear spikes' are shown to occur when the oscillation and the mean flow are aligned leading to enhanced surface layer velocities and therefore bulk shear, consistent with the analytical configurations described in Section 3.3.1. The diurnal variability in bulk shear is superimposed onto a sub-inertial signal which indicates an increase in bulk shear until 10-11 March followed by a subsequent decrease, which is again consistent with the physics described for the analytical configurations. Comparison of the bulk shear production computed from the observations and the theory of Burchard and Rippeth (2009) (Figure 3.11c) reveals that the timing of the diurnal peaks is not always consistent. This could again be largely explained by errors in the WRF model wind direction over this event, as the theoretical bulk shear production is computed from

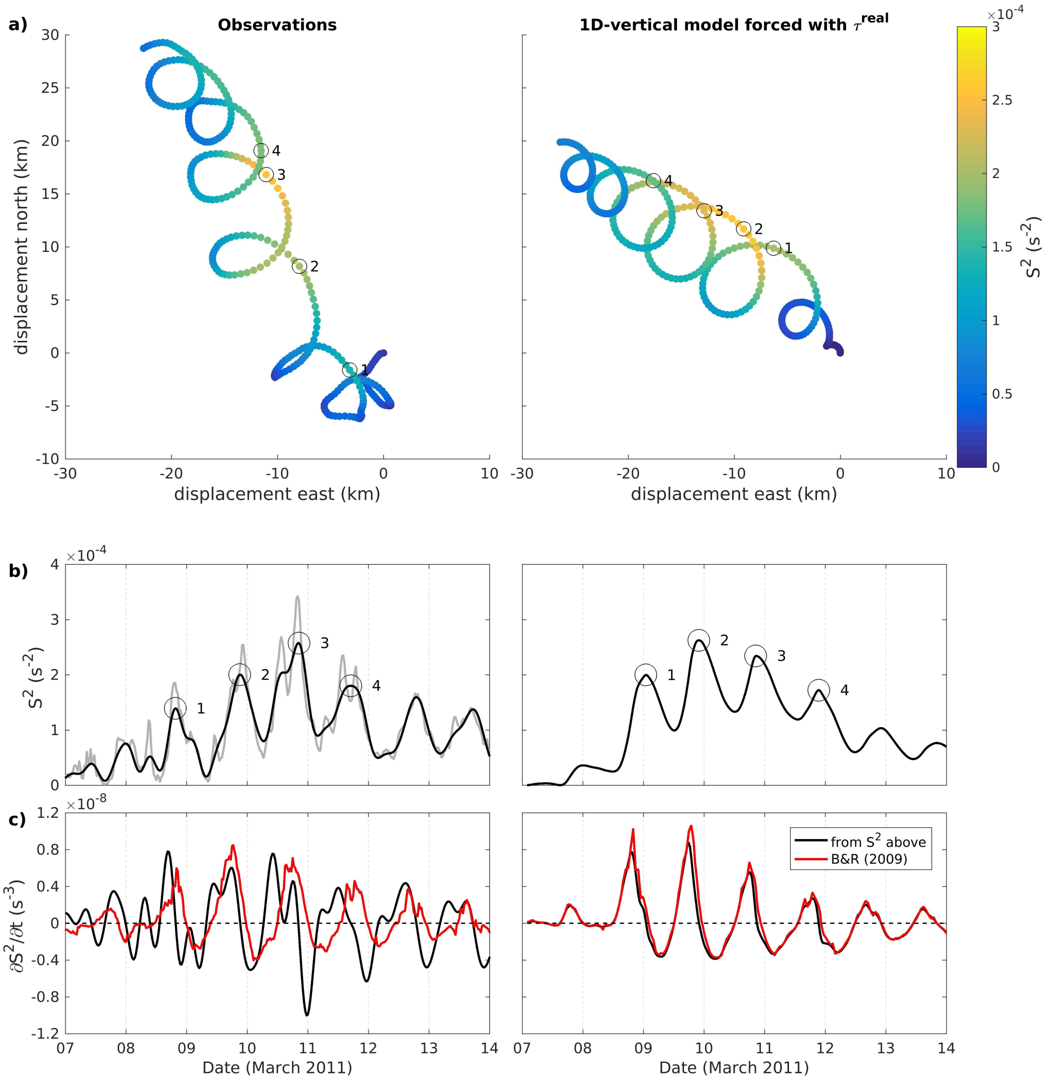

FIGURE 3.11: Observations (left) versus 1D-vertical model (right) during the event shown in Figure 3.10. (a) Progressive displacement plots derived from surface layer velocities ($\overrightarrow{u_s}$). (b) Time-series of bulk shear (S^2). The grey line shows the unfiltered bulk shear derived from the observations while the black line shows the low-pass filtered data. (c) Time-series of bulk shear production ($\frac{\partial S^2}{\partial t}$) computed from the observations (left), model output (right), and the theory of Burchard and Rippeth (2009).

the dot product of the WRF model wind stress and the observed bulk shear vector (Equation 3.11). The bulk shear production computed from the model is however in good agreement with the theory.

τ^{ac0} as a diagnostic for diapycnal mixing

The comparison of the realistic model configuration with the observations shown above was carried out using realistic wind stresses (τ^{real}), while the analytical model configurations presented in Section 3.3.1 were carried out using a constant amplitude anticlockwise rotating wind stress (τ^{ac}). Figures 3.12 and 3.13 present results for simulations forced with both τ^{real} and τ^{ac}, respectively, to ascertain the extent to which τ^{ac} alone contributes to diapycnal mixing over the event. τ^{ac} for this simulation was computed from the 7 day period of 7-14 March 2011, as depicted by the red circle in Figure 3.1. The notable difference between the simulations is the absence of diurnal 'shear spikes' in the simulation forced with τ^{ac} alone. In the absence of Ekman transport (τ^{ac} has a mean wind stress of zero), the mechanism for the generation of diurnal 'shear spikes' through the superposition of the mean flow and the inertial oscillations is no longer present. The sub-inertial evolution of bulk shear is however quite similar between the two simulations. Despite the large differences in the magnitude of the applied surface wind stresses (τ^{real} attains a maximum value of $\sim$0.15 N m^{-2} while τ^{ac} has a constant amplitude of 0.03 N m^{-2}), the cumulative diapycnal mixing response as revealed by C_s is comparable between the two simulations. The results therefore suggest that the amplitude of τ^{ac} (τ^{ac0}) can be used as a reasonable diagnostic for event-scale diapycnal mixing in response to the land-sea breeze. 'Shear spikes' introduced by the interaction of the surface inertial oscillation with the Ekman transport are shown to play a secondary role.

As τ^{ac0} represents a diagnostic for diapycnal mixing, the spatial and seasonal variability of this parameter over St Helena Bay has been assessed, as shown in Figure 3.14. The monthly climatology of τ^{ac0} computed at the location of the Lucas et al. (2014) observations (Figure 3.14a) reveals a distinct seasonality in the land-sea breeze, with a peak coinciding with the austral summer (November - January). This

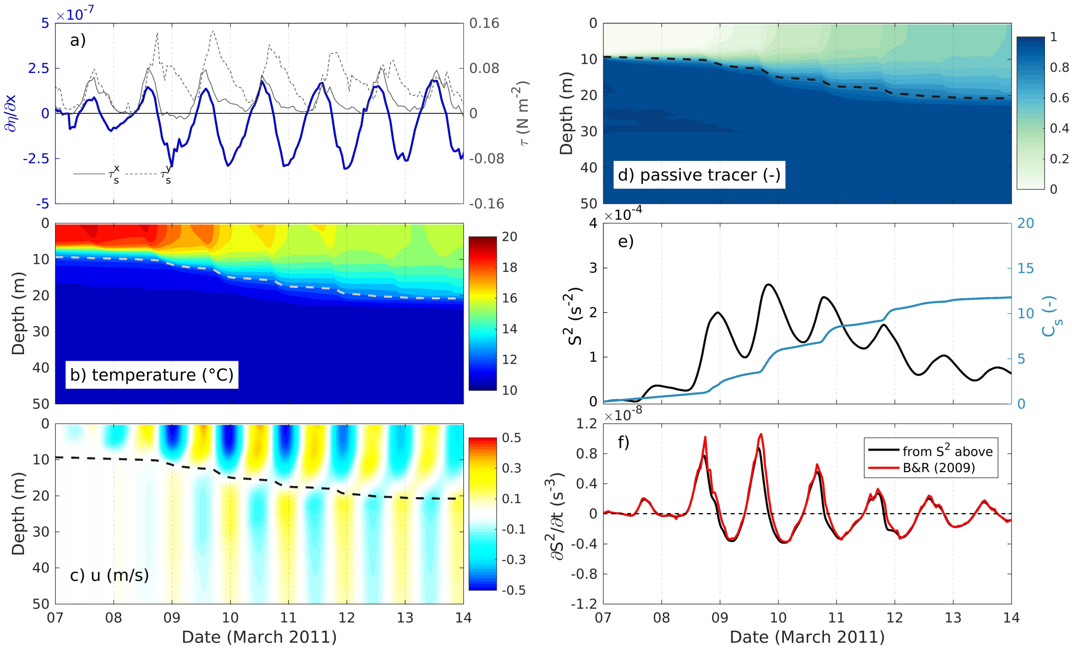

FIGURE 3.12: Realistic model configuration for comparison with observations.

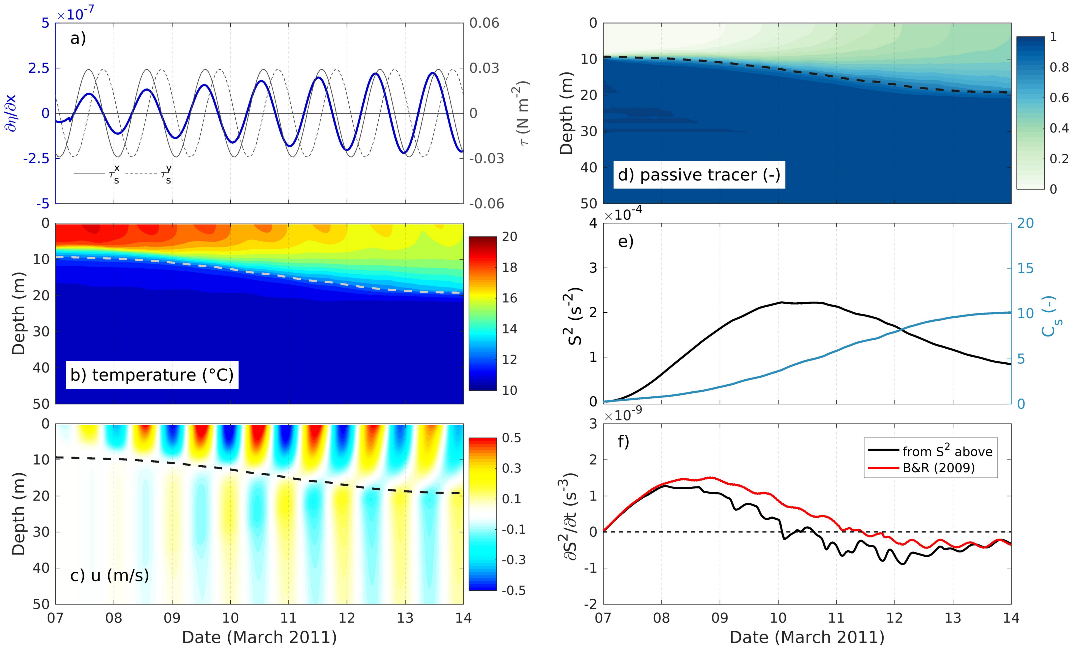

FIGURE 3.13: As per Figure 3.12 but forced with the diurnal anti-clockwise rotary component of the wind stress (τ^{ac}).

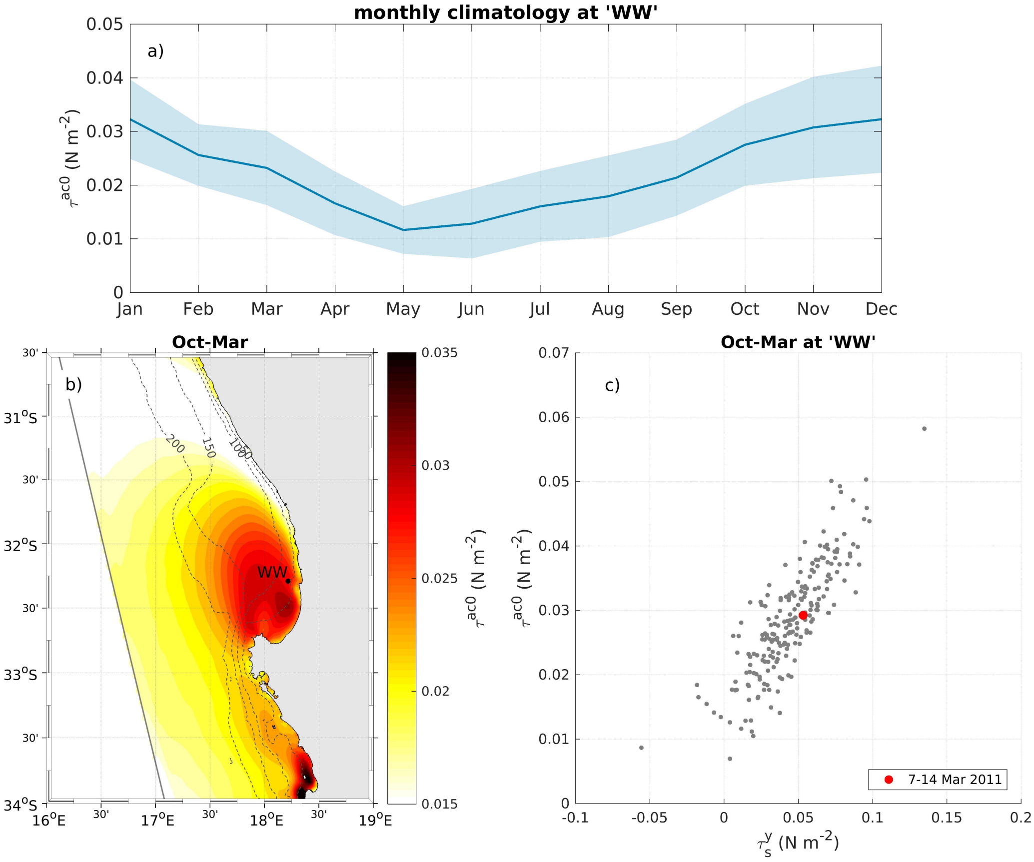

FIGURE 3.14: Spatial and seasonal variability in the amplitude of the diurnal anticlockwise rotary component of wind stress (τ^{ac0}) over St Helena Bay. τ^{ac0} has been estimated from consecutive 7 day windows over the 8 year duration of the 3 km resolution WRF simulation described in Section 3.2.1. (a) Monthly climatology of $\tau^{ac0} \pm 1\ \sigma$ at the location of the Lucas et al. (2014) observations ('WW'). (b) Spatial variability in the six month climatology of τ^{ac0} over the upwelling favourable months of October to March. Overlain are the bathymetric contours. (c) Scatter plot of τ^{ac0} vs the 7 day mean alongshore wind stress (τ_s^y) at the location of the Lucas et al. (2014) observations ('WW') over the upwelling favourable months of October to March.

seasonality corresponds to that of the upwelling favourable winds in the region. Figure 3.14c reveals that τ^{ac0} and τ_s^y are strongly correlated, indicating that periods of enhanced inertial oscillations are coincident with enhanced upwelling. The period coinciding with the historical mixing/upwelling event considered in this study (7-14 March 2011) is highlighted and shown to be typical in terms of both upwelling and land-sea breeze forcing. The spatial variability in τ^{ac0} (Figure 3.14b) indicates a strong amplification of the land-sea breeze over St Helena Bay. The orographic effects of Cape Columbine and high spatial variability in coastal sea surface temperatures in this region have been shown to significantly influence the spatial variability of low level winds (Burls and Reason, 2008), and are likely to be responsible for the shown amplification.

3.3.3 Sensitivity experiments

Various sensitivity experiments have been carried out with the analytical model configuration in an attempt to generalise the results of the model. The baseline configuration employs the input parameters: latitude = 30° S, initial MLD = 10 m, ΔT = 6° C and water depth = 100 m. The 'Craig approximation' for the cross-shore free surface elevation gradient is included in these experiments. Figure 3.15 presents the sensitivity of the model to varying each of these parameters, as quantified through the amplitude of the surface layer velocity ($|\overrightarrow{u_s}|$) and the passive tracer integrated over the surface layer (C_s), both averaged over the fifth day of each simulation. Results are presented for a range of amplitudes of diurnal anticlockwise rotating wind stress (τ^{ac0}), being typical of those experienced over St Helena Bay (Figure 3.14).

Figure 3.15a indicates a strong dependence of both $|\overrightarrow{u_s}|$ and C_s on latitude with the peak response at the critical latitude of 30° S. The inertial response is shown to drop off within 6° latitude either side of the critical latitude. The approximate latitude of St Helena Bay (SHB) is shown for reference, indicating that this site experiences near-peak response to diurnal forcing. For τ^{ac0} = 0.01 N m^{-2} the shear generated by the surface inertial oscillation is not high enough to trigger diapycnal mixing above background levels. Increasing τ^{ac0} leads to an increase in $|\overrightarrow{u_s}|$ and C_s, however the amplitude of the surface oscillation is limited by enhanced diapycnal mixing,

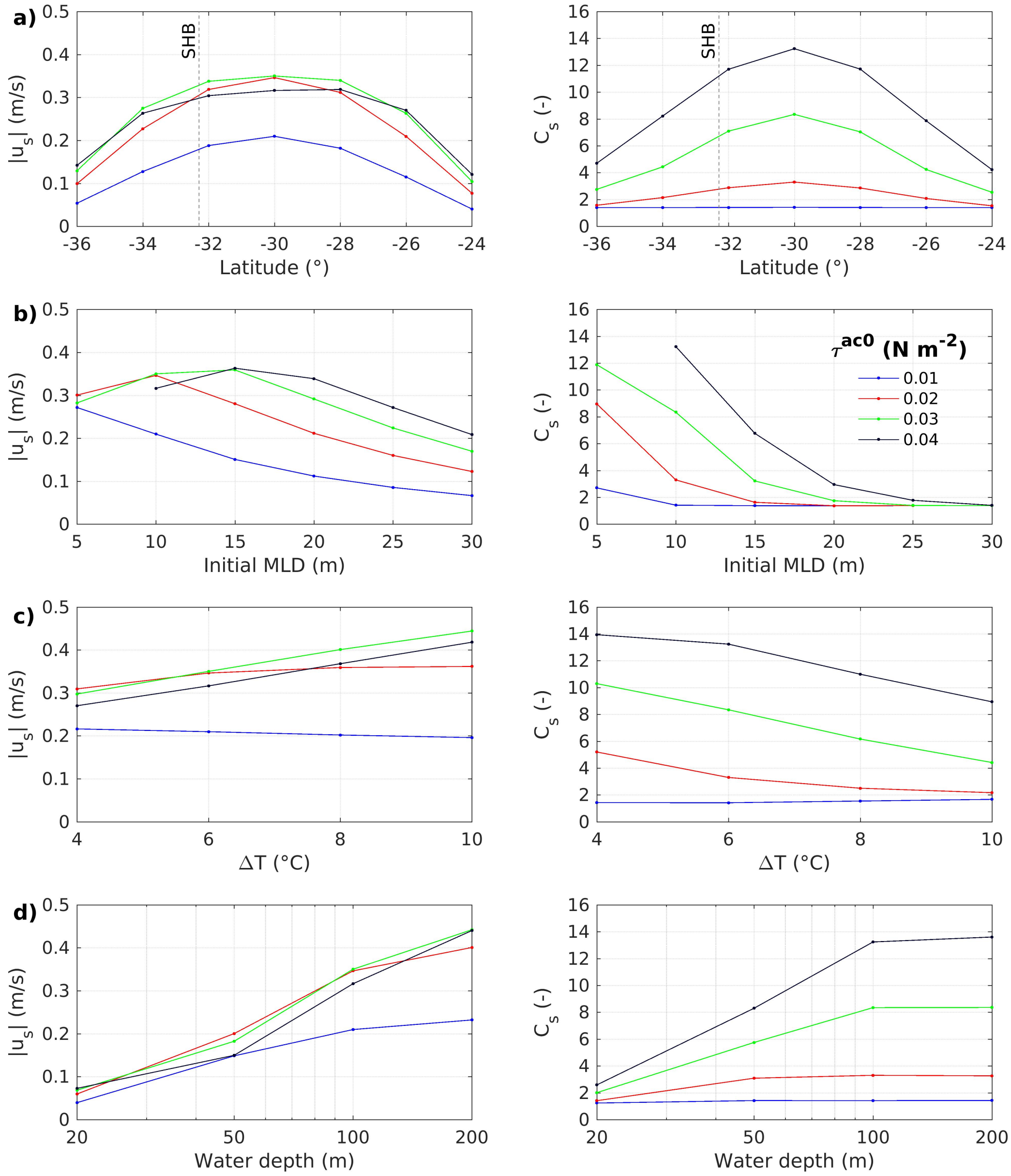

FIGURE 3.15: Sensitivity of the analytical model configuration, as quantified through the amplitude of the surface layer velocity ($|\overrightarrow{u_s}|$) and the passive tracer integrated over the surface layer (C_s), both averaged over the fifth day of each simulation. (a) Sensitivity to latitude. (b) Sensitivity to initial mixed layer depth (MLD). (c) Sensitivity to stratification (ΔT represents the temperature difference between surface and subsurface layers). (d) Sensitivity to water depth. The different colour lines correspond to different wind stress amplitudes.

as dictated by bulk shear production theory used to interpret the results shown in Section 3.2.5.

The sensitivity of the model to initial MLD and stratification (Figure 3.15b and 3.15c) can be largely understood in terms of the gradient Richardson number, $Ri = N^2/S^2$ which quantifies the balance of stabilising forces due to stratification (N^2) and the destabilising forces due to vertically sheared flow (S^2). Shallower surface mixed layers lead to higher amplitude surface currents and therefore enhanced shear. A given stratification can only sustain a defined shear before Ri is reduced sufficiently to trigger diapycnal mixing. Exaggerated mixing serves to dampen the amplitude of the surface oscillation as already described in Section 3.3.1. Diapycnal mixing is therefore particularly sensitive to initial MLD, while the surface current amplitude is modulated and even reduced in cases of exaggerated mixing. Note that the result for $\tau^{ac0} = 0.04$ N m^{-2} and initial MLD = 5 m is not plotted as excessive mixing effectively eroded the two layer system to form a homogeneous water column with temperatures of between 10 and 11° C. The results indicate that event-scale diapycnal mixing reduces to background levels for MLD's greater than $\sim$30 m. Elevated stratification has a dampening effect on diapycnal mixing, while allowing for higher amplitude currents to be sustained in the surface layer. Surface current amplitude is however insensitive to stratification for low wind stress amplitudes which do not drive exaggerated mixing, as the depth of the surface layer remains largely unchanged over these simulations. The initial MLD therefore has a primary role in governing the diapycnal mixing response to diurnal-inertial resonance, while stratification plays a secondary modulating role.

Figure 3.15d shows that shallower water depths lead to significantly reduced surface current amplitudes and mixing. The formulation for the 'Craig approximation' (Equation 3.8) dictates that shallower water depths have an amplifying effect on $\frac{\partial \eta}{\partial x}$. As already described in Section 3.3.1, this has a dampening effect on both the amplitude of the surface layer oscillation as well as diapycnal mixing. Simulations run at 20 m water depth are shown to result in very low amplitude oscillations ($|\overrightarrow{u_s}|$ <0.1 m/s for all tested wind stress amplitudes), and a complete dampening of diapycnal mixing to near-background levels. The C_s results from Figure 3.15d at 100 m are very similar to those at 200 m, indicating that the impact of the land boundary on diapycnal mixing from the locally generated inertial response becomes negligible for water depths greater than ∼100 m.

3.4 Discussion and conclusions

3.4.1 Diapycnal mixing dynamics

Despite the simplicity of the 1D-vertical model introduced in this chapter, the results of the realistic configuration are in good agreement with nearshore observations over an upwelling event accompanied by diapycnal mixing in ∼60 m water depth in the southern Benguela upwelling system. One of the main limitations of applying 1D models to study diurnal-inertial resonance near a land boundary is the difficulty in reproducing the first baroclinic mode vertical structure of the currents (Zhang et al., 2010). Here we address this limitation through the implementation of the 'Craig approximation' for first order surface elevation gradient response, extending the formulation of Simpson et al. (2002) through the inclusion of bottom friction terms. The results of the model have been interpreted using the bulk shear production theory of Burchard and Rippeth (2009). This work represents the first application of this theory in the context of diurnal-inertial resonance near the critical latitude of 30° N/S. The theory dictates that bulk shear will be produced (and mixing enhanced) when the bulk shear vector is aligned with the surface and bottom shear stresses, weighted by the depth of the two layers, and moderated by interfacial mixing. Near latitudes of 30° N/S, the diurnal anticyclonic rotary component of the wind is always in alignment with the bulk shear vector induced by the presence of inertial oscillations, which provides a constant source of bulk shear production. The effect of the land boundary is to generate a subsurface oscillation with a 180° phase shift with the surface layer, thereby introducing bottom shear stresses in the opposite direction to the surface stresses. The latter has a dampening effect on bulk shear production (Figure 3.5), which in turn reduces diapycnal mixing. The land boundary effect becomes increasingly important for shallow water depths (<∼100 m), where bottom friction losses serve to amplify the response of the cross-shore surface elevation gradient, which in turn further dampens the amplitude of the surface inertial oscillations. For depths $<\sim$100 m, the introduction of bottom friction terms in the formulation of the 'Craig approximation' is crucial for achieving realistic currents and mixing in the model through the maintenance of near-zero depth averaged cross-shore transport. Diapycnal mixing is reduced to near-background levels in water depths of $\sim$20 m (Figure 3.15d). In this way, the first order response of the cross-shore surface elevation gradient offers a mechanism for contributing to the well known decrease in near-inertial energy towards the coast (Shearman, 2005; Chen and Xie, 1997; Xing et al., 2004).

Many previous studies cite the 180° phase shift between surface and subsurface layers, introduced by the land boundary, as a source of shear and mixing. This is seemingly in contrast with our results which suggest that the land boundary has a dampening effect on diapycnal mixing associated with the forced response to the land-sea breeze. It is however important to emphasise that the 1D-vertical model excludes propagating near-inertial first baroclinic mode internal waves. These waves are known to be generated by the inertial pumping of the thermocline due to convergence and divergence of the forced response at the land boundary (Millot and Crépon, 1981; Tintoré et al., 1995; Chen et al., 2017; Kelly, 2019). The large vertical displacements of the thermocline as seen in the observations (Figure 3.10) provide evidence for the propagating near-inertial internal wave component in the observations. First baroclinic mode internal waves also introduce a 180° phase shift between surface and subsurface layers, which can be an important contributor to diapycnal mixing (Xing et al., 2004; Zhang et al., 2010). Separating the contribution of the internal wave component from the locally forced response described in this chapter is complicated by the similar vertical current structures and frequencies of these processes. The good agreement between observations and the 1D-vertical model however suggests that diapycnal mixing over the considered event was dominated by resonance between the local diurnal wind variability and the locally generated inertial oscillation, while the propagating near-inertial internal wave component was of lower importance. 2D numerical experiments designed to ascertain the diapycnal mixing contribution of near-inertial internal waves set up by diurnal-inertial resonance at a land boundary will be addressed in Chapter 4.

The introduction of a non-zero mean alongshore wind stress serves to introduce 'shear spikes' at the diurnal-inertial frequency, coinciding with times where the surface inertial oscillation and Ekman transport are aligned. While 'shear spikes' have been found to be important for driving diapycnal mixing and bloom enhancement in shallow stratified seas (Burchard and Rippeth, 2009; Lincoln et al., 2016; Williams et al., 2013), our results suggest that this process plays a secondary role in the integrated nutrient enrichment of the surface layer, when compared with the diurnal-inertial resonance phenomenon (Figure 3.13). It should however be noted that the timing of the diurnal 'shear spikes' in relation to sunlight availability would have consequences for the diurnal variability in phytoplankton growth. Both observations and model results indicate night time nutrient enrichment of the surface layer over the considered event (Figure 3.11), which would benefit phytoplankton growth during the following day.

3.4.2 Implications for St Helena Bay and EBUS generally

St Helena Bay is exposed to a pronounced enhancement of the diurnal anticlockwise rotary component of the wind stress (Figure 3.14), which has been shown to be a reasonable diagnostic for event-scale diapycnal mixing (Figure 3.13). Sensitivity tests to latitude (Figure 3.15a) indicate that St Helena Bay ($\sim$32.5° S) experiences near-peak inertial response to diurnal forcing. These results alone provide strong evidence for the forcing mechanism of the energetic diurnal-inertial current variability which has been observed in the bay (Fawcett et al., 2008; Lucas et al., 2014).

Productivity within St Helena Bay is largely understood in terms of the retentive properties of the bay which allow for the utilisation of upwelled nutrients during wind relaxation/reversal (Pitcher et al., 2010). As such, productivity tends to be highest in late summer when extended relaxation events following active upwelling allow for the formation of shallow stratified surface mixed layers, considered favourable for development of high biomass dinoflagellate blooms (Fawcett et al., 2007; Pitcher and Weeks, 2006; Pitcher et al., 2010). Shallow surface mixed layers have also been shown to be a key determinant for enhanced diapycnal mixing, as moderated by the level of stratification between surface and subsurface layers

(Figure 3.15b and 3.15c). Although relaxation events are generally associated with a lower amplitude land-sea breeze (Figure 3.14), even low amplitude diurnal wind variability would serve to moderate the formation of shallow surface mixed layers through the entrainment of subsurface waters and nutrients. Furthermore, successive events of enhanced diurnal wind variability would act on the inertial currents set up by the previous event, serving to further enhance the ocean response. The results presented in this chapter therefore provide further evidence that the land-sea breeze plays a major role in determining the evolution of primary productivity within St Helena Bay through surface layer nutrient enrichment.

A further consequence of enhanced subsurface near-inertial currents driven by the land-sea breeze is the contribution of elevated bed shear stresses toward the re-suspension of seabed sediment. The inertial oscillation-induced bed shear stresses would act in conjunction with those induced by surface gravity waves and also sub-inertial subsurface currents, which can be particularly enhanced during downwelling events (Kämpf, 2019). This process may further contribute to phytoplankton productivity in coastal upwelling systems through the introduction of regenerated nutrients (produced by benthic recycling) into the water column (Fanning et al., 1982; Herbert, 1999). Indeed, observations within St Helena Bay confirm that on-shelf trapping of remineralised nutrients enhances the nutrient pool in the subsurface waters of the bay (Flynn et al., 2020).

Given the significant impact of diurnal wind variability on the vertical water column structure, our results indicate that diapycnal mixing may have further implications for the nearshore sub-inertial upwelling/relaxation dynamics of St Helena Bay. Deeper surface mixed layers induced by nearshore mixing would reduce offshore surface Ekman velocities, thereby acting as a retention mechanism within the studied bay, and more generally in the EBUS regions. The modulation of cross-shore pressure gradients due to diapycnal mixing would also affect alongshore geostrophic currents and therefore bay-scale circulation. Observations in the Coastal Southern California Bight indicate that diurnal-inertial resonance can lead to steeper cross-shore isotherms and intensified alongshore flows (Nam and Send, 2013). These processes will be further investigated in Chapter 5.

Although this work has used St Helena Bay as a case study, the results and implications are transferable to other regions, as all four major EBUS include land-sea breeze forcing near the critical latitude. A dedicated analyses of the diurnal anticlockwise rotary component of the wind stress could highlight other regions where the local inertial response and diapycnal mixing could be enhanced. A general consideration for future studies is the requirement for atmospheric products of sufficient spatial and temporal resolution to capture the nearshore spatial variability in the land-sea breeze. This can be considerable where local orographic features and sea surface temperatures may significantly impact nearshore diurnal wind variability, as highlighted by Figure 3.14. Similarly, the spatial resolution of 3D ocean models is required to be sufficiently high so as to capture the spatial variability in the forced response to the land-sea breeze. The inability to resolve the nearshore features of the land-sea breeze and the associated ocean response may be a significant shortcoming in large scale models which aim at simulating productivity in coastal upwelling systems. This study suggests that the mostly affected regions would be those where the development of shallow surface mixed layers through retention coincide with the local amplification of the land-sea breeze.

Chapter 4

The internal wave response to the land-sea breeze near the critical latitude

4.1 Introduction

While the 1D-vertical model presented in Chapter 3 implicitly includes the effect of the land boundary through the first order surface elevation gradient response (i.e. the 'Craig approximation'), a significant shortcoming of the model was identified to be the exclusion of vertical thermocline displacements associated with horizontal convergence and divergence of the forced response at the land boundary. In this chapter we build on the 1D model experiments already presented, through the use of a 2D-vertical model which includes the cross-shore dimension. In so doing, we aim to elucidate dynamics of both the forced and the internal wave response in coastal upwelling systems due to land-sea breeze forcing near the critical latitude. The 1D model solution is used as a proxy for the forced response, while significant deviations from the 1D solution are used to identify the effects of the internal wave response induced by thermocline pumping at the land boundary. We use the 2D model to elucidate the effect of water depth, latitude and bottom slope on the cross-shore variability in currents, thermocline displacements and diapycnal mixing due to land-sea breeze forcing near the critical latitude. Analytically configured experiments for this purpose are set up in an analogous way to the 1D experiments described in Chapter 3, and we employ the 1D model solution as the offshore open boundary condition for the 2D model. We further explore the implications of the interaction of the inertial response with sub-inertial Ekman transport driven by an alongshore wind stress. Again, we turn to the observations of Lucas et al. (2014) for an assessment of a realistically configured 2D model, but extend the comparison to include all three Wirewalker moorings, as shown in Figure 4.1. The moorings are arranged roughly perpendicular to the local coastline orientation, making them particularly relevant for identifying the cross-shore processes highlighted by the analytically configured experiments.

4.2 Methods

4.2.1 Ocean model

The ocean model employed for the numerical experiments presented in this chapter is the full 3D version of the CROCO model described in Chapter 2.3. The model configuration as described below however effectively constitutes a 2D cross-shore model.

4.2.2 Model configuration

Both analytically and realistically configured experiments are employed in this chapter. The analytically configured experiments are designed to elucidate the processes of interest and to carry out sensitivity tests to relevant variables, while the realistically configured simulations compare the model solution to the observations of Lucas et al. (2014) over the period 7-14 March 2011, being the same period used for comparison with the 1D model in Chapter 3.

The model domain has dimensions of 100 km (E-W) $\times$ 2.5 km (N-S), and is discretised using a regular grid of 500 m resolution (i.e. a 200 $\times$ 5 grid). The number of sigma layers is defined to be equal to the water depth at the offshore boundary of the model. A baroclinic time-step of 40 s is used to integrate the model solution over a period of 7 days from initialisation, typical of the time-scale of upwelling events. 40 barotropic time-steps are computed within each baroclinic time-step. Instantaneous

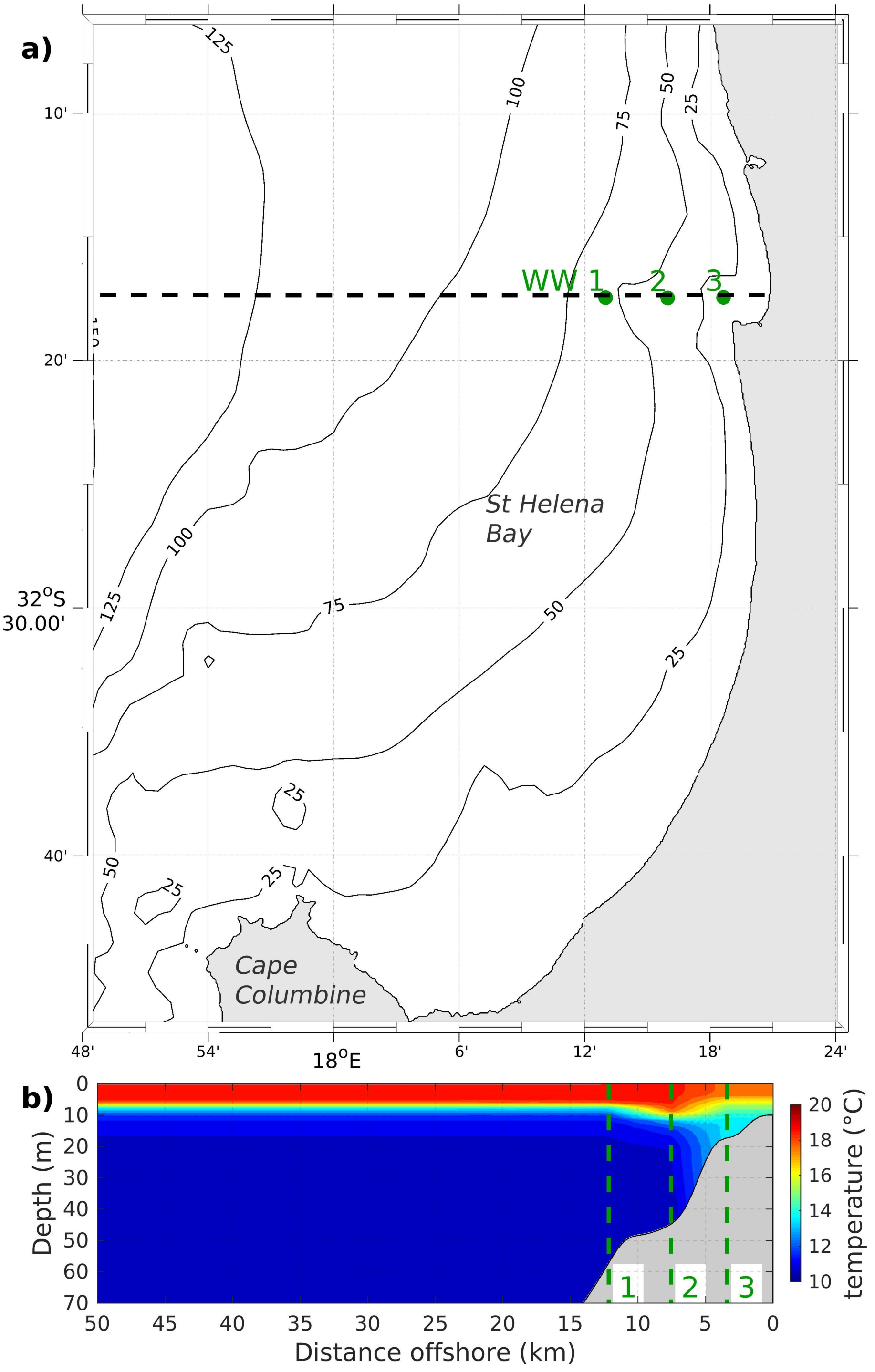

FIGURE 4.1: (a) Locality map for the Wirewalker (WW) moorings of Lucas et al. (2014). The black dotted line denotes the location of the section shown in (b). (b) Temperature section interpolated and extrapolated from the observations on 7 March 2011, used to initialise the realistically configured 2D-vertical model. Bathymetry is interpolated from digital navigational charts for the region provided by the Hydrographer of the SA Navy.

model output at 30 min intervals is filtered in time to provide a two hour running mean at each time-step, consistent with the processing of observations.

The northern and southern boundaries are defined as periodic boundary conditions, such that all the outflows (inflows) at the southern boundary are inflows (outflows) at the northern boundary. The eastern boundary is defined as a closed land boundary, while the western boundary is applied as an open boundary condition. The open boundary requires the prescription of temperature (T), salinity (S), velocity components (u, v) and a passive tracer (C) used as a proxy for subsurface nutrients. The prescribed boundary conditions are defined from 30 min output of analogously configured 1D model experiments (described in Chapter 3) which include the 'Craig approximation' for the first order surface elevation gradient response. Relaxation times of 1/4 day and 1 day are adopted for inward and outward radiation, respectively, implying strong relaxation to the specified boundary values. A sponge layer of 10 km (20 grid cells) is used to gradually ramp up the internal model solution to the applied boundary values within the sponge layer.

The baseline analytical model is configured with a flat bottom defined at 100 m depth, although we test the sensitivity of the model solution to constant water depths of 50 m and 20 m, and also to cross-shore bottom slopes of 1:200 and 1:500. The nearshore bathymetry (shallower than 100 m) for the realistically configured simulation is interpolated from digital versions of the most detailed available navigation charts for the region, as provided by the Hydrographer of the South African Navy (Figure 4.1 and Section 2.4). All experiments maintain a constant alongshore bathymetry, and a maximum offshore water depth of 100 m. Baseline experiments adopt a latitude of 30°S for testing the pure case of diurnal-inertial resonance, however we also test the model sensitivity to latitudes of 20°S and 40°S. The realistically configured solution adopts the realistic mooring latitude of $\sim$32.3°S.

Simulations are initialised from rest using a constant salinity of 35 and a temperature profile defined either analytically or from observations. In the case of analytically configured experiments, the initial vertical profile for temperature is defined in the same way as described for the 1D model (Equation 3.9 and Figure 3.2).

The realistic model configuration is initialised using measured temperature profiles from the three moorings of Lucas et al. (2014). Linear interpolation is used to define the initial temperature in between the offshore and inshore moorings, while data from the offshore (inshore) mooring is used to extrapolate offshore (inshore) of the moorings. While it is acknowledged that the temperature section will not be realistic at the offshore extent of the model, the intention is only to provide a stable offshore boundary so that the nearshore processes in the vicinity of the observations can be assessed. The resulting initial temperature section is shown in Figure 4.1.

In the case of analytically configured experiments the land-sea breeze is approximated as a diurnal anticyclonic (anticlockwise in the southern hemisphere) rotating wind stress (τ^{ac}), which is applied as a spatially constant forcing. The amplitude of the applied wind stress is 0.03 N m^{-2}, being typical of the amplitude of the diurnal anticlockwise rotary component of the wind stress (τ^{ac0}) over St Helena Bay (Figure 3.14). Upwelling in these experiments is simulated through the application of a constant alongshore wind stress ($\overline{\tau}_s^y$). We use $\overline{\tau}_s^y$ = 0.05 N m^{-2} in these experiments, being typical of the 7 day mean alongshore wind stress over St Helena Bay (Figure 3.14).

Surface heat fluxes are excluded in analytically configured experiments. In the case of the realistically configured simulation, spatially varying surface stress and heat flux forcing are computed from the CSAG WRF model output, as described in Section 2.4.

4.2.3 Diagnostics

As we aim to compare the results of the 1D and 2D simulations, we remain consistent in the computation of diapycnal mixing diagnostics as described in Section 3.2.5. Note however that in this chapter we do not revisit the bulk shear production theory of Burchard and Rippeth (2009), as the 1D momentum equations from which the theory is derived are no longer valid in the context of our 2D simulations.

As described in Section 3.2.5, we use a defined isotherm as a proxy for the depth of the thermocline (H_s). The 11° C isotherm is used for this purpose in the analytically configured experiments, while the 12.5° C isotherm is used in the realistically configured experiment (consistent with Chapter 2). The quantification of diapycnal mixing is again aided by initialising the model with a passive tracer (C) below the thermocline, representing a reservoir of subsurface nutrients. The initial vertical profile for the passive tracer is defined in the same way as described for the 1D model (Figure 3.2). The cumulative diapycnal mixing of the passive tracer to the surface layer (C_s) is computed according to Equation 3.13. As described in Section 3.2.5, the depth averaged velocity vector over the surface layer of the model (i.e. from the surface to H_s) is used to indicate the surface layer current response in the model ($\overrightarrow{u_s} = (u_s, v_s)$). The analysis of diapycnal mixing is further aided by extracting the vertical turbulent diffusivity (K_{Tv}), as output from the k-ε turbulent closure scheme of the model. K_{Tv} is extracted at the thermocline depth as an indication of interfacial mixing in the model.

In Section 4.3.2 we make use of CROCO's online Lagrangian floats module to track the evolution of subsurface water in upwelling simulations which both include and exclude land-sea breeze forcing. These simulations are initialised with neutrally buoyant Lagrangian floats from the depth of the 11° C isotherm to the bottom in vertical increments of 1 m and over the cross-shore extent of the model domain in increments of 500 m (the horizontal grid resolution), thereby covering subsurface waters over the entire model domain. The floats are advected by the cross-shore and vertical velocity components alone, and no diffusion is added to the movement of the floats. The parcels are hence assumed to be adiabatic and retain the temperature of the source. The location and temperature of each float (interpolated from the Eulerian model grid) is saved at 30 min intervals over each simulation.

We further use the vertical displacement of the thermocline in order to diagnose internal wave generation and propagation in the model. To this end, the thermocline depth is presented as the displacement from the daily running average thermocline depth, allowing us to isolate the super-diurnal variability in the thermocline depth induced by the applied land-sea breeze forcing.

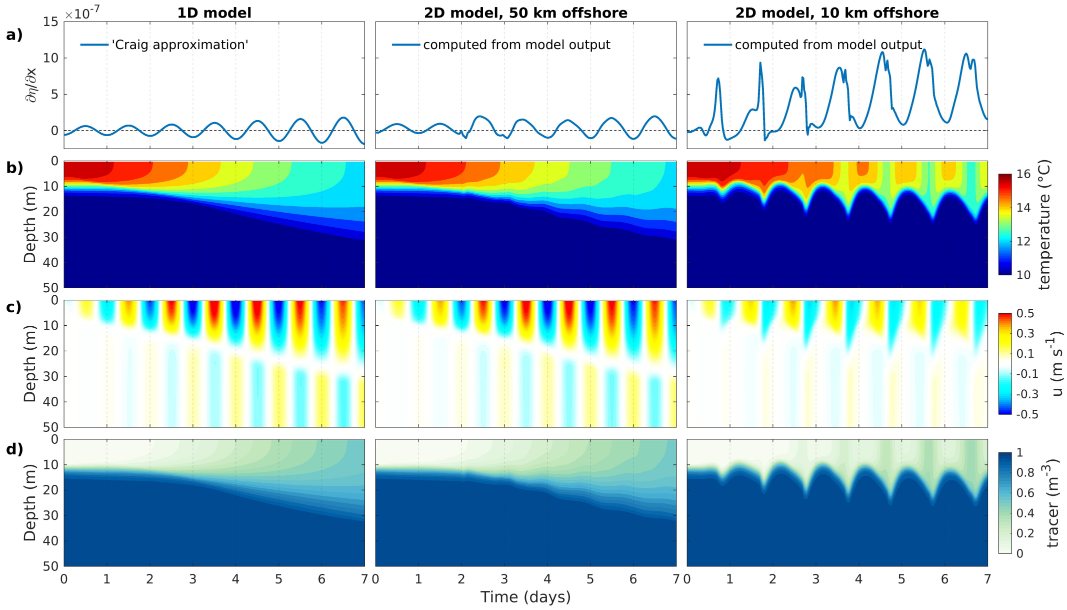

FIGURE 4.2: Flat bottom case, water depth = 100 m. Comparison of the 1D model and the 2D model at distances of 50 km and 10 km from the land boundary. (a) Time-series of surface elevation gradient ($\frac{\partial \eta}{\partial x}$), represented by the 'Craig approximation' in the case of the 1D model, and computed from the model output in the case of the 2D model; (b) Vertical profile of temperature; (c) Vertical profile of cross-shore velocity (u); (d) Vertical profile of passive tracer concentration. Results are computed from a 7 day integration of the models with input parameters τ^{ac0} = 0.03 N m^{-2}, latitude = 30° S, initial MLD =10 m, initial stratification (ΔT) = 6° C.

4.3 Results

4.3.1 Diurnal-inertial resonance at a land boundary

Flat bottom experiments

We begin by considering a flat bottom with a water depth of 100 m, an analytically derived two layer vertical water column structure, and a constant amplitude diurnal anticlockwise rotating wind stress at 30° S (the pure case of diurnal-inertial resonance). The amplitude of the applied wind stress is 0.03 N m^{-2}, and we exclude any sub-inertial upwelling from a mean alongshore wind stress. Figure 4.2 presents the evolution of the model output for both the analogous 1D model configuration presented in Chapter 3 and the 2D model introduced in this chapter at distances of 50 km and 10 km from the land boundary. Figure 4.3 presents Hovmöller diagrams for the 2D experiment showing cross-shore variability in thermocline displacements, $\log_{10} K_{Tv}$ at the 11°C isotherm (taken to represent the thermocline), and the passive tracer concentration integrated from the 11°C isotherm to the surface (C_s).

The results indicate that at a distance of 50 km offshore, the 1D and 2D models are in excellent agreement. In the case of the 1D model, the surface elevation gradient ($\frac{\partial \eta}{\partial x}$) is an applied forcing determined from the 'Craig approximation' for the barotropic response imposed by the no-flow condition perpendicular to the land boundary. The excellent agreement between the 'Craig approximation' and $\frac{\partial \eta}{\partial x}$ computed from the 2D model output suggests that the linear dynamics of the approximation provide a sufficient description of the processes at this location. The agreement between the 1D and 2D model solutions here provides validation for the methodology of using the 1D model solution as the offshore boundary condition for the 2D model. It is noted that this approach largely prevented spurious internal wave generation at the open boundary.

At a distance of 10 km offshore, the 2D model solution deviates significantly from the 1D solution, as the linear assumptions of the 'Craig approximation' are invalid. Here, in close proximity to the land boundary, horizontal gradients in cross-shore currents are high and the non-linear advection terms become important. Onshore (offshore) surface currents lead to convergence (divergence) of the surface currents and the downward (upward) displacement of the thermocline. Thermocline displacements have a diurnal periodicity, consistent with the diurnal periodicity of the wind forcing. The cross-shore currents are significantly weaker at 10 km offshore than at 50 km offshore, implying reduced vertical shear and therefore reduced diapycnal mixing, as reflected in the surface tracer concentration. Unlike at 50 km offshore, the results at 10 km offshore reveal strong diurnal variability in surface temperature and tracer concentration, reflecting high spatial variability in diapycnal mixing which is advected back and forth over the shown output location by the surface inertial oscillations.

Hovmöller diagrams of the 2D experiment (Figure 4.3) reveal that the vertical displacements of the thermocline generate an offshore propagating, but evanescent internal wave response, which is largely dissipated by 50 km from the land boundary. Between 10 km and 50 km offshore, diapycnal mixing is shown to respond to a combination of the forced response and the internal wave response, generating diurnal

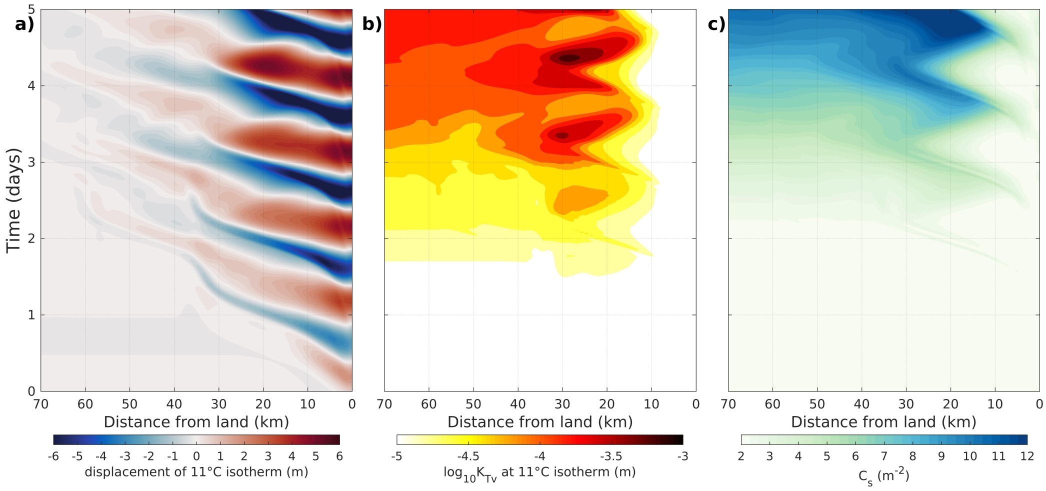

FIGURE 4.3: Hovmöller diagrams for the 2D experiment shown in Figure 4.2. (a) Displacement of the 11°C isotherm from the daily running average isotherm depth, where blue (red) denotes downward (upward) displacement of the thermocline; (b) $\log_{10} K_{Tv}$ at the 11°C isotherm; (c) Passive tracer concentration integrated from the 11°C isotherm to the surface (C_s).

peaks of enhanced mixing at the diagnostic thermocline (Figure 4.3b). The net result is elevated diapycnal mixing over and above that induced by the forced response alone, as revealed by a locally enhanced passive tracer concentration in the surface layer of the model (Figure 4.3c).

Figure 4.4 presents the cross-shore variability in the 2D model output for the simulation presented in Figures 4.2 and 4.3 (latitude = 30°S), in contrast to simulations run at latitudes of 20°S and 40°S. The results are presented as Hovmöller diagrams of thermocline displacements, as well as the amplitude of the surface layer velocity ($|\overrightarrow{u_s}|$) and the passive tracer integrated over the surface layer (C_s), both averaged over the fifth day of each simulation. The 1D model output for $|\overrightarrow{u_s}|$ and C_s is also shown for comparative purposes, providing an indicator of the locally forced response ($|\overrightarrow{u_s}|$ and C_s are the same metrics used to summarise the 1D model sensitivity experiments presented in Section 3.3.3). The figure indicates that at 20°S, the diurnal pumping of the thermocline results in offshore propagating internal waves, however these waves are evanescent at latitudes of 30°S and 40°S. This result is consistent with the theoretical dispersion relation for Poincare waves (Equation 1.7), which dictates that waves can only freely propagate at latitudes where the inertial frequency f is less than the frequency of the forced displacements. The forced displacement of

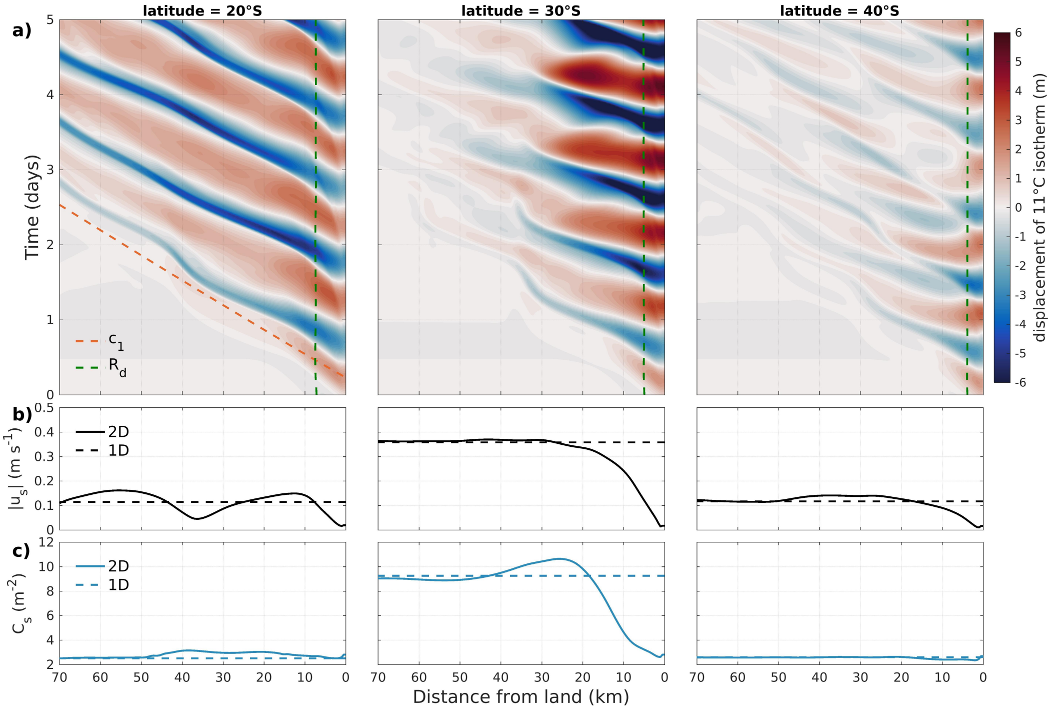

FIGURE 4.4: Flat bottom case, water depth = 100 m. Effect of latitude on cross-shore variability in thermocline displacement, current amplitude and diapycnal mixing. (a) Hovmöller diagram of the displacement of the 11°C isotherm from the daily running average isotherm depth, where blue (red) denotes downward (upward) displacement of the thermocline. The orange and green dotted lines denote the theoretical internal wave speed (c_1) and internal Rossby radius of deformation (R_d), respectively. (b) Amplitude of the surface layer velocity ($|\overrightarrow{u_s}|$), averaged over the fifth day the simulation. The dotted line denotes the 1D solution at the corresponding depth. (c) Passive tracer concentration integrated over the surface layer (C_s), and averaged over the fifth day the simulation. The dotted line denotes the 1D solution at the corresponding depth. Results are computed from a 7 day integration of the models with input parameters τ^{ac0} = 0.03 N m^{-2}, initial MLD =10 m, initial stratification (ΔT) = 6° C.

the thermocline is limited to within the internal Rossby radius of deformation (R_d), while propagation of the displacement occurs offshore of R_d:

$$R_d = \frac{c_1}{f} \tag{4.1}$$

where c_1 is the celerity of the internal wave. The results indicate that c_1 can be reasonably approximated by the theoretical celerity of a long wave propagating at the interface of a two layer system:

$$c_1 = \sqrt{g' \frac{H_s H_b}{H_s + H_b}} \tag{4.2}$$

where $g' = \frac{\Delta\rho}{\rho} g$ is the reduced gravity acceleration. H_s and H_b are the thicknesses of the surface and bottom layers, respectively, as defined by the depth of the 11°C isotherm. For theoretical experiment shown in Figure 4.4, c_1 is estimated from the temperature difference between the surface and subsurface layers and a linear expansion coefficient $\alpha = 2 \times 10^{-4}$ K^{-1}.

The amplitude of the thermocline displacement is greatest at the critical latitude of 30°S, where the amplitude of the surface currents and therefore convergence/divergence at the land boundary is greatest (Figure 4.4b). At this latitude, the amplitude of the surface current is shown to drop off rapidly within ∼20 km of the land boundary. Diapycnal mixing, as quantified through the passive tracer concentration integrated over the surface layer (C_s), is shown to be highest at a distance of ∼25 km offshore, and is ∼20% greater than the offshore value. As already described, the elevated mixing is attributed to the effect of the evanescent internal waves which contribute to the mixing induced by the forced response. The effect of the internal wave response is shown to extend to ∼50 km offshore, after which the results are in good agreement with the forced response, as estimated by the 1D model solution (Figure 4.2).

Both surface current amplitude and diapycnal mixing are predictably lower at latitudes of 20°S and 40°S when compared to 30°S. For the 20°S experiment the signature of the offshore propagating internal waves is evident both through deviations of the surface current amplitude (Figure 4.4b) and elevated diapycnal mixing (Figure 4.4c)

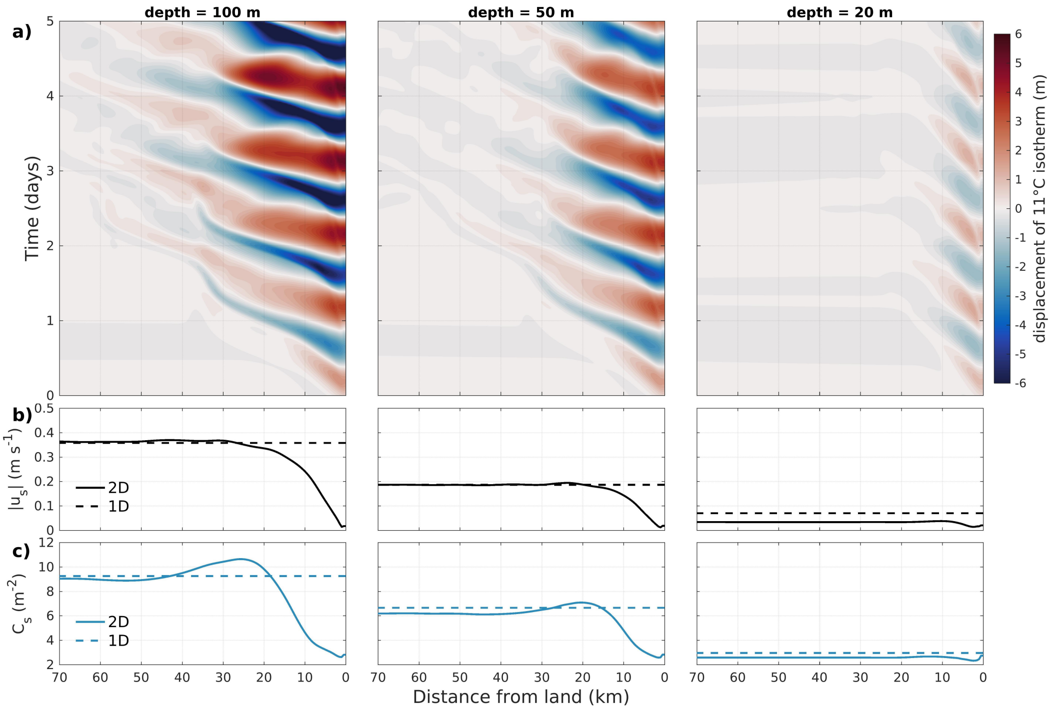

FIGURE 4.5: As per Figure 4.4, but testing the effect of water depth at a latitude of 30°S. The left panels are identical to the centre panels in Figure 4.4.

when compared to the forced response. This is not seen in the 40°S experiment, where the effect of the internal wave response is negligible.

Continuing with flat bottom experiments, Figure 4.5 presents the sensitivity of the model to water depth. In Chapter 3 we showed that bottom friction losses associated with smaller water depths have a dampening effect on the forced response to diurnal-inertial resonance. We observe here that dampened surface oscillations lead to lower convergence/ divergence at the land boundary and a consequent reduction in the internal wave response. The effect of the internal waves on the surface current amplitude and diapycnal mixing is in turn commensurately reduced.

Effect of bottom slope

In Figure 4.6 we contrast the 100 m water depth flat bottom configuration already presented with two experiments in which the water depth gradually increases away from the land boundary, employing constant bottom slopes of 1:200 and 1:500, respectively. By way of comparison, the average bottom slope across the moorings in

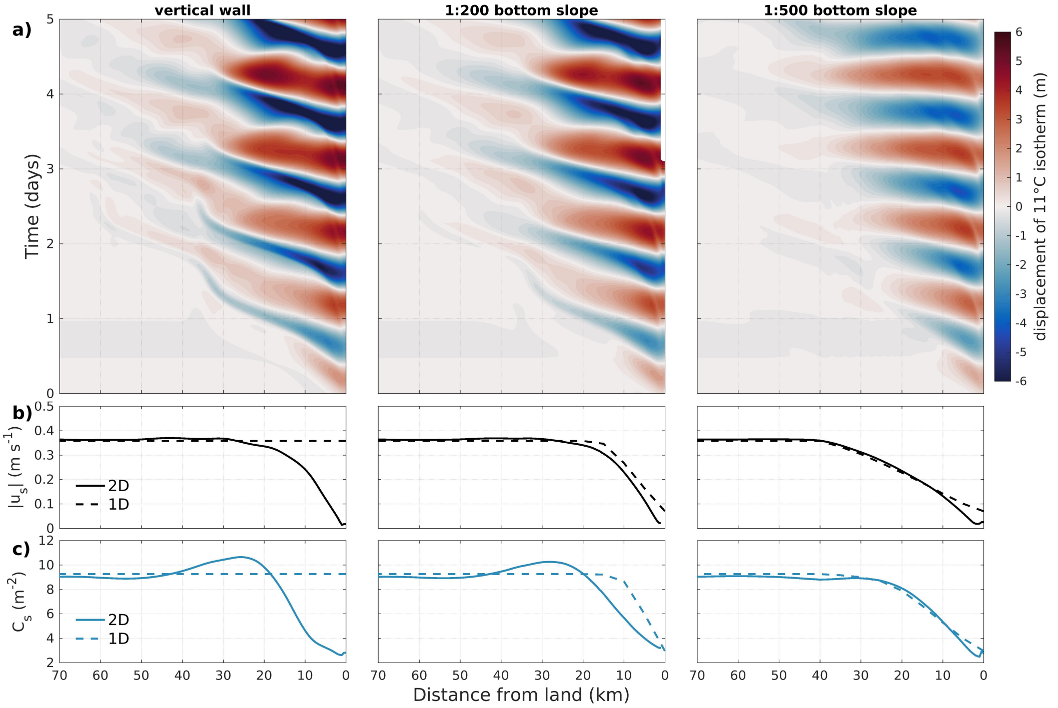

FIGURE 4.6: As per Figure 4.4, but testing the effect of bottom slope at a latitude of 30°S. The left panels are identical to the centre panels in Figure 4.4.

St Helena Bay is approximately 1:200 (Figure 4.1). The 1D model has been run at various water depths to better evaluate the role of the bottom slope on the cross-shore variability in the forced response. The results of the 1D model (dashed lines in Figure 4.6b,c) are taken from individual model solutions run at 5 km increments from the land boundary, using the corresponding water depth of the 2D model. The 1D model experiments show how the forced response becomes gradually dampened toward the land boundary, and that the degree of dampening is greater for more gradual bottom slopes. The dampening of the forced response leads to a reduction in the convergence/ divergence of the forced oscillations in the surface layer, and therefore a reduction in thermocline pumping (Figure 4.6a). Considering the case of the 1:500 bottom slope, the 2D model results for both $|\overrightarrow{u_s}|$ and C_s are almost identical to the 1D model (right panels of Figure 4.6b,c), indicating that the internal wave effects on currents and diapycnal mixing are negligible. As the slope becomes steeper, so the convergence/ divergence in the forced response becomes greater and the effects of the internal waves, as already described, become apparent. Steeper bottom slopes are therefore shown to enhance the internal wave response and allow for elevated diapycnal mixing over and above what would be expected from the forced response alone.

4.3.2 Diurnal-inertial resonance in the presence of upwelling

In the case of upwelling systems, the processes associated with diurnal-inertial resonance are embedded within Ekman dynamics driven by sub-inertial wind variability. The 2D model allows us to explore the interaction of the inertial response to the land-sea breeze and sub-inertial upwelling by comparing simulations forced with a diurnal anticlockwise rotating wind stress alone (τ^{ac0} = 0.03 N m^{-2}), a mean alongshore wind stress alone ($\overline{\tau}_s^y$ = 0.05 N m^{-2}), and a combination of the two. The values of τ^{ac0} and $\overline{\tau}_s^y$ were specifically chosen so that a combination of the two is representative of a 'typical' upwelling event within St Helena Bay (Figure 3.14). For simulations including sub-inertial upwelling, $\overline{\tau}_s^y$ is linearly ramped up from zero to the specified value over the second day of the simulation. This allows for the preconditioning of the water column by the land-sea breeze over the first two days before the full impact of the mean alongshore wind stress is felt by the surface layer. We adopt a bottom slope of 1:200 for these experiments, being representative of the bottom slope within St Helena Bay (Figure 4.1). Figure 4.7 presents the temporal evolution of the modelled temperature, cross-shore currents and passive tracer for each experiment at a distance of 10 km from the land boundary.

The processes associated with the simulation forced with τ^{ac0} alone have already been described (Figure 4.2), whereby diurnal variability in surface temperature is driven by a combination of high spatial variability in diapycnal mixing and advection due to the surface inertial oscillation. The simulation forced with $\overline{\tau}_s^y$ alone shows considerably reduced diapycnal mixing, and shows the offshore transport of the surface layer in response to the sustained alongshore wind stress (centre panel of Figure 4.7b). The combined effect of sub-inertial upwelling and inertial oscillations is to generate pronounced diurnal variability in surface temperature, coinciding with the sub-inertial advection of the upwelling front past the model output location. The inertial oscillations (left panels of Figure 4.7) are superimposed onto the sub-inertial transport (centre panels of Figure 4.7), resulting in the repeated advection of the upwelling front past the model output location (right panels of Figure 4.7), explaining

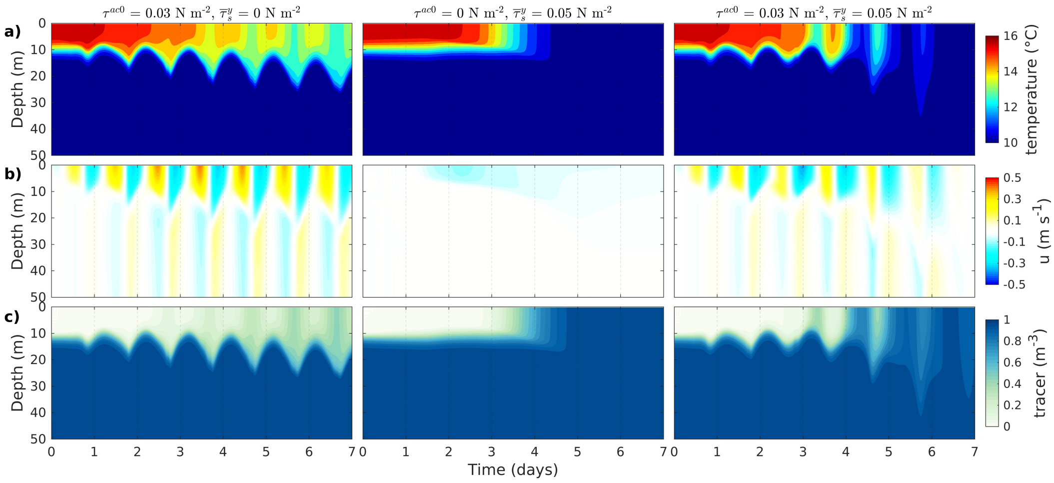

FIGURE 4.7: Effect of the land-sea breeze over a 'typical' upwelling event at a distance of 10 km from the land boundary. Simulations are forced with τ^{ac0} = 0.03 N m^{-2} alone (left), $\overline{\tau}_s^y$ = 0.05 N m^{-2} alone (middle), and a combination of the two (right). (a) Vertical profile of temperature; (b) Vertical profile of cross-shore velocity (u); (c) Vertical profile of passive tracer concentration. Results are computed from a 7 day integration of the models with input parameters latitude = 30° S, bottom slope = 1:200, initial MLD =10 m, initial stratification (ΔT) = 6° C.

the enhanced diurnal variability in temperature.

The cross-shore variability in temperature, and associated offshore distance of the upwelling front, provides further insight into the impact of the land-sea breeze on sub-inertial upwelling dynamics (Figure 4.8). For this analysis the offshore distance of the upwelling front is approximated as the surface outcropping of the 11°C isotherm (Figure 4.8d). The effect of the land-sea breeze on upwelling is distilled by comparing the simulation forced by a combination of τ^{ac0} and $\overline{\tau}_s^y$ (Figure 4.8a) with the simulation forced by $\overline{\tau}_s^y$ alone (Figure 4.8b). The two shown snapshots in time (left and centre panels of Figure 4.8a-c) have been specifically selected to display the landward and seaward extent of a particular inertial oscillation (as shown by the vertical dotted lines in Figure 4.8d).

At the offshore extent of the shown section (i.e. outside the influence of the upwelling front), the inertial response is shown to result in a significant cooling of the surface, which overlays a commensurate warming. This result is consistent with the effects of a deepened thermocline through local diapycnal mixing. The snapshot in time depicting the landward extent of the surface oscillation predictably shows the

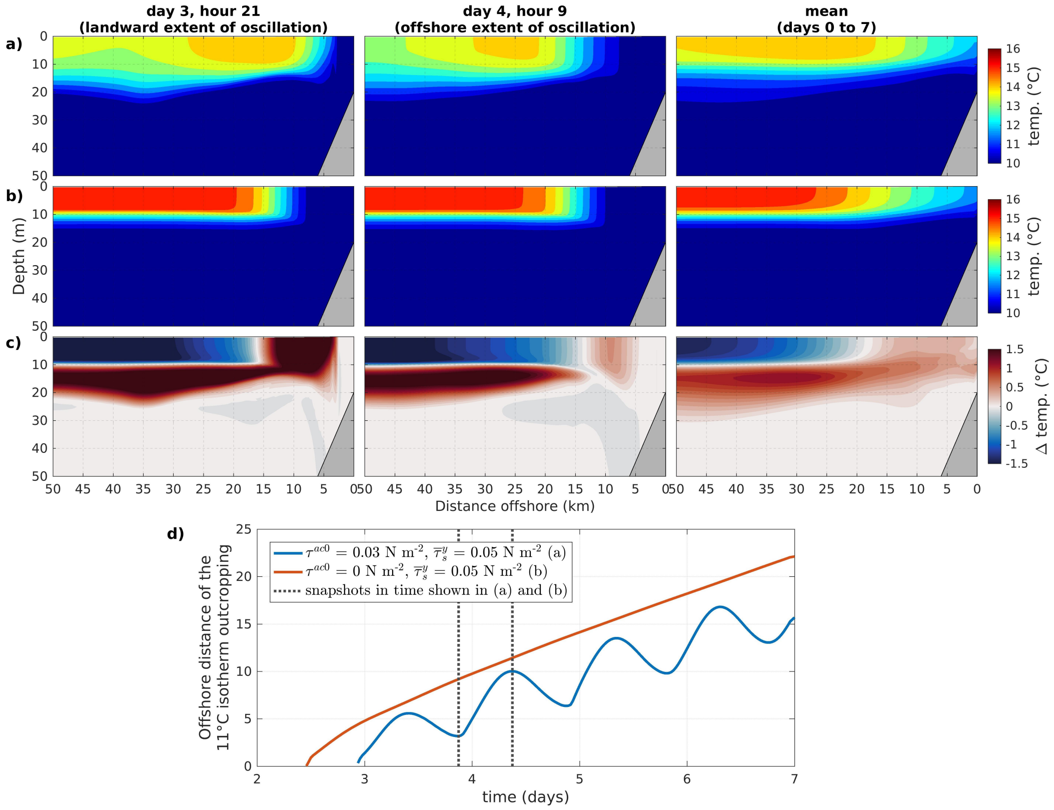

FIGURE 4.8: Effect of the land-sea breeze on the cross-shore variability in temperature over a 'typical' upwelling event. (a) Snapshots in time and mean section of temperature for the simulation forced with a combination of τ^{ac0} = 0.03 N m^{-2} and $\overline{\tau}_s^y$ = 0.05 N m^{-2}; (b) Snapshots in time and mean section of temperature for the simulation forced with $\overline{\tau}_s^y$ = 0.05 N m^{-2} alone (i.e. excluding the land-sea breeze); (c) Difference between (a) and (b) (c=a-b); (d) Time-series of the offshore distance of the 11°C isotherm in the surface layer of the model (used as a proxy for the upwelling front) for the simulations shown in (a) and (b). Results are computed from a 7 day integration of the models with input parameters latitude = 30° S, bottom slope = 1:200, initial MLD =10 m, initial stratification (ΔT) = 6° C.

upwelling front to be located landward of that predicted by the simulation forced with $\overline{\tau}_s^y$ alone, leading to a positive surface temperature difference in the vicinity of the upwelling front (Figure 4.8a-c, left panels).

One might expect a symmetrically negative surface temperature difference when the surface inertial oscillation is at its seaward extent, however this is not the case (Figure 4.8a-c, middle panels). Figure 4.8d confirms that the location of the upwelling front (as depicted by the outcropping of the 11°C isotherm) for the simulation forced by a combination of τ^{ac0} and $\overline{\tau}_s^y$ is consistently landward of that for the simulation forced by $\overline{\tau}_s^y$ alone. This implies that the inclusion of the land-sea breeze in the upwelling event leads to a reduction in the offshore advection of the surface layer. While the net offshore transport of the surface layer will be identical in the two simulations, in accordance with classical Ekman theory (Equation 1.2), the transport is applied over a deeper surface layer when the land-sea breeze is included, explaining the reduction in net offshore advection.

The comparison of the mean temperature section computed over the entire 7 day upwelling event (Figure 4.8a-c, right panels) reveals a net warming of nearshore surface waters (i.e. within the region under the influence of the upwelling front) as a consequence of the land-sea breeze. We posit two explanations for this result. Firstly, the persistent landward location of the upwelling front due to the inclusion of the land-sea breeze (Figure 4.8d) will naturally result in warmer nearshore surface waters. Secondly, the vertical mixing induced by the land-sea breeze leads to a warming of subsurface waters, which are carried by the upwelling circulation toward the inshore and surface. In Figure 4.9 we present diagnostics designed to estimate the relative contribution of these two processes to nearshore surface warming.

The contribution of the location of the upwelling front (blue line in Figure 4.9) is computed as follows: the cross-shore temperature profile from the surface layer of the $\overline{\tau}_s^y$ forced simulation is extracted at each 30 min time-step; a landward offset to this profile is then applied according to the difference in the upwelling front locations shown in Figure 4.8d; the difference between the original and the offset cross-shore temperature profiles is then computed. The effect shown in Figure 4.9 is the mean temperature difference over the entire 7 day simulation.

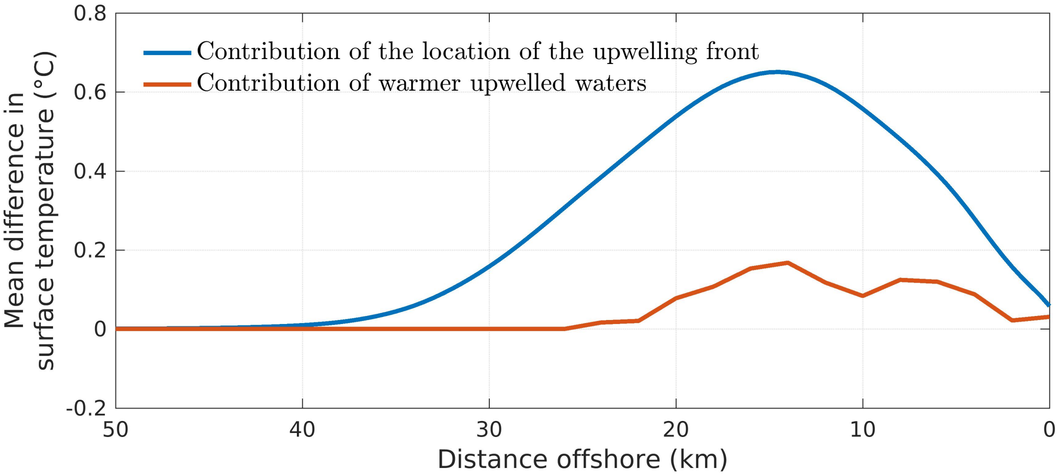

FIGURE 4.9: Diagnostics explaining the warming of nearshore surface waters in response to the inclusion of the land-sea breeze, as shown in Figure 4.8a-c, right panels.

The contribution of the upwelling of warmer subsurface waters (red line in Figure 4.9) is computed via an analysis of Lagrangian floats initialised from the depth of the 11° C isotherm to the bottom (see Section 4.2.3), allowing us to track the temperature of 'upwelled' water in both simulations as follows: all Lagrangian floats in the upper 5 m of the water column are identified at each 30 min time-step and taken to represent 'upwelled' water; the difference between the temperature of the Eulerian field at the location of the floats and the original temperature of the floats is computed; the offshore distance of the floats are used to construct a cross-shore profile of the surface temperature difference, using 2 m bins in the cross-shore direction and averaging the temperature difference from all 'upwelled' Lagrangian floats contained within each 2 m bin. The effect shown in Figure 4.9 is the mean temperature difference over the entire 7 day simulation forced by a combination of τ^{ac0} and $\overline{\tau}_s^y$, over and above that computed from the simulation forced by $\overline{\tau}_s^y$ alone.

The analysis suggests that the nearshore warming due to the inclusion of the land-sea breeze is primarily driven by the location of the upwelling front, while the upwelling of warmer waters due to enhanced vertical mixing plays a secondary role. This is not particularly surprising, as subsurface warming is most pronounced immediately below the thermocline where the onshore upwelling circulation is not particularly intense while, conversely, subsurface warming is weak at deeper depths where the onshore flow is stronger. It is noted that the combined nearshore surface warming of the diagnostics shown in Figure 4.9 is larger than the overall nearshore surface warming shown in Figure 4.8a-c, right panels, however this is explained by the fact that these diagnostics intentionally exclude the surface cooling effect of vertical mixing.

4.3.3 Case study of St Helena Bay

We now present the final more comprehensive experiment, being a realistically configured simulation for comparison with the nearshore observations of Lucas et al. (2014). This allows us to assess the extent to which the dynamics elucidated by the analytically configured experiments can be used to explain the observations. The model solution is integrated over a 7 day period, starting on 7 March 2011 from the temperature section shown in Figure 4.1, and forced with hourly winds and heat fluxes derived from the CSAG WRF simulation. It is again highlighted that this event was specifically identified as a period where the observations clearly demonstrate the response of a highly stratified two layer system to the onset of upwelling favourable winds with an anticlockwise sense of rotation (Lucas et al., 2014).

Figure 4.10 presents the evolution of observed and modelled temperature throughout the water column across the mooring array, including summary statistics as a function of depth (refer to Equations 2.21 and 2.22). The model is shown to reproduce the salient features of the temperature observations at all three moorings, which show significant diurnal variability in surface temperature (particularly over 9 - 12 March 2011) and a net cooling of surface waters over the considered period. The 2D analytical experiments have highlighted that strong diurnal variability in surface temperature can be expected during an upwelling event accompanied by a land-sea breeze near the critical latitude (Figure 4.7), explained by strong horizontal surface temperature gradients in the presence of the inertial oscillations. The horizontal gradients are set up by a combination of sub-inertial upwelling as well as spatial variability in diapycnal mixing induced by the land-sea breeze. The net cooling of surface waters, over and above that explained by diapycnal mixing, is explained

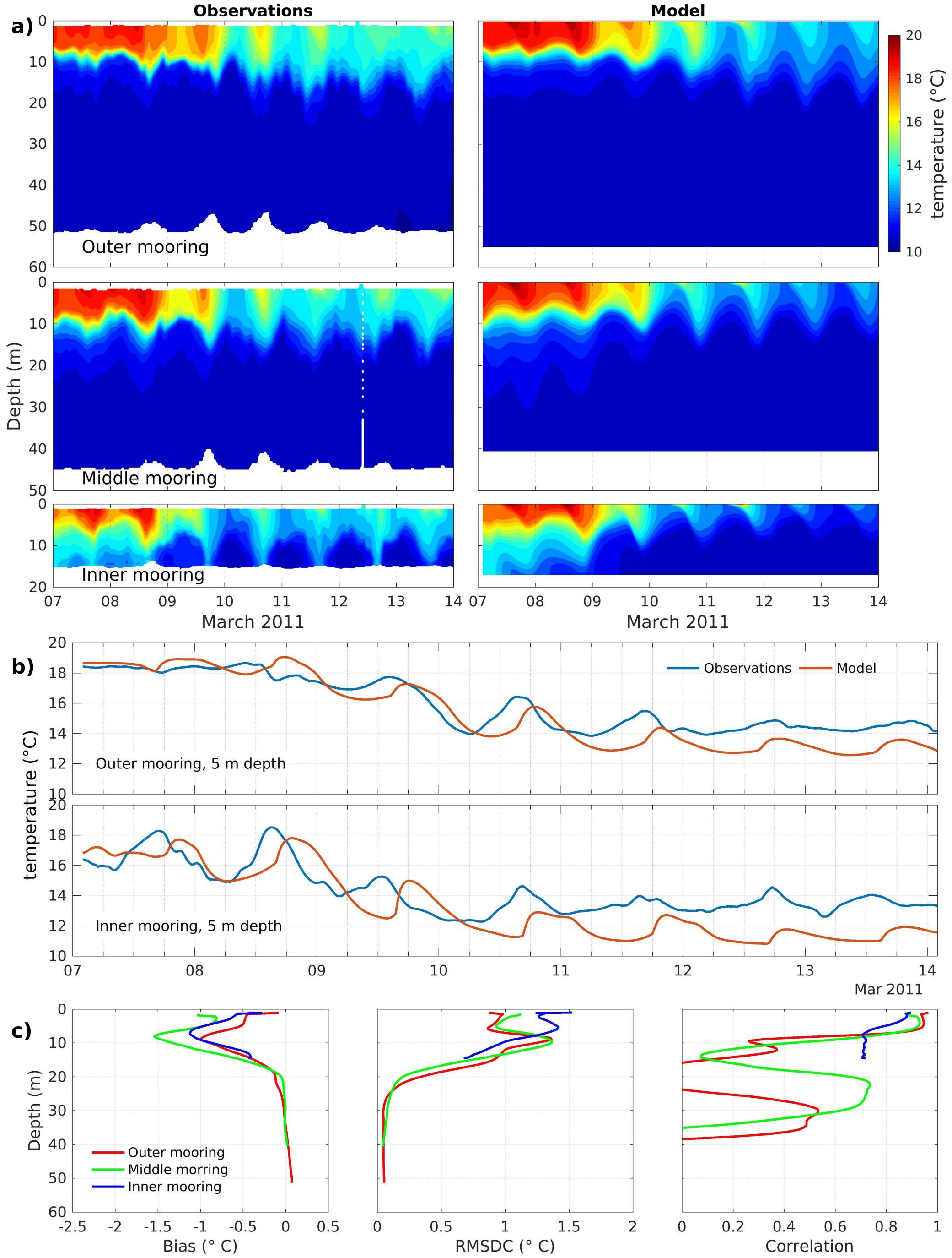

FIGURE 4.10: Observed and modelled temperature over an upwelling event accompanied by diapycnal mixing from three moorings in St Helena Bay ('WW' Figure 4.1). (a) Temporal evolution of the observed (left) and modelled (right) temperature profile at the outer (~12.7 km offshore), middle (~8.1 km offshore) and inner (~3.9 km offshore) moorings. (b) Time-series of observed and modelled temperature at the outer and inner moorings at 5 m depth. (c) Summary statistics for modelled temperature as a function of depth.

by offshore Ekman transport of the surface layer driven by the sub-inertial alongshore winds (Figure 4.7). The good agreement between the model and the observations is reflected in high temperature correlations at the surface (>0.8 for depths shallower than ∼5 m, as shown in Figure 4.10c). The time-series comparisons at 5 m depth (Figure 4.10b) confirm that while the features of the temperature signal are reasonably reproduced in the model, there is a notable lag in the modelled temperature. This may indicate shortcomings in the phase of the high-frequency component in the winds used to force the model. The significant reduction in temperature correlations near the base of the thermocline could be explained by what appears to be an over-prediction in sub-inertial upwelling and the consequent over-prediction in thermocline lifting, reflected in a negative near-surface temperature bias across the moorings (left panel of Figure 4.10c). The low (even negative) correlations in the subsurface at the middle and outer moorings are attributed to the lack of a meaningful temperature signal over the considered event, as evidenced by the low RMSDC in this region of the water column, despite poor correlations.

Figure 4.11 presents the evolution of the cross-shore component of velocity for the outer and inner moorings only (ADCP data from the middle mooring was mostly missing over this period and is therefore not shown). The comparison confirms that the model is able to reproduce the salient features of the vertical current structure of the observations. The time-series comparisons (Figure 4.11b) however again reveal a notable time lag in the modelled currents at both the outer and inner moorings, which lag the observations by ∼6 hrs. Despite the presence of the time lag, correlation coefficients at the outer mooring are between ∼0.4 and ∼0.6 for the subsurface currents, while a maximum of ∼0.7 is attained for the modelled near-surface currents (Figure 4.11c). These model correlation coefficients drop to negative values in the region of the thermocline, where the 180° phase shift between the surface and subsurface currents is observed. Poor correlation in this region is not surprising, as any misrepresentation in the depth of the 180° phase shift will have a notable impact on the horizontal current correlations in this region of the water column. Current correlations are lower at the inner mooring (between ∼0.2 and ∼0.4), where the amplitude of the inertial oscillations is weaker. The modelled currents at this mooring

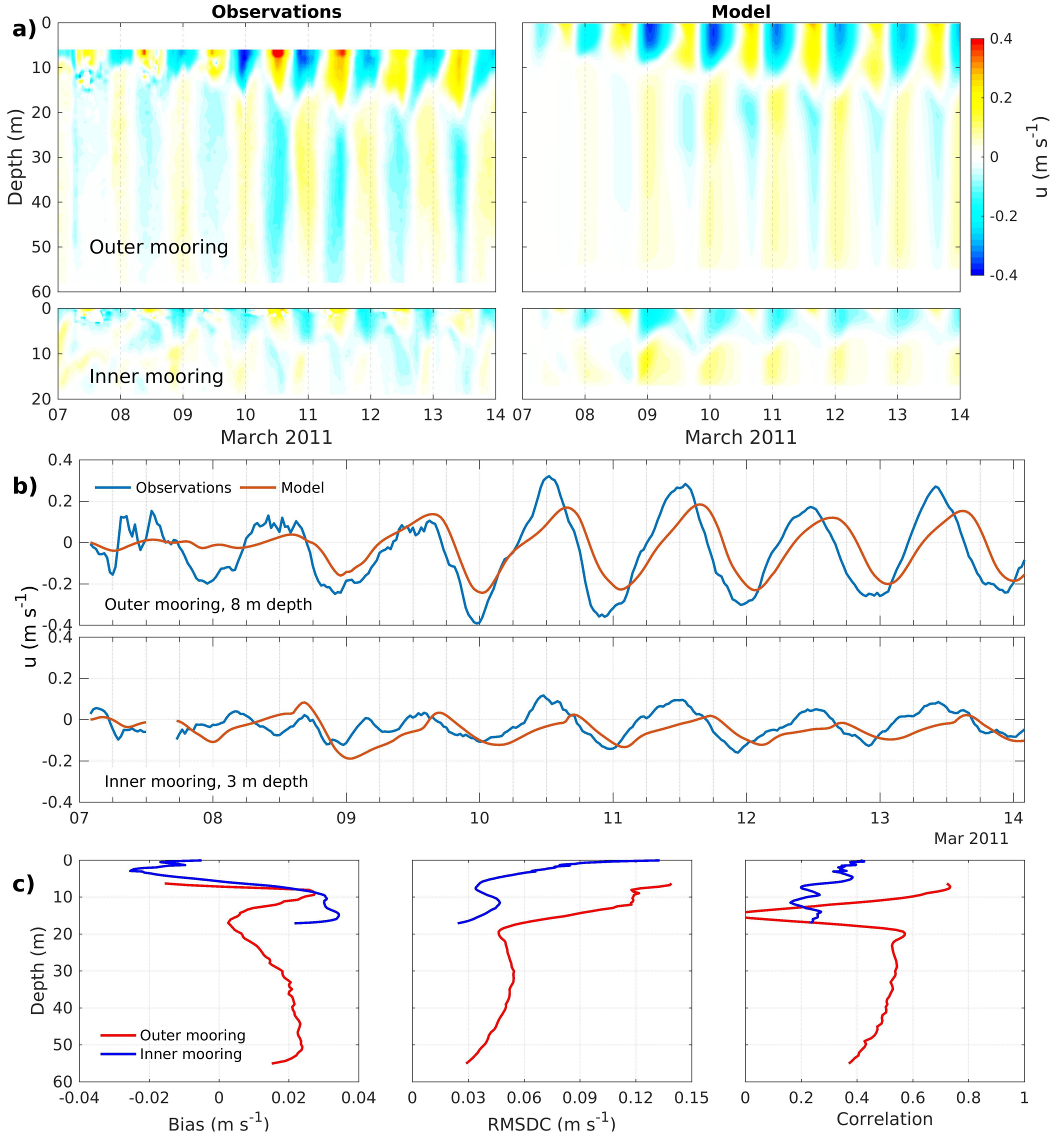

FIGURE 4.11: Observed and modelled cross-shore velocity (u) over an upwelling event accompanied by diapycnal mixing from two moorings in St Helena Bay ('WW' Figure 4.1). (a) Temporal evolution of the observed (left) and modelled (right) cross-shore velocity profile at the outer (∼12.7 km offshore) and inner (∼3.9 km offshore) moorings. (b) Time-series of observed and modelled cross-shore velocity at the outer and inner moorings at 8 m and 3 m depths, respectively. (c) Summary statistics for modelled cross-shore velocity as a function of depth. ADCP data from the middle mooring was mostly missing over this period and is therefore not shown.

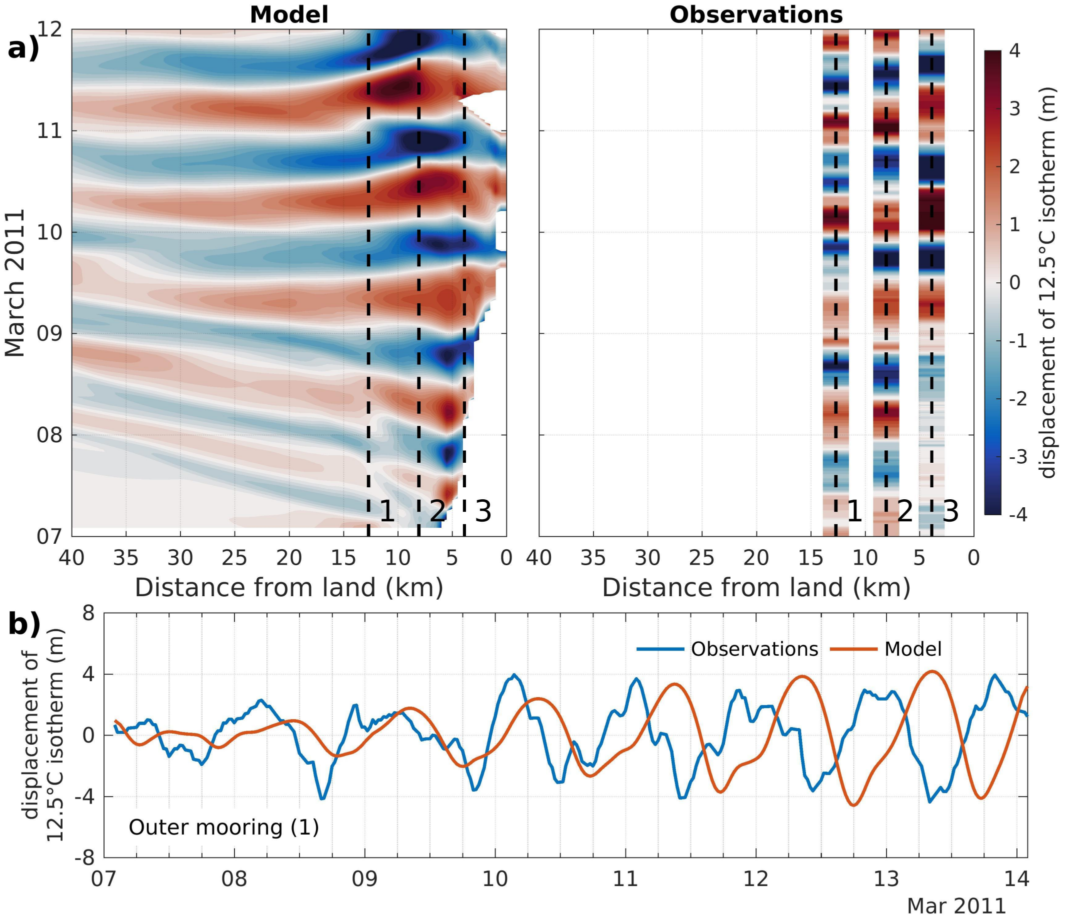

FIGURE 4.12: (a) Observed (left) and modelled (right) Hovmöller diagrams of the displacement of the 12.5°C isotherm from the daily running average isotherm depth, where blue (red) denotes downward (upward) displacement of the thermocline. (b) Time-series of observed and modelled thermocline displacement at the outer mooring (~12.7 km offshore).

appear to be hampered by the signature of an over-prediction in sub-inertial upwelling circulation, as evidenced by negative (positive) cross-shore current biases in the surface (subsurface) (Figure 4.11c). This shortcoming is in agreement with the over-prediction in surface temperature cooling visible in Figure 4.10.

Both the model and the observations indicate a notable reduction in surface oscillation amplitude toward the land boundary. As the outer mooring is ~12.7 km offshore, the observations are all located within the region where the analytically configured experiments anticipate a rapid drop-off in the amplitude of the surface oscillation towards the land boundary (centre panel of Figure 4.6b). The strong convergence and divergence of surface oscillations in this region is shown to drive vertical displacements of the thermocline near the diurnal-inertial frequency, visible in both the model and the observations (Figure 4.12). Note that the missing data in the model output shown in Figure 4.12a corresponds to the outcropping of the 12.5°C isotherm, used to denote the thermocline. The time-series comparison shown in Figure 4.12b indicates that while the amplitude of the thermocline displacements is reasonably reproduced in the model, the previously noted phase lag is again evident. Interestingly, unlike the phase lag observed in the modelled currents, the phase lag in the thermocline displacements increases over the simulation, until the modelled thermocline displacements are almost completely out of phase by the end of the simulation. As previously noted, this discrepancy is likely an indication of shortcomings in the high-frequency component in the winds used to force the model.

4.4 Discussion and conclusions

In this chapter we have used a 2D-vertical model to gain insight into the cross-shore variability in nearshore processes governing the response to land-sea breeze forcing in coastal upwelling systems located near the critical latitude for diurnal-inertial resonance. By contrasting the results from the 2D-vertical model with those of the 1D-vertical model presented in Chapter 3, we have been able to identify the respective roles of the locally forced response (as approximated by the 1D model) and the internal wave response to land-sea breeze forcing near the critical latitude. In addition to testing the sensitivity of the processes to relevant variables, a realistically configured 2D-vertical model has been compared with three nearshore moorings orientated perpendicular to the local coastline in St Helena Bay, southern Benguela (Lucas et al., 2014). Notwithstanding model shortcomings which include an overprediction in sub-inertial upwelling and a phase lag in the modelled diurnal-inertial response, the favourable comparison with the observations provides some confidence in the dynamics elucidated by the analytically configured experiments. Key findings are summarised and discussed below.

4.4.1 Nearshore response of upwelling systems to the land-sea breeze

In agreement with the numerical experiments of Zhang et al. (2010), our sensitivity tests to latitudinal dependence indicate that the internal wave response to the land-sea breeze is trapped poleward of 30° N/S, where there is no solution to the dispersion relation for Poincare waves. As the forced inertial response to the land-sea breeze is maximised at the critical latitude (Craig, 1989; Simpson et al., 2002, Chapter 3), here we also find the maximum amplitude thermocline displacements due to convergence/ divergence of the forced oscillations at the land boundary. The internal Rossby radius of deformation (R_d) provides a reasonable offshore limit for the forced thermocline displacements, which generate offshore propagating internal waves. At the critical latitude, the waves are evanescent and largely absent offshore of $\sim$50 km from the land boundary. The excellent agreement between the 2D and 1D model solutions offshore of $\sim$50 km from the land boundary provides further confidence in the application of the 'Craig approximation' for the barotropic response to the no-flow condition perpendicular to the land boundary. Within $\sim$50 km from the land boundary, the amplitude of the inertial oscillations and associated shear-driven diapycnal mixing are driven by a combination of the forced and evanescent internal wave response. At the critical latitude, the model estimates that diapycnal mixing is maximised at a distance of $\sim$25 km from the land boundary, where mixing can be up to $\sim$20% greater than that predicted by the forced response alone. The contribution of the internal wave response to diapycnal mixing is however moderated by the bottom slope, whereby shallower slopes lead to a dampened internal wave response due to reduced nearshore convergence/ divergence of the forced response at the land boundary.

Within the context of upwelling systems, the evanescent internal wave response represents a significant contribution to local diapycnal nutrient flux near the critical latitude, with implications for nearshore phytoplankton growth. The large thermocline displacements associated with the internal wave response may have further implications on productivity due to their influence on light availability over the surface layer. In Chapter 3 we showed that shear-driven mixing is enhanced during night time, which would benefit phytoplankton growth during the following day. However observations reveal that the onshore advection of the surface layer and consequent downward displacement of the thermocline occurs during daylight hours. These super-diurnal physical processes and their timing with respect to sunlight availability are likely to have a significant impact on the event-scale productivity of these systems. It is suggested that coupling of the 2D-vertical model presented here with a biogeochemical model could prove useful in improving our understanding of super-diurnal phytoplankton dynamics in EBUS. Failure to include such small scale and high frequency processes in global and regional biogeochemical models may be a major shortcoming in simulating the productivity of these systems. The significant phase lag in our modelled thermocline displacements should however be noted, as this shortcoming would hamper any model study into these high-frequency phytoplankton dynamics. The use of wind data from nearshore observations to force the model may prove useful in circumventing some of the phasing errors introduced in the model forcing.

The inclusion of a sub-inertial alongshore wind stress in the 2D model experiments has allowed for further reflection on the role of the inertial response within the context of upwelling dynamics. Our results reveal how the combined effect of sub-inertial upwelling and inertial oscillations can produce pronounced diurnal variability in nearshore surface temperatures, driven by horizontal diurnal advection of strong cross-shore temperature gradients which are a feature of upwelling systems. Local land-sea breeze forcing has been identified as playing a key role in diurnal temperature variability in a number of in-situ observations in EBUS (Kaplan et al., 2003; Woodson et al., 2007; Bonicelli et al., 2014; Walter et al., 2017), and is evident in the nearshore observations of Lucas et al. (2014) (Figure 4.10). The 2D model experiments presented here clearly demonstrate a driving mechanism of this phenomenon. It should however be noted that the additional contribution of solar irradiance in driving diurnal variability in sea surface temperatures in EBUS has not been explicitly considered in this chapter. This is however further explored in a realistically configured regional simulation of the southern Benguela in Chapter 5.

Our simulations further highlight how deepening of the thermocline due to diurnal-inertial resonance near the critical latitude can lead to a significant reduction in sub-inertial offshore advection of the surface layer. Retention of surface waters is an important mechanism for the accumulation of high biomass coastal blooms in EBUS (Pitcher et al., 2010). Our results provide evidence that the reduction of advective losses due to land-sea breeze forcing may play a contributing role in the retention of surface waters in EBUS. This effect is expected to be greatest near the critical latitude for diurnal-inertial resonance, as this is where we find a peak in diapycnal mixing and the consequent deepening of the thermocline which is responsible for the reduction in offshore advection.

The mean cross-shore temperature section is shown to be significantly impacted by the land-sea breeze over a 'typical' upwelling event, resulting in cooler sea surface temperatures (SST's) offshore of the upwelling front (in response to diapycnal mixing), and warmer SST's landward of the upwelling front (largely due to reduced sub-inertial offshore advection). Nearshore temperature biases are a common shortcoming in global and regional models of EBUS. Such biases are largely attributed to errors in the representation of the low frequency alongshore wind stress in the atmospheric forcing products (e.g. Richter, 2015; Small et al., 2015), while the influence of the land-sea breeze is over-looked as a potential source of systematic error. Our results suggest that the spatial and temporal representation of the land-sea breeze could play an additional role in alleviating nearshore SST biases in these models, particularly near the critical latitude. The impact of the land-sea breeze on nearshore temperatures of a realistic simulation of the southern Benguela will be explored in Chapter 5.

4.4.2 Improved understanding of St Helena Bay observations

The three moorings revisited in this study are located ∼12.7 km, ∼8.1 km and ∼3.9 km offshore of the local land boundary, respectively, making them within the region where the 2D simulations predict the overall ocean response to be a combination of the forced response and the evanescent internal wave response. This provides some context for the shortcomings of the 1D model when compared to the outer mooring, as detailed in Chapter 3 (Figure 3.10). The 1D model was shown to over-predict the deepening of the thermocline through diapycnal mixing, under-predict net cooling of surface waters over the event, and lack sufficient diurnal variability in temperature and vertical displacement of the thermocline. Figure 4.6 confirms that for a 1:200 bottom slope (the approximate slope across the mooring array) and an offshore distance of just $\sim$12.7 km, an over-prediction in the amplitude of the surface oscillation and consequent deepening of the thermocline is to be expected in the 1D model. The lack of diurnal variability in surface temperature, as well as the underestimation in the net cooling of surface waters, are both explained in the 2D model experiment through the introduction of offshore Ekman transport in response to a sustained alongshore wind stress (Figure 4.10). The modelled diurnal pumping of the thermocline due to convergence/ divergence of the forced surface oscillation is also in good agreement with the observations. Despite the reduced physics of the 2D model, the reasonable agreement with the observations (and much improved over the 1D model) suggests that it provides a useful lens through which to interpret the observations, and reinforces the insights gained into the fundamental physical processes at play, as revealed by the analytically configured experiments.

Although the 2D model confirms shear-induced diapycnal mixing to be a feature over the mooring array, as argued by Lucas et al. (2014), an important consequence of the presented experiments is that the region of maximum diapycnal mixing is in fact expected to be located offshore of the moorings. It therefore seems plausible that the effect of the land-sea breeze on the event-scale phytoplankton response may well have been further enhanced offshore of the moorings. This suggests that our understanding of event-scale phytoplankton dynamics in the region would benefit from high-frequency observations of the water column which extend across the full width of St Helena Bay.

Chapter 5

The influence of the land-sea breeze in the southern Benguela: diurnal variability in SST, event-scale mixing and implications for the mean state

5.1 Introduction

The reduced physics experiments of Chapters 3 and 4 have provided insight into the fundamental processes governing the response of upwelling systems to land-sea breeze forcing near the critical latitude. We now return to the validated 3D model of the southern Benguela presented in Chapter 2 to further explore these processes at larger spatial scales. In Chapter 3 it was suggested that the energetic diurnal-inertial motions observed in St Helena Bay (Fawcett et al., 2008; Lucas et al., 2014) may be explained by a combination of physical characteristics (proximity to the critical latitude, local amplification of τ^{ac0}, and the development of shallow stratified surface layers) which favour the local development of high amplitude forced surface oscillations. Chapter 4 elucidated the dynamics of the internal wave response to land-sea breeze forcing, and highlighted the combined role of the land-sea breeze and the low frequency winds in driving large diurnal variability in coastal temperatures. The effect of the land-sea breeze in reducing sub-inertial offshore Ekman advection of the surface layer was also investigated. The experiments presented in this chapter allow us to further evaluate these processes within the context of a realistically configured regional model of the southern Benguela. The response of the system is evaluated using experiments and diagnostics designed to reveal the processes elucidated in the preceding chapters. This is achieved through a comparison of simulations which both include and exclude land-sea breeze forcing, while maintaining the same sub-inertial wind forcing.

We firstly consider the extent to which the land-sea breeze drives diurnal variability in SST's within the system. We then distill the effect of land-sea breeze forcing on processes associated with event-scale diapycnal mixing, a common theme throughout the preceding chapters. Finally, we present the effects of land-sea breeze forcing on the seasonal mean vertical water column structure and circulation. We consider upwelling and relaxation wind regimes separately for this analysis, as different sub-inertial processes are at play during each.

5.2 Methods

5.2.1 Atmospheric forcing

The model used to carry out the experiments presented in this chapter is described in detail in Chapter 2. Here we present three different experiments, each identified by the type of wind forcing applied to the model (Table 5.1). All the other forcings and boundary conditions listed in Section 2.4 are unchanged in all experiments. The first simulation is forced with realistic hourly wind stresses (τ^{real}) derived from hourly CSAG WRF model 10 m winds and surface heat fluxes. The model is then re-run using forced daily averaged wind stresses (τ^{daily}) as output from the realistically forced simulation. In so doing, the simulation forced with τ^{daily} maintains net Ekman dynamics and diurnal surface heat fluxes, but the impact of the high-frequency component of the wind stress is removed. In the third simulation we force the model with the diurnal anticyclonic rotary component of the wind stress

TABLE 5.1: Summary of wind forcing for experiments presented in this chapter.

Experiment	Description of wind forcing
τ^{real}	Hourly averaged wind stresses derived from the CSAG WRF model winds
τ^{daily}	Daily averaged wind stresses computed from the simulation forced with τ^{real}
$\tau^{daily+ac}$	Hourly averaged wind stresses corresponding to the diurnal anticyclonic rotary component of the CSAG WRF model winds (τ^{ac}), added to the daily averaged wind stresses (τ^{daily})

(τ^{ac}) which is super-imposed onto τ^{daily}, and adopt the nomenclature $\tau^{daily+ac}$ to refer to this simulation. τ^{ac} is computed from consecutive 7 day windows, as described in Section 3.2 and shown in Figure 3.1. The seasonal climatology of τ^{ac} computed in this way is shown in Figure 3.14. In this simulation we aim to distill the influence of the inertial response of the ocean to the land-sea breeze, while excluding additional effects induced by the high frequency component of the winds.

5.2.2 Computation of climatologies

Each of the three types of wind forcing (Table 5.1) are used to integrate the model over the period 01 November 2005 to 31 December 2012 (7 years), spanning the duration over which all forcing data are available. Daily averaged output from these simulations is used to compute seasonal climatologies of temperature and horizontal current velocity, allowing for an assessment of the impact of the land-sea breeze on the mean state of the vertical water column structure and circulation over the area of interest. Three hourly 'snapshots' of temperature generated over the entire simulation period are used to assess day-night sea surface temperature differences in the model. All seasonal analyses are confined to the nominally upwelling months of October - March, when the amplitude of the land-sea breeze is also at its highest (Figure 3.14).

5.2.3 Event-scale diapycnal mixing experiment

The processes driving event-scale diapycnal mixing in response to land-sea breeze forcing near the critical latitude have been a primary area of focus over the preceding chapters. Here, we use the 3D model to further explore these processes by comparing two simulations, each integrated over a 7 day period initialised on 25 January 2007 from the simulation forced with τ^{daily}. This ensures that the influence of the land-sea breeze is absent from the initial condition. The initialisation date was subjectively chosen to be at the end of a relaxation event characterised by a shallow and highly stratified surface layer over St Helena Bay, as well as a clearly defined Columbine Jet, providing a distinct offshore boundary for bay-scale waters. One simulation is forced with τ^{daily}, while the other is forced with $\tau^{daily+ac}$, allowing for the distillation of the effect of τ^{ac} on event-scale diapycnal mixing. As per the reduced physics experiments presented in Chapters 3 and 4, we initialise the subsurface of the model with a passive tracer (C). C is initialised to a value of 1 for temperatures of 12°C and less, 0 for temperatures of 13°C and above, while linear interpolation is applied for temperatures between 12°C and 13°C. This approach is also adopted for specifying the passive tracer at the lateral boundaries of the model. The 12°C isotherm is used as a proxy for the depth of the thermocline (H_s), and is used to quantify the cumulative mixing of the passive tracer to the surface layer (C_s), in accordance with Equation 3.13. We use C_s averaged over the fifth day of the simulation as an indication of diapycnal mixing over the event. The vertical displacement of the thermocline is further used to diagnose internal wave generation and propagation in the model.

5.2.4 Satellite SST data

This chapter makes use of the Group for High Resolution Sea Surface Temperature (GHRSST) dataset for the Eastern Atlantic Region from the Spinning Enhanced Visible and InfraRed Imager (SEVIRI[1]) (OSISAF, 2015). The data are available at hourly intervals from June 2004 to present, on a 0.05° regular grid. Only data with a quality flag of 3 and greater are used in the presented analysis, as recommended in the scientific validation report for the product (SAF, 2018).

---

[1] `https://podaac.jpl.nasa.gov/dataset/SEVIRI_SST-OSISAF-L3C-v1.0`

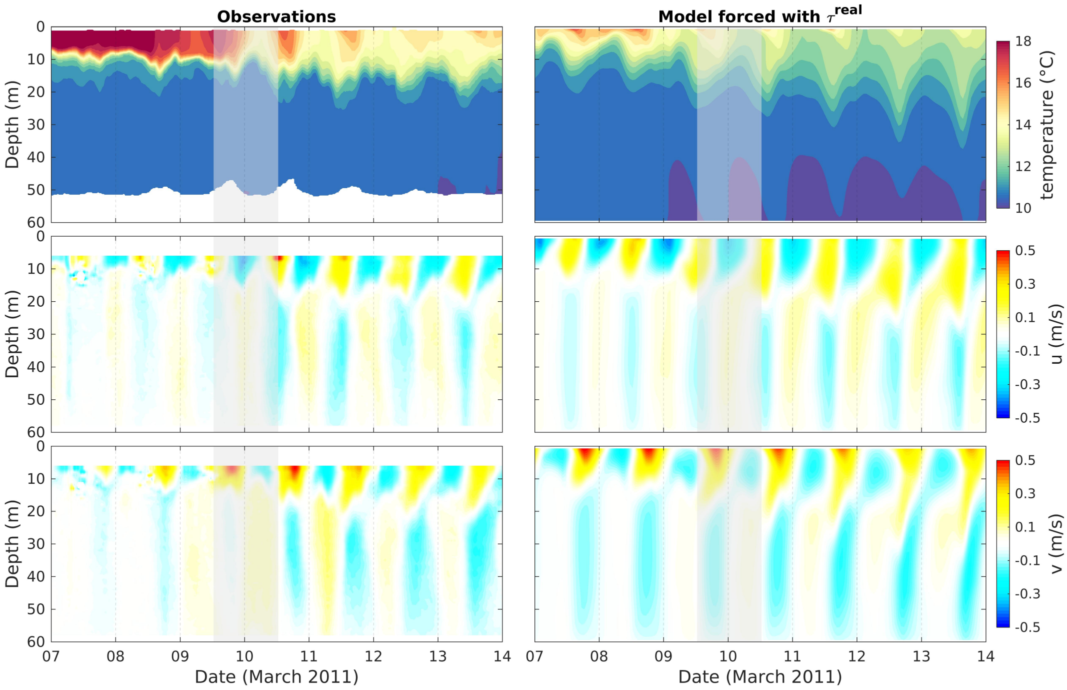

FIGURE 5.1: Observed (left) and modelled (right) temperature and horizontal velocity components over an upwelling event accompanied by diapycnal mixing at the Wirewalker fixed mooring in 60 m water depth ('WW' Station 1 in Figure 1.2). The shaded time denotes the period considered in Figure 5.2.

5.3 Results

5.3.1 Diurnal variability in SST

In Chapter 2 we compared the temporal evolution of temperature and horizontal velocity components from the offshore Wirewalker mooring with the simulation forced with τ^{real} over the month of March 2011 (Figures 2.8 and 2.9). In Figure 5.1 we present a 7 day subset of this comparison, corresponding to the upwelling/mixing event which was given particular attention in Chapters 3 and 4. The reasonable agreement between the modelled and observed diurnal variability in the vertical water column structure provides some confidence that the model can be used to gain further insight into the spatial and temporal variability of the processes at play.

The shaded area in Figure 5.1 denotes a 24 hour period which is characterised by the onset of strong diurnal variability in surface temperatures, both in the observations and in the model. The evolution of the spatial variability in sea surface temperature (SST) and surface currents over St Helena Bay for this 24 hour period is further

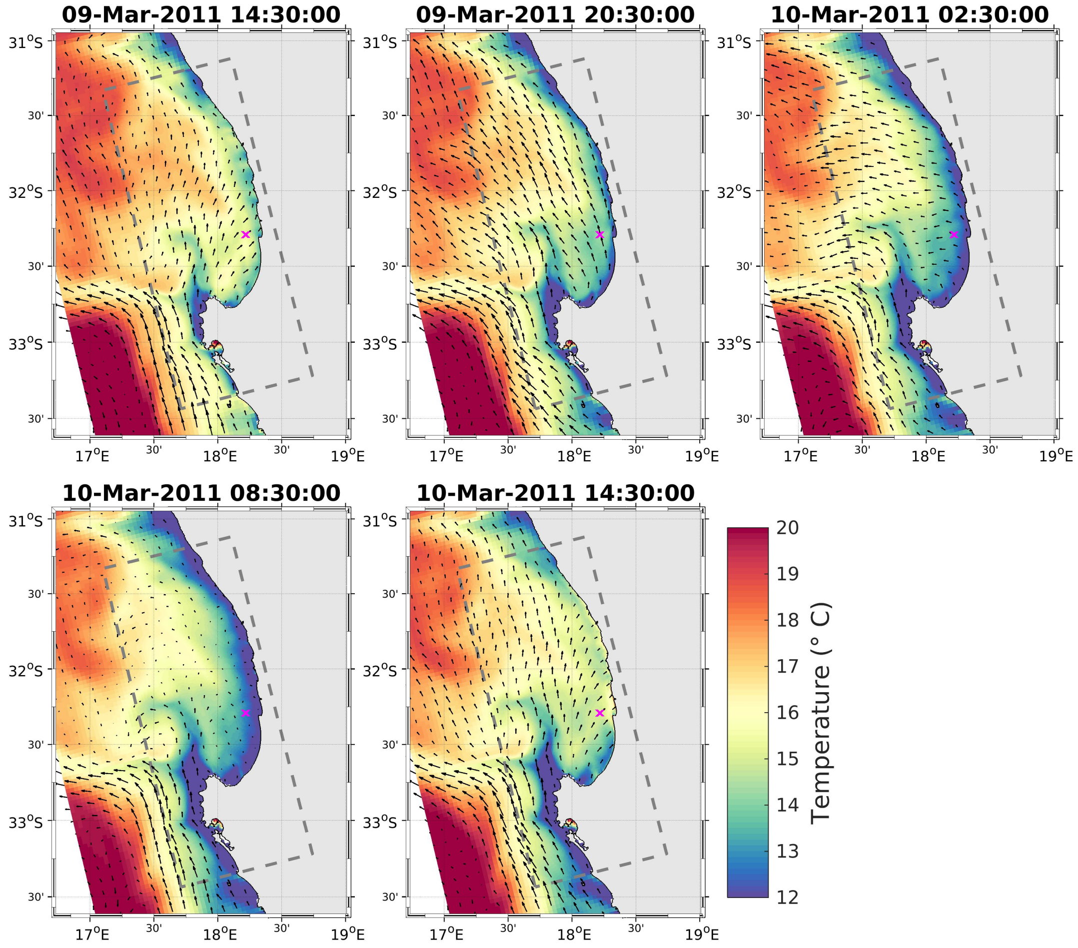

FIGURE 5.2: 6 hourly snapshots of modelled SST and surface current vectors over an upwelling event, demonstrating the outcropping and subduction of the inner shelf upwelling front over a day in response to inertial motions. The Wirewalker observations (denoted by the magenta cross) capture the strong diurnal variability in SST, as shown in Figure 5.1. Times are local time, UTC+2.

assessed in Figure 5.2. Before describing the diurnal variability in SST and surface currents revealed by Figure 5.2, it is worthwhile noting that the event displays some typical features of the upwelling system, as documented in the literature and summarised in Chapter 1.3. For instance, intensified upwelling associated with the Cape Columbine upwelling cell is evident, as is the bifurcation of the equatorward Goodhope Jet into offshore and alongshore components north of Cape Columbine. The alongshore component corresponds to the Columbine Jet, which effectively defines the dynamic offshore boundary of St Helena Bay.

Figure 5.2 reveals substantial diurnal variability in both SST and surface currents, particularly within the nearshore region of St Helena Bay. The cross-shore component of the surface current is offshore at night, turning to onshore during daylight hours. The phase of the surface current is therefore tied to that of the local land-sea breeze component of the winds (shown in Figure 3.1), suggesting that these currents are driven by the diurnal-inertial resonance phenomenon. A narrow strip of cold water is shown to be upwelled on the inner shelf within St Helena Bay during the night (e.g. refer to the 08:30:00 time-step). Six hours later, however, the newly upwelled waters are once again subducted. This high frequency variability in SST's is consistent with the onset of outcropping of the upwelling front due to sub-inertial upwelling, in combination with the advection of the upwelling front by the diurnal-inertial currents. These processes contribute to temperature variability of greater than 5°C within the inner shelf regions of St Helena Bay over the considered 24 hour period.

Diurnal-inertial current variability is a ubiquitous feature of the region (Fawcett et al., 2008; Lucas et al., 2014). This is particularly true over upwelling events as the amplitude of the land-sea breeze (as quantified by the diurnal anticlockwise rotary component of the wind stress, τ^{ac}) is correlated with the sub-inertial alongshore winds (Figure 3.14). The associated day-night differences in SST's, driven by the outcropping and subduction of the upwelling front by diurnal-inertial currents, is therefore an expected feature of the region. In an attempt to quantify this effect we present daytime (14:00:00) vs nighttime (02:00:00) climatologies of SST for the region, derived from daily snapshots of the realistically forced model solution (τ^{real}) at these

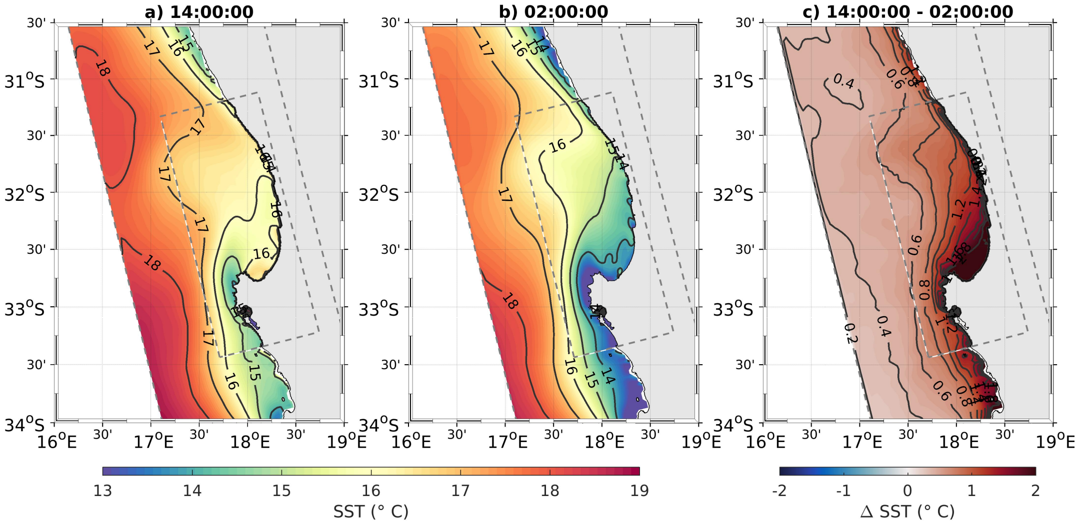

FIGURE 5.3: Climatology of modelled SST for the 'upwelling' months of October - March from the simulation forced with τ^{real}. a) Climatology computed from snapshots at 14:00:00. b) Climatology computed from snapshots at 02:00:00. c) The difference between climatologies computed at 14:00:00 and 02:00:00. Times are local time, UTC+2.

times (Figure 5.3). The analysis is restricted to the nominally 'upwelling' months of October - March. The difference between the two climatologies reveals that SST's computed during the day are consistently warmer than those at night over the entire domain, and that the effect becomes more enhanced towards the coast. The effect is particularly stark within the inner shelf region of St Helena Bay, where the climatological difference exceeds 2°C over much of the bay.

It is acknowledged that a proportion of the day-night differences in nearshore SST could be attributed to diurnal variability in surface heat fluxes driven by solar irradiance (the land-sea breeze is itself a product of diurnal heating/cooling over the land and ocean). To distill the relative importance of the diurnal-inertial oscillations and surface heat fluxes, we make use of the simulation forced with τ^{daily} (Table 5.1). The heat fluxes are the same in the simulations forced with τ^{real} and τ^{daily}, however the response to the high frequency winds are excluded in the simulation forced with τ^{daily}, allowing us to filter out the role of the heat fluxes in driving diurnal variability in SST's. By subtracting the computed diurnal variability in SST driven by heat fluxes alone (Figure 5.4b) from the total diurnal variability (Figure 5.4a) , we provide an estimate of the diurnal variability driven by the high frequency winds alone (Figure 5.4c). The influence of the land-sea breeze on the diurnal fluctuations in SST is

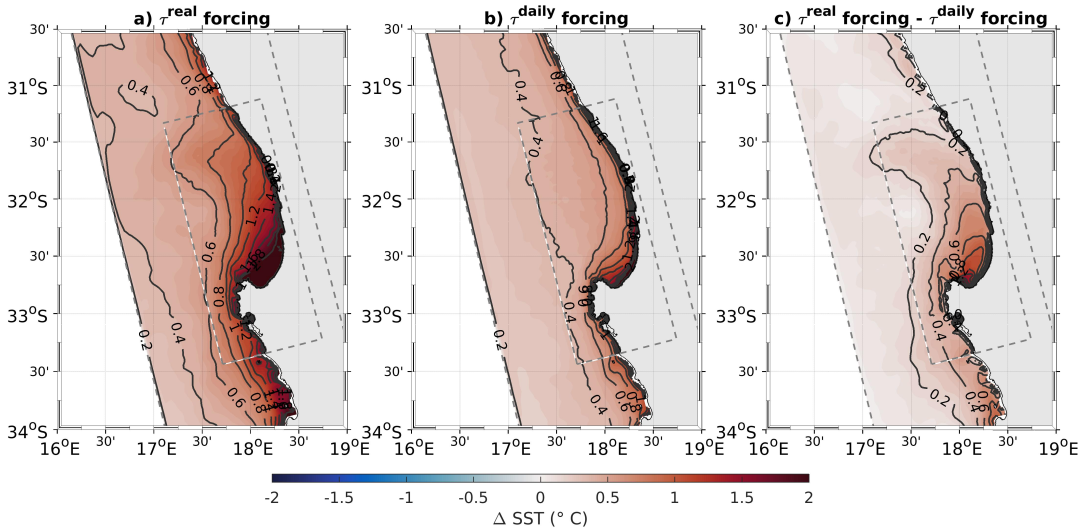

FIGURE 5.4: Difference between modelled climatologies of SST computed at 14:00:00 and 02:00:00 (local time, UTC+2) for the upwelling months of October - March. a) Simulation forced with τ^{real}, reflecting the overall diurnal variability in SST. b) Simulation forced with τ^{daily}, reflecting the diurnal variability in SST driven by diurnal surface fluxes alone. c) The difference between the two simulations (a-b), reflecting the diurnal variability in SST driven by super-diurnal wind variability alone.

shown to be particularly enhanced in the nearshore region of St Helena Bay, where the climatological difference exceeds 1°C. Diurnal warming due to solar irradiance is also enhanced in the southern extent of the bay, leading to the pronounced combined effect.

We now make us of the GHRSST-SERVIRI satellite product (OSISAF, 2015) to provide further insight into the diurnal variability in remotely sensed SST over the region of interest. Unlike many other satellite products, the geostationary orbit of the satellite allows for observations to be made available at an hourly temporal resolution. Figure 5.5 presents 15 year (2005-2019) SST climatologies for the nominally upwelling months of October - March, as computed from satellite SST observations at 14:00:00 and 02:00:00 (local time, UTC+2). It is immediately apparent from the presented analysis that the SST's computed from the GHRSST-SERVIRI satellite data are significantly warmer than those computed from the model, particularly in regions where upwelling is greatest. Given that the nearshore temperature bias in the model

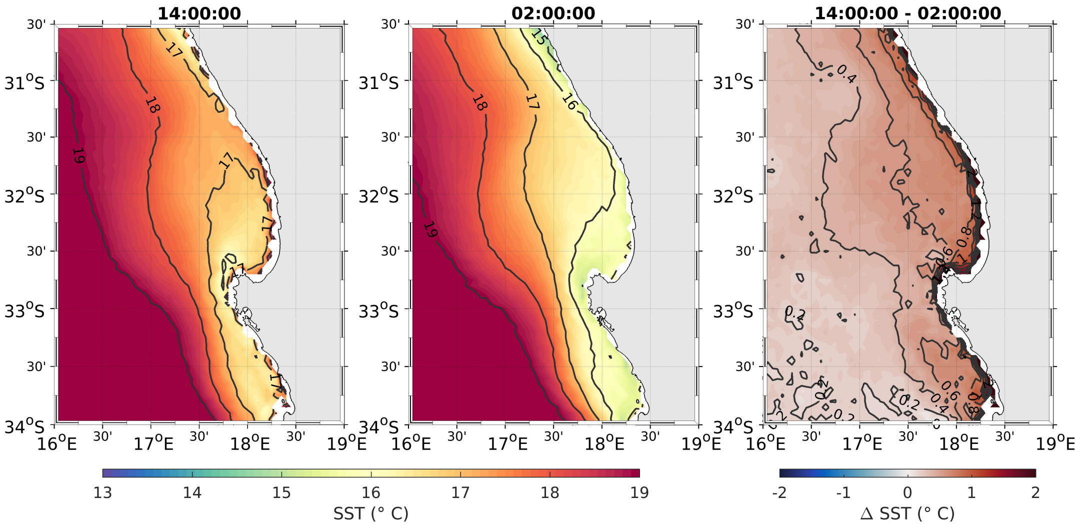

FIGURE 5.5: As per Figure 5.3 but derived from GHRSST-SEVIRI satellite SST data.

has been shown to be low (<1°C) when compared with in-situ observations (Chapter 2), it is suggested that the nearshore climatologies computed from the GHRSST-SERVIRI satellite data are too warm. Flagging techniques used to 'de-cloud' thermal infrared satellite data are known to contribute to large warm biases in upwelling systems (Dufois et al., 2012; Smit et al., 2013; Meneghesso et al., 2020). The flagging of cold upwelled water as missing data in the processing of the observations is posited as the explanation for the discrepancy. The difference between the satellite derived SST climatologies at 14:00:00 and 02:00:00 reveal similar patterns to that computed from the model, namely that SST's at 14:00:00 are systematically warmer than those at 02:00:00, and that the difference increases towards the coast. The effect in the nearshore regions of St Helena Bay is however not as exaggerated as revealed in the model results.

5.3.2 Event-scale diapycnal mixing

We now use the 3D model to further explore the processes governing event-scale diapycnal mixing driven by land-sea breeze forcing near the critical latitude. The analysis is carried out on two simulations, each over a 7 day period and each initialised on 25 January 2007 from the simulation forced with τ^{daily}, as described in Section 5.2.3. The initial SST and vertical section of temperature for the experiments

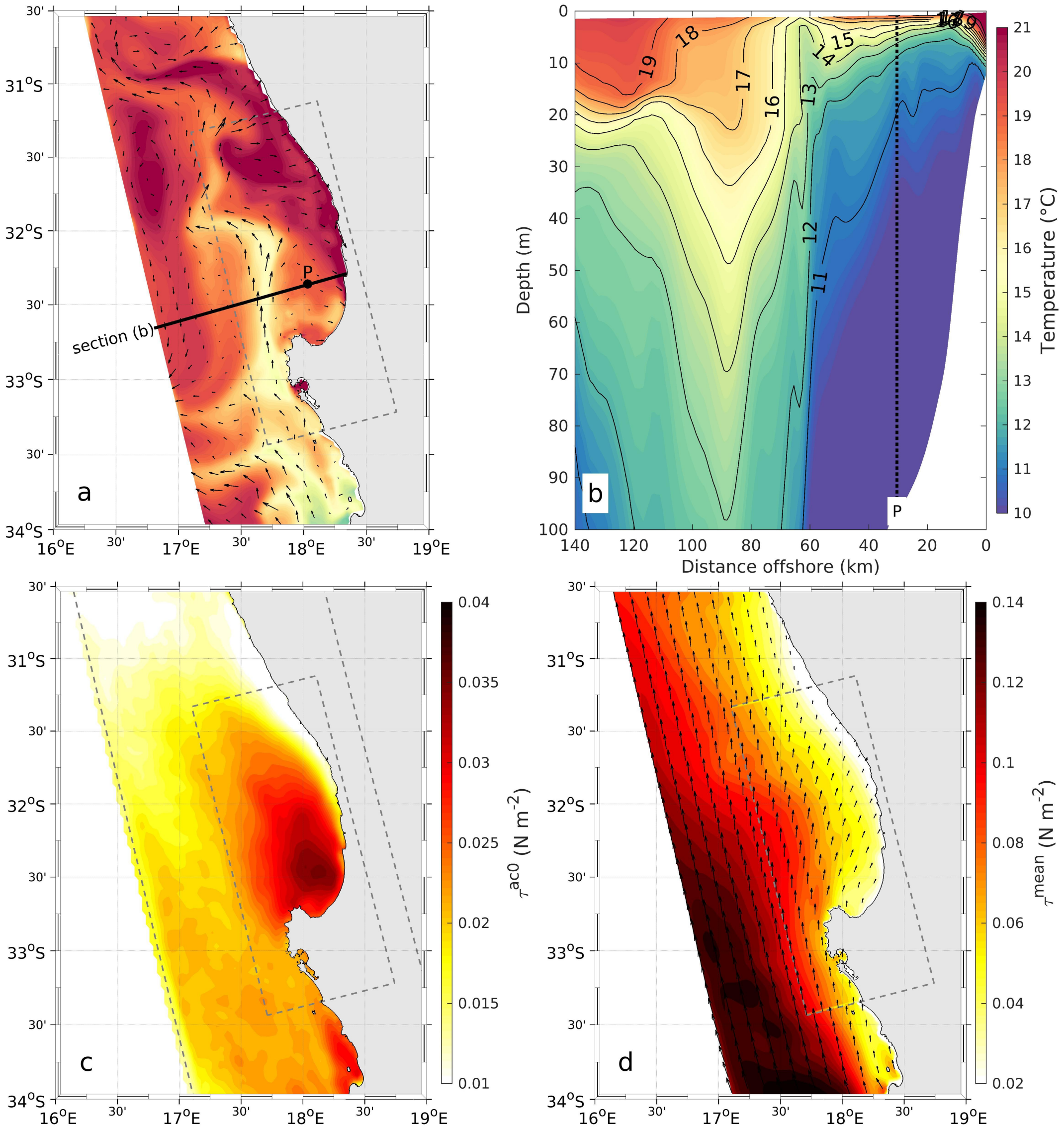

FIGURE 5.6: Initial temperature condition and wind forcing for 7 day experiments initialised on 25 January 2007 from the model forced with τ^{daily}. a) Sea surface temperature. b) vertical section of temperature across the model domain over the upper 100 m of the water column. c) Amplitude of the diurnal anticlockwise rotary component of the wind stress (τ^{ac0}) over the 7 day duration of the experiments. d) Mean wind stress (τ^{mean}) over the 7 day duration of the experiments.

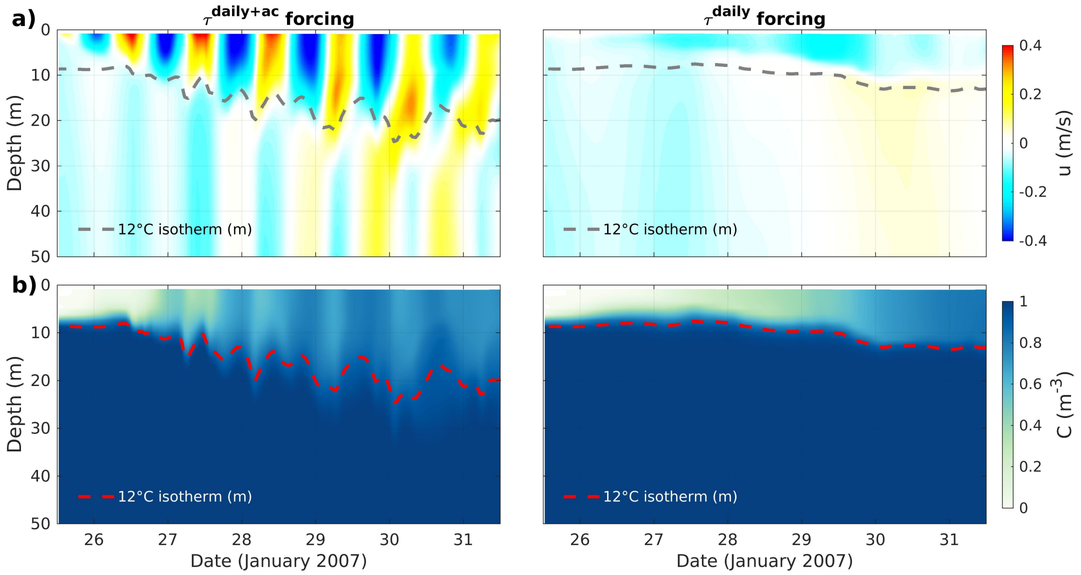

Figure 5.7: Temporal evolution of the model solution for the cross-shore component of velocity (a) and the passive tracer (b) over the upper 50 m of the water column at a location in the centre of St Helena Bay ('P' in Figure 5.6). The model is initialised on 25 January 2007 and forced with both $\tau^{daily+ac}$ (left panels) and τ^{daily} (right panels).

are shown in Figure 5.6a,b. The subsequent 7 day period is characterised by upwelling favourable sub-inertial winds (τ^{mean}), accompanied by an elevated amplitude in the diurnal anticlockwise rotary component of the winds (τ^{ac0}), as shown in Figure 5.6c,d.

Figure 5.7 shows the temporal evolution of the cross-shore component of velocity and the passive tracer at a location in the centre of St Helena Bay ('P' in Figure 5.6). The comparison of simulations forced both $\tau^{daily+ac}$ (left panels) and τ^{daily} (right panels) clearly demonstrates how the inclusion of τ^{ac} leads to shear-driven deepening of the thermocline in response to the diurnal-inertial resonance phenomenon and the associated injection of subsurface waters into the surface layer. The 12°C isotherm is also shown as a proxy for the interface between the surface and subsurface layers, revealing a complex pattern of thermocline displacements. These thermocline displacements can be interpreted from the Hovmöller diagram shown in Figure 5.8. Note that the missing data in the model output shown in Figure 5.8 corresponds to the outcropping of the 12°C isotherm, used to denote the thermocline.

At the land boundary, the land-sea breeze is shown to drive large vertical displacements of the thermocline with a diurnal frequency. The forcing mechanism for these

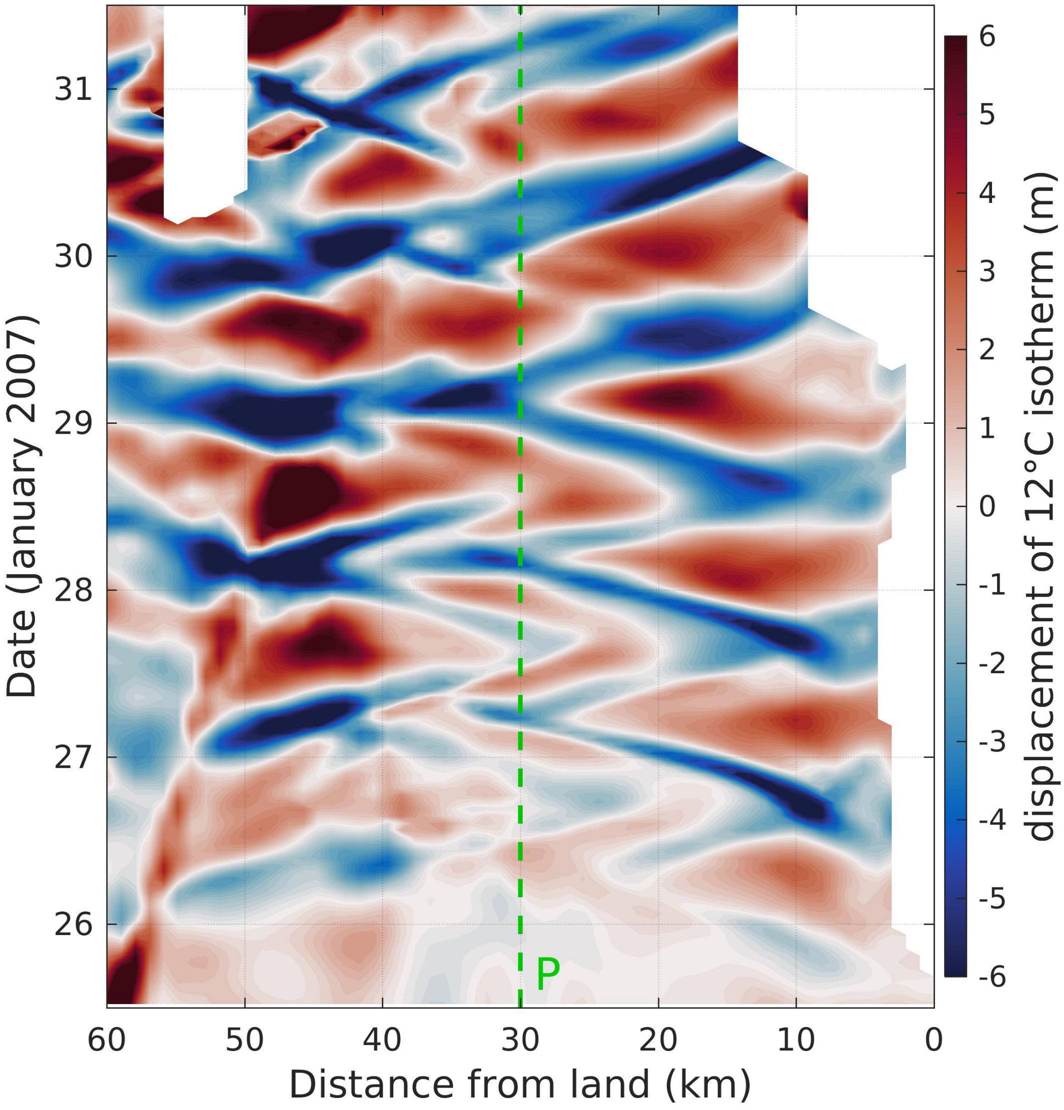

FIGURE 5.8: Hovmöller diagram of the displacement of the 12°C isotherm from the daily running average isotherm depth, where blue (red) denotes downward (upward) displacement of the thermocline. The model is initialised on 25 January 2007 (Figure 5.6) and forced with $\tau^{daily+ac}$

displacements, and their offshore propagation as internal waves, was revealed in the 2D model experiments presented in Chapter 4. In accordance with Zhang et al. (2010), the internal wave response in the 3D model is shown to be evanescent, as St Helena Bay is located poleward of 30°S, where there is no solution to the dispersion relation for Poincare waves. The full 3D case however presents a more complex picture. The thermocline response at the offshore boundary of St Helena Bay (as defined by the Columbine upwelling plume and associated jet) is shown to be connected to that at the land boundary, such that upward thermocline displacements at the land boundary are coincident with downward thermocline displacements at the offshore extent of the bay, and vice versa. It is noted that this is not a model boundary effect since the boundary is located further offshore than the observed phenomenon. The offshore diurnal-inertial pumping of the thermocline is largely attributed to the heterogeneity in the depth of the Ekman layer (see Figure 5.6b), where the presence of the upwelling plume introduces spatial variability in the forced surface layer diurnal-inertial currents (Figure 3.15b). An additional mechanism for the offshore thermocline pumping lies in the spatial variability in the sub-inertial surface currents, where enhanced vorticity associated with the alongshore jet will also influence the spatial variability in the diurnal-inertial motions in this region (Weller, 1982; Klein et al., 2004; Elipot et al., 2010). The diurnal-inertial pumping of the thermocline at the offshore extent of St Helena Bay is shown to drive the landward propagation of evanescent internal waves, generating a complex internal wave field within the bay due to the constructive/ destructive interference of the onshore and offshore propagating internal waves.

Given that the 2D analytical experiments presented in Chapter 4 indicated a peak in diapycnal mixing at a distance of $\sim$25 km from the source of diurnal thermocline pumping, and that St Helena Bay is approximately 50 km wide, it is plausible that the landward propagating internal waves contribute to additional shear-driven mixing within St Helena Bay. While the contribution of this process is difficult to isolate in the 3D model, in Figure 5.9 we revisit the analytically configured 2D model of Chapter 4 in order to explore the effect of introducing a region of offshore thermocline pumping, representative of the response to the presence of the Columbine

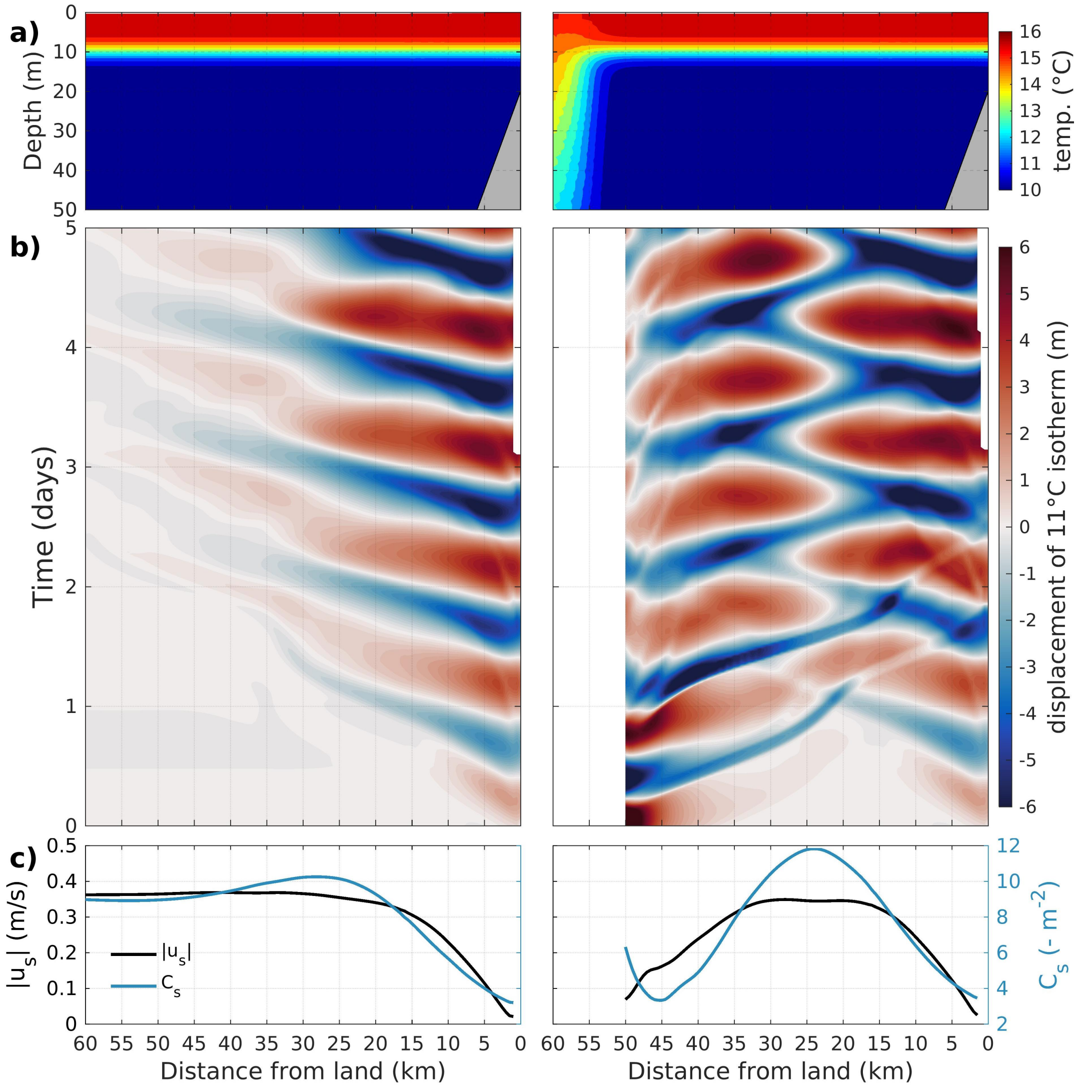

FIGURE 5.9: Comparison of analytically configured 2D model experiments. Left panels correspond to the 1:200 slope experiment shown in Figure 4.6, while the right panels show the result of introducing a region of convergence/ divergence at ∼50 km from the land boundary. a) Initial condition for temperature. b) Hovmöller diagram of the displacement of the 11°C isotherm from the daily running average isotherm depth, where blue (red) denotes downward (upward) displacement of the thermocline. c) Amplitude of the surface layer velocity ($|\overrightarrow{u_s}|$), and passive tracer concentration integrated over the surface layer (C_s), both averaged over the fifth day the simulation. Results are computed from a 7 day integration of the models with input parameters τ^{ac0} = 0.03 N m^{-2}, initial MLD =10 m, initial stratification (ΔT) = 6° C. Data inside the sponge layer of the model are not plotted.

upwelling plume. The experiment shown in the panels on the left of Figure 5.9 is the 1:200 slope experiment shown in Figure 4.6, while the experiment shown on the right of Figure 5.9 adopts a reduced offshore extent of the model (60 km) and we adopt temporally constant offshore boundary conditions computed from the 3D model climatology at the corresponding offshore distance, over the upwelling months of October - March. The analytical temperature profile in the nearshore is blended into the offshore boundary condition using a hyperbolic tangent function over the sponge layer of the model (10 km wide), the result of which is shown in Figure 5.9a (right panel). The intention of this offshore boundary condition is purely to introduce a source of diurnal thermocline pumping at a distance of $\sim$50 km from the land boundary. The Hovmöller diagram of the displacement of the 11°C isotherm (Figure 5.9b) indicates that this is achieved, resulting in an internal wave field which is qualitatively similar to that shown in Figure 5.8. The landward propagating internal waves are shown to contribute to an elevation in diapycnal mixing within the bay, with a peak in vertical mixing located roughly mid-way between the land boundary and the source of offshore thermocline pumping, as evidenced by the increase in the tracer concentration over the surface layer, C_s (Figure 5.9c).

As described in Section 5.2.3, diapycnal mixing over the considered event is quantified through the passive tracer concentration integrated over the surface layer of the model (above the 12°C isotherm in this case), averaged over the fifth day of the simulation (C_s). Figure 5.10 shows the spatial variability in the impact of the rotary component of the wind stress (τ^{ac}) on C_s. This is quantified by subtracting C_s computed from the simulation forced by τ^{daily} from C_s computed from the simulation forced by $\tau^{daily+ac}$ i.e. $\Delta C_s = C_{s\_\tau^{daily+ac}} - C_{s\_\tau^{daily}}$. The analysis indicates that land-sea breeze-driven diapycnal mixing is particularly enhanced within St Helena Bay for the considered event. It should however be noted that the shown footprint of enhanced vertical mixing is a result of a combination of vertical turbulence and advection over the experiment i.e. diapycnal mixing which occurred within the inner shelf at the start of the simulation would have been advected offshore due to Ekman transport by the fifth day of the simulation.

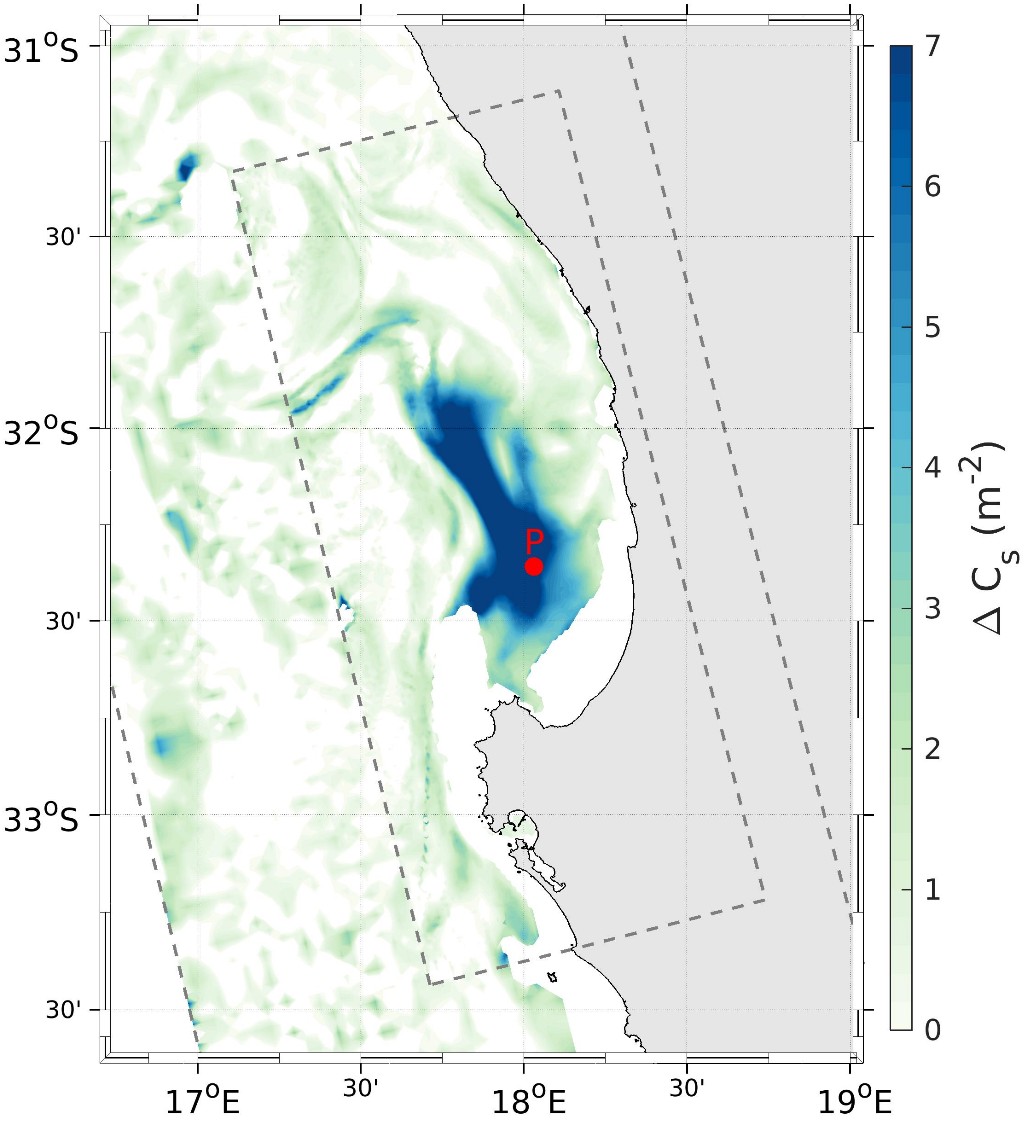

FIGURE 5.10: Increase in the passive tracer integrated from the 12°C isotherm to the surface (C_s) due to the inclusion of τ^{ac}, averaged over the fifth day of the simulation. The model is initialised on 25 January 2007 (Figure 5.6) and forced with both τ^{daily} and $\tau^{daily+ac}$. The effect of τ^{ac} on C_s is computed as $\Delta C_s = C_{s\_\tau^{daily+ac}} - C_{s\_\tau^{daily}}$.

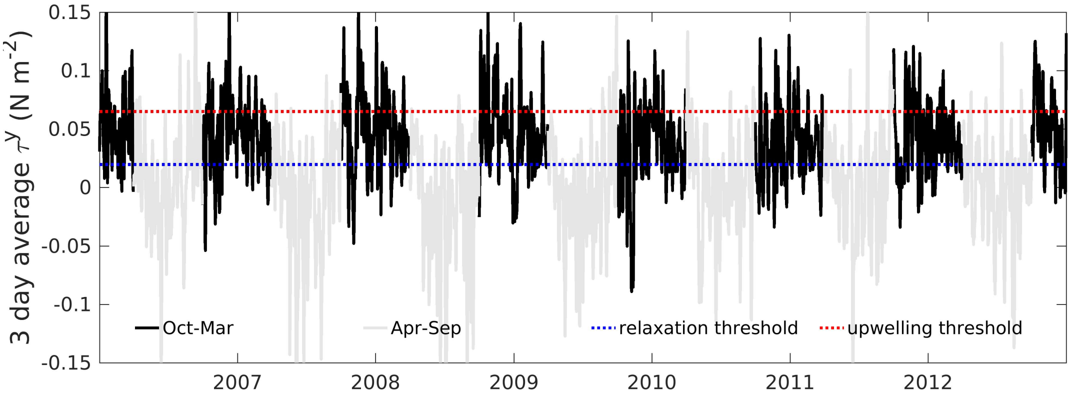

FIGURE 5.11: Time-series of 3 day average alongshore wind stress (τ^y) extracted from the model at a location in the centre of St Helena Bay ('P' in Figure 5.6). The shown relaxation and upwelling thresholds correspond to the 25th and 75th percentile τ^y for the nominally upwelling months of October - March.

5.3.3 Impacts on the mean ocean state

The results presented in this chapter thus far have focused on event-scale dynamics associated with the land-sea breeze. We now consider how these high-frequency processes affect the mean state of the vertical water column structure and circulation over the area of interest. This is achieved by comparing 7 year climatologies for simulations forced with τ^{daily} and $\tau^{daily+ac}$, thereby isolating the effect of the diurnal anticlockwise rotary component of the wind stress (τ^{ac}). Climatological comparisons are provided in Figures 5.12 and 5.13 for upwelling and relaxation wind regimes, respectively. We define these wind regimes according to the mean alongshore wind stress over the preceding 3 days of each time-step from a time-series of wind stress in the centre of St Helena Bay (Figure 5.11). We take active upwelling as times where the 75th percentile 3 day average alongshore wind stress is exceeded, while relaxation periods are identified as times where the 3 day average alongshore wind stress falls below the 25th percentile value. The analysis is confined to the nominally upwelling months of October - March, when the amplitude of the land-sea breeze is also at its highest (Figure 3.14). The presented climatologies for relaxation and upwelling regimes are therefore both computed from the same amount of model output ($12 \times 0.5 \times 0.25 = 1.5$ months per year).

The mean SST results for the upwelling wind regime (Figure 5.12a) indicate that the

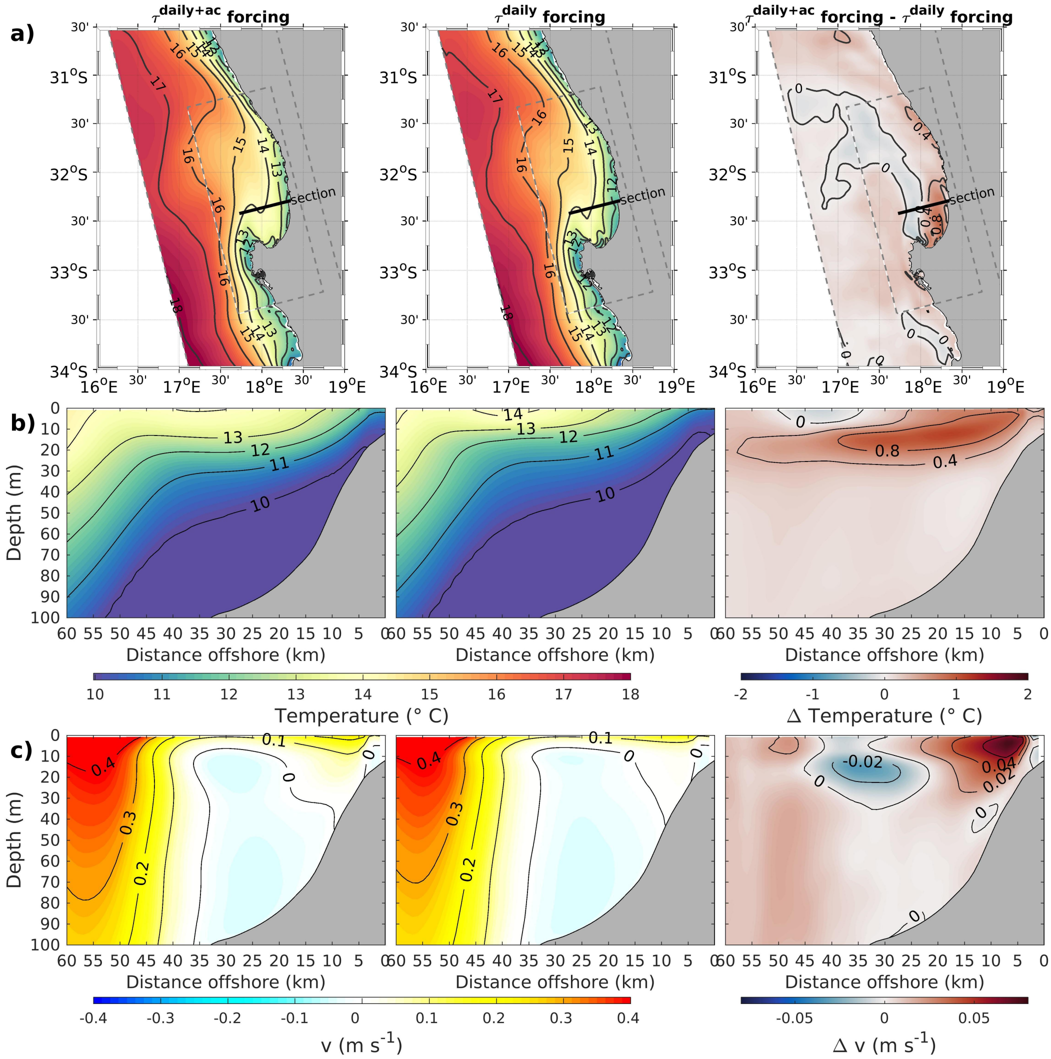

FIGURE 5.12: Impact of the diurnal anticlockwise rotary component of the wind stress (τ^{ac}) on the mean temperature and alongshore currents during upwelling conditions. The left panels show results for the simulation forced with $\tau^{daily+ac}$, the middle panels show results for the simulation forced with τ^{daily}, while the right panels show the difference between the two, highlighting the impact of τ^{ac}. a) Climatology of SST. b) Climatology of temperature for a vertical section through St Helena Bay (the location of the section is shown in (a)). c) Climatology of the equatorward (i.e. alongshore) component of horizontal velocity (v) for a vertical section through St Helena Bay.

effect of τ^{ac} is to lead to a marginal decrease in SST toward the outer extent of St Helena Bay, and a net warming of SST along the inner shelf of the bay. The simulation forced with $\tau^{daily+ac}$ is shown to result in a notably deeper mean thermocline than the simulation forced with τ^{daily} (Figure 5.12b). For example, at an offshore distance of 30 km, the mean 12°C isotherm depth is $\sim$14 m for the simulation forced with τ^{daily}, increasing to a depth of $\sim$21 m for the simulation forced with $\tau^{daily+ac}$. The resulting warmer subsurface waters (right panel of Figure 5.12b) is consistent with the effects of enhanced diapycnal mixing, however the net warming of the entire water column in the inner shelf region points to additional processes. It is suggested that the net warming in the coastal waters of St Helena Bay can be explained by the processes already elucidated with the 2D model presented in Chapter 4. The analytically configured experiment depicting a 'typical' upwelling event (Section 4.3.2) revealed how the deepened thermocline introduced by the land-sea breeze leads to a reduction in offshore advection of surface waters, as the same offshore Ekman transport is applied over a deeper surface layer. This process was found to be the primary driver of a net warming of nearshore surface waters, i.e. within the region under the influence of the upwelling front (Figure 4.8), which is qualitatively similar to that shown in Figure 5.12b.

Figure 5.12c shows how upwelling favourable wind conditions are accompanied by a strong equatorward current offshore of St Helena Bay (mean surface current $>$0.4 m s^{-1} at an offshore distance of $\sim$55 km) corresponding to the Columbine Jet, in geostrophic balance with the cross-shore pressure gradient set up by the Columbine upwelling plume. This jet current is not shown to be notably impacted by the rotary component of the wind stress (τ^{ac}), however alongshore currents within St Helena Bay (offshore distance $<\sim$40 km) are shown influenced in interesting ways. The model indicates that alongshore currents on the inner shelf ($<\sim$ 15 km offshore) are predominantly equatorward during periods of active upwelling, in agreement with local observations (Fawcett et al., 2008). It is suggested that geostrophic considerations can in part be used to explain the presence of the equatorward alongshore flow in this region, being a response to the cross-shore pressure gradient set up by the inner shelf upwelling. The inclusion of τ^{ac} is shown to enhance this alongshore flow.

In the area of maximum impact, the inclusion of τ^{ac} increases the mean equatorward alongshore current speed from 0.09 m s^{-1} to 0.17 m s^{-1} (right panel of Figure 5.12c). The deeper thermocline associated with the simulation forced with $\tau^{daily+ac}$ would serve to enhance the horizontal pressure gradients driving the mean alongshore flow, and is the suggested mechanism for the shown effect. Similarly, cross-shore pressure gradients set up at the offshore extent of the stratified surface layer within St Helena Bay would serve to drive the poleward alongshore flow, which is visible in both simulations (refer to depths of $\sim$10-30 m and offshore distances of $\sim$20-35 km). This poleward current is also shown to be enhanced by the inclusion of τ^{ac}, and can again be interpreted as a response to the deepened thermocline. In the area of maximum impact, the inclusion of τ^{ac} increases this mean poleward alongshore current speed from 0.02 m s^{-1} to 0.05 m s^{-1} (right panel of Figure 5.12c). Near-bottom currents within St Helena Bay are shown to be poleward and of similar structure in both simulations, which may in part be linked to negative wind stress curl through the Sverdrup relation (Veitch et al., 2010). This near-bottom alongshore flow is not notably impacted by the inclusion of τ^{ac}.

As expected, the absolute value of mean SST's during relaxation periods are shown to be significantly warmer than those during periods of active upwelling (Figure 5.13a vs Figure 5.12a). τ^{ac} is shown to drive cooler SST's over most of the model domain during periods of wind relaxation (right panel of Figure 5.13a). This effect is particularly evident within the nearshore regions of St Helena Bay, where the mean difference between the two simulations can exceed 2°C. Inspection of the vertical water column structure (Figure 5.13b) reveals that the lower SST's driven by τ^{ac} are compensated by warmer subsurface waters due to a deeper thermocline, consistent with the effects of enhanced diapycnal mixing. It is interesting to note that the net warming of the nearshore water column in response to τ^{ac} during upwelling periods (Figure 5.12b) is not at all present during periods of relaxation. This further supports the suggested mechanism for the net warming to be linked to reduced offshore Ekman advection of the surface layer, which would be absent during relaxation of alongshore winds.

Relaxation events are also associated with a significantly weakened Columbine Jet

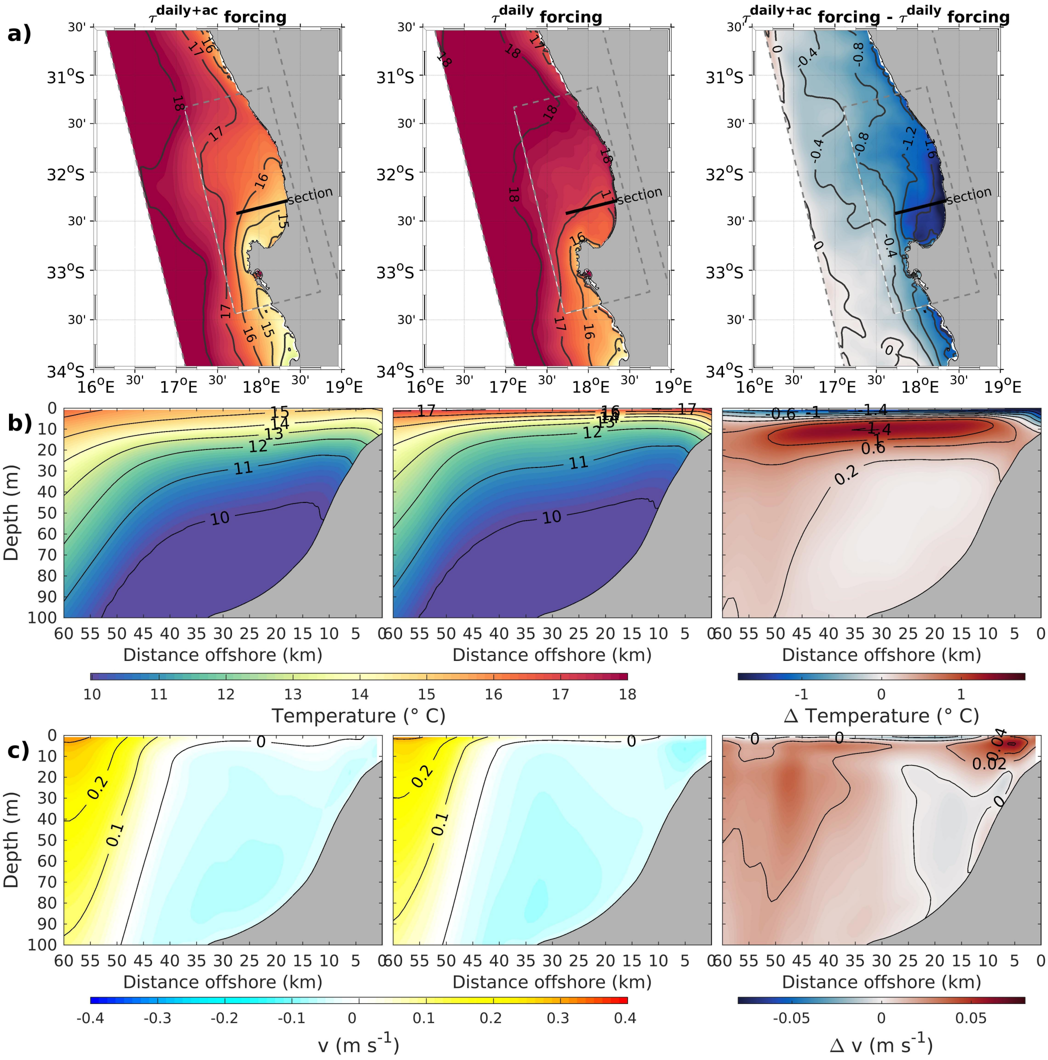

FIGURE 5.13: As per Figure 5.12 but for relaxation conditions.

(Figure 5.13c vs Figure 5.12c), consistent with reduced horizontal temperature gradients during these periods. Mean currents within St Helena Bay are shown to be poleward during wind relaxation, again consistent with inner shelf observations (Fawcett et al., 2008). The results indicate that τ^{ac} serves to weaken the poleward current in the near-coastal waters of St Helena Bay (i.e. <10 km from the coast). In the area of maximum impact, the inclusion of τ^{ac} reduces this mean poleward alongshore current speed from 0.08 m s^{-1} to 0.02 m s^{-1} (right panel of Figure 5.13c). It is suggested that this current can again be largely understood in terms of the cross-shore pressure gradients set up by the subduction of the thermocline during wind relaxation (an example of such a nearshore water column structure is shown Figure 5.6b). Such near-bottom horizontal pressure gradients set up during coastal downwelling events have been used to explain the development of strong poleward near-bottom currents in upwelling systems (Kämpf, 2019). A deeper thermocline induced by the inclusion of τ^{ac} would serve to weaken such horizontal gradients, in agreement with the results of the shown experiments.

5.4 Discussion and conclusions

In this chapter we have used a validated 3D model of the Southern Benguela upwelling system to explore the influence of the land-sea breeze on various aspects of the dynamics of the system. An over-arching finding, common to all of the presented analyses, is that the effects of land-sea breeze forcing are particularly enhanced within the inner shelf region of St Helena Bay. This finding is consistent with previous observational studies which have noted the ubiquitous presence of diurnal-inertial current variability in the nearshore regions of the bay (Fawcett et al., 2008; Lucas et al., 2014). In Chapter 3 it was hypothesised that St Helena Bay possesses a combination of physical characteristics which might promote a strong locally forced inertial response. These characteristics were identified as a near-critical latitude for diurnal-inertial resonance, a local enhancement of the diurnal anticyclonic rotary component of the wind stress (τ^{ac}), and the tendency for the development of a shallow stratified surface layer due to the retentive properties of the bay.

The 3D experiments presented in this chapter have provided further evidence confirming the importance of diurnal winds in driving high frequency variability and determining the mean state within St Helena Bay. Some of the implications of the land-sea breeze-driven variability are now considered.

5.4.1 Implications of enhanced diurnal variability in SST

A striking finding from the model is the extent to which SST's over the model domain vary at the diurnal frequency, with the effect increasing toward the coast and becoming particularly exaggerated within St Helena Bay. Over the upwelling months of October - March, modelled mean near-coastal daytime SST's are more than 2°C warmer than those at nighttime over much of St Helena Bay (Figure 5.3). Diurnal warming is one major driver, as would be expected under conditions of low winds and high solar irradiance (Stuart-Menteth et al., 2003). The model has revealed that in addition to diurnal warming in response to solar irradiance, the advection of strong SST gradients by diurnal-inertial surface oscillations forced by the land-sea breeze can account for more than half of the diurnal variability in near-coastal SST's, particularly in St Helena Bay where the response is greatest.

Comparisons of our model results with GHRSST-SERVIRI satellite SST observations are consistent with the previously established fact that satellite SST have important nearshore biases in upwelling systems, largely attributed to the flagging of cold upwelled water as missing data (Carr et al., 2020; Meneghesso et al., 2020). Our high frequency model output is therefore seen as a preferred reference for assessing diurnal variability in SST's over the southern Benguela. As satellite SST products are however often used to validate ocean models of upwelling systems, our results emphasise that the strong diurnal signature of SST in the coastal regions of these systems should at least be taken into account in such analyses. Even if satellite observations were hypothetically free from error, the aliasing of observations to a particular time of day would compromise a climatological comparison with temporally averaged data from a model, particularly within embayments near the critical latitude where large diurnal variability in SST's can be expected. Ideally, only model output corresponding to the times of the observations should be used in computing climatologies for comparison with the observations. It is further suggested that similar considerations would need to be made when using in-situ observations with a daily frequency. For instance, daily in-situ observations of coastal seawater temperature have provided a useful basis for computing monthly coastal temperature climatologies along the entire South African coastline (Smit et al., 2013). Our results however suggest that the time of day of these observations could play a large role in the outcome of the analysis and should be taken into account if the data are to be used as a ground truth for mean coastal SST's.

5.4.2 Implications of enhanced diapycnal mixing

The reduced physics experiments of Chapters 3 and 4 indicated that diapycnal mixing in response to the land-sea breeze near the critical latitude is predominantly driven by diurnal-inertial resonance of the locally forced response, while evanescent internal waves provide an additional source of shear-driven mixing. This chapter has allowed for the identification of these event-scale processes in a realistically configured model, confirming that the physical characteristics of St Helena Bay are particularly conducive to enhanced diapycnal mixing. This is especially true at the onset of upwelling events following a period of extended wind relaxation as in this case the wind forcing acts on a shallow stratified surface layer, leading to an exaggerated response. In addition to the processes already explored, the presented analysis in this chapter has identified the offshore extent of the bay, as defined by the Columbine upwelling plume, as an additional source of forced diurnal thermocline pumping, driving the landward propagation of evanescent internal waves. This can create a complex internal wave field due to their interaction with internal waves generated at the land boundary, providing an addition source of shear-driven mixing. It should however be noted that in reality the Columbine upwelling plume is by nature ephemeral, and when it is well defined its location and vertical structure are variable. This makes it difficult to quantify the overall significance of this process with respect to diapycnal mixing within St Helena Bay. Our results serve merely to illustrate the process.

The model indicates that the land-sea breeze is responsible for exaggerated diapycnal mixing over the area of interest, which is expressed as a 2°C cooling of SST's within St Helena Bay during wind relaxation conditions (Figure 5.13). Relaxation events are known to be accompanied by the development of a shallow thermocline within St Helena Bay due to the retentive properties of the bay and local solar irradiance. It is precisely these events which are favourable for the development and accumulation of high biomass blooms within the bay (Fawcett et al., 2007; Pitcher and Weeks, 2006). In Chapter 3 it was hypothesised that although relaxation events are generally associated with a lower amplitude land-sea breeze forcing, even low amplitude diurnal wind variability would serve to moderate the formation of shallow surface mixed layers through the entrainment of subsurface waters and nutrients. Furthermore, the effects of exaggerated mixing and nutrient injection to the surface layer during a prior upwelling event would set up the initial conditions for the subsequent relaxation event. The clear signature of enhanced diapycnal mixing during relaxation events provides strong support to the observational evidence that diapycnal nutrient flux induced by the land-sea breeze is of high importance in driving the overall productivity of the system (Lucas et al., 2014).

The analytically configured 2D experiments of Chapter 4 indicated that the enhanced diapycnal mixing induced by the land-sea breeze would lead to a reduction in subinertial offshore advection of the surface layer and a net warming of coastal waters during upwelling events. The results of this chapter confirm that this signature of reduced upwelling is indeed captured in a realistically configured model of the system. Advective losses during active upwelling can contribute to a reduction in productivity within upwelling systems, while the retention of upwelled waters is important for the accumulation of high biomass coastal blooms (Demarcq et al., 2007; Pitcher et al., 2010). Our results imply that the land-sea breeze plays a contributing role in the retentive properties of St Helena Bay through reduced offshore advection of the surface layer during upwelling events.

In addition to the impact of the land-sea breeze on the mean structure of the vertical water column, our results have further revealed its role in impacting mean alongshore currents, through its effect on cross-shore pressure gradients. The results during upwelling favourable conditions are in agreement with observations in the Coastal Southern California Bight which indicate that diurnal-inertial resonance can lead to steeper cross-shore isotherms and intensified alongshore flows (Nam and Send, 2013). The near-coastal poleward current set up by the subduction of the thermocline during relaxation events is however shown to be weakened by a deeper thermocline induced by diurnal-inertial resonance. These alongshore flows are important within the context of their role in setting up the retentive properties of St Helena Bay, thought to play a key role in its function as a main nursery ground for several fish species (Shelton and Hutchings, 1982; Huggett et al., 2003; Ragoasha et al., 2019). Our results suggest that the accurate simulation of this low frequency bay-scale retention in regional ocean models near the critical latitude may in part rely on the accurate spatial and temporal representation of the land-sea breeze in the forcing of these models.

Chapter 6

Conclusions and future directions

The objective of this thesis has been to improve our understanding of the physical response of EBUS to land-sea breeze forcing near the critical latitude of 30°N/S. This was achieved using a series of numerical experiments of increasing complexity, each aimed at highlighting specific processes and their implications within the context of EBUS. Reduced physics 1D-vertical and 2D-vertical numerical experiments were used to elucidate the key physical processes at play, while a realistically configured and validated 3D model has allowed for an assessment of the implications of these processes within the southern Benguela upwelling system.

1D-vertical experiments have improved our understanding of the locally forced response to the land-sea breeze and implications for diapycnal mixing. This was greatly aided by extending the 'Craig approximation' for the first order cross-shore surface elevation gradient response to include bottom friction terms. In so doing the forced response to water depth could be properly assessed, revealing the mechanics through which shallow depths ($<\sim$100 m) dampen surface oscillations and shear-driven mixing at the thermocline. The amplitude of the diurnal anticyclonic rotary component of the wind stress (τ^{ac0}) was revealed to be a good predictor of the locally forced response. Wind forecasts from high resolution regional atmospheric models can thus be used as a first order estimate of the expected diurnal-inertial currents and associated diapycnal mixing, particularly if the vertical water column structure is known. Sensitivity experiments showed the importance of the vertical water column structure, whereby shallow surface mixed layers promote exaggerated diapycnal mixing, which is moderated by stratification in line with Richardson number considerations.

2D-vertical experiments have provided insight into the cross-shore variability of the response to land-sea breeze forcing near the critical latitude. While shear-driven diapycnal mixing is largely governed by the locally forced response, evanescent internal waves generated by the convergence/ divergence of the forced response have been shown to contribute to shear-driven mixing, with a peak effect occurring $\sim$25 km from the land boundary. The internal wave response is however dampened in the presence of a gradually sloping bottom topography due to reduced convergence/ divergence of the forced response at the land boundary. In the presence of upwelling favourable sub-inertial winds, the land-sea breeze has been shown to introduce strong diurnal variability in nearshore temperatures, and reduce sub-inertial upwelling due to a deepened thermocline, thereby acting as a mechanism for retention of nearshore surface waters during upwelling events.

St Helena Bay ($\sim$32.5° S), in the southern Benguela upwelling system, has been used as a case study for further exploring the processes elucidated in the reduced physics experiments. The bay has been shown to possess a combination of physical characteristics which favour an enhanced response to the land-sea breeze, namely a near-critical latitude, a local enhancement of τ^{ac0}, and a tendency for the development of a shallow stratified surface layer due to the retentive properties of the bay. Here, high amplitude diurnal-inertial surface oscillations in the presence of steep horizontal sea surface temperature (SST) gradients contribute to large diurnal variability in SST. Event-scale diapycnal mixing dynamics revealed by the reduced physics experiments are clearly visible in the realistically configured 3D model. Additionally, the offshore dynamical extent of the bay, as defined by the variable location of the Columbine upwelling plume, was identified as a source of landward propagating internal waves which further contribute to diapycnal mixing within St Helena Bay. During wind relaxation events, the signature of enhanced diapycnal mixing due to land-sea breeze forcing was clearly evident by a drop in mean SST's. During upwelling events, the land-sea breeze was shown to drive a net warming of inner shelf waters due to the enhanced retention of the deepened thermocline, in agreement with the predictions of the 2D-vertical analytical configuration. The deepened thermocline was shown to have further implications for sub-inertial geostrophically-driven alongshore currents within St Helena Bay, which are strengthened (weakened) during upwelling (relaxation) events.

A recurring point of discussion throughout this thesis, and indeed a central motivation for it, has been how the land-sea breeze might contribute to the biogeochemical response of EBUS. It is clear from our results that the land-sea breeze drives enhanced diapycnal mixing in St Helena Bay, a finding which may translate to other retention zones in other EBUS near the critical latitude. Assessment of the spatial variability in diapycnal mixing was aided in this study by analysing the distribution of a passive tracer initialised below the surface layer. It seems altogether likely that subsurface nutrient enrichment of the surface layer associated with this process will contribute to the productivity of these systems. The indirect contribution of diapycnal mixing on reducing advective losses during upwelling is likely to have a further positive impact on productivity. The large diurnal variability in nearshore physical processes are also considered to play an important role in event-scale bloom dynamics. For instance, alignment of sub-inertial Ekman transport with diurnal-inertial surface oscillations leads to nighttime peaks in shear-driven mixing and surface layer nutrient enrichment, while onshore and downward displacement of the thermocline occurs during daylight hours. These processes and their timing with respect to sunlight availability may lead to short bursts of growth when conditions become favourable.

It is suggested that the numerical experiments presented in this thesis provide a good basis for further studies into the biogeochemical response of upwelling systems to land-sea breeze forcing near the critical latitude. For instance, the 2D-vertical model would provide a useful tool for testing the parameterisation of event-scale phytoplankton growth in biogeochemical models. Coupling the 3D physical model presented here with a suitable biogeochemical model could be used to quantify the impact of the land-sea breeze on the overall productivity of the southern Benguela. Similar studies in other EBUS may prove to be equally insightful. A general consideration for future studies is the requirement for atmospheric products of sufficient spatial and temporal resolution to capture the nearshore spatial variability in the land-sea breeze. This can be considerable where local orographic features and SST's may significantly impact nearshore diurnal wind variability. Similarly, the spatial resolution of 3D ocean models is required to be sufficiently high so as to capture the spatial variability in the forced response to the land-sea breeze. The inability to resolve the nearshore features of the land-sea breeze and the associated ocean response may be a significant shortcoming in large scale models which aim at simulating the productivity of EBUS. It is suggested that 3D physical-biogeochemical models that have already been set up with appropriate atmospheric forcing could be re-analysed through the lens provided by this thesis, to better understand if the biogeochemical response is influenced by the physics at these high frequency scales.

It is imperative that these modelling studies be supported by continued observations of the physical and biogeochemical response of EBUS. The high spatial and temporal variability of the processes at play however pose challenges for the design of such monitoring campaigns. Our understanding of the processes studied in this thesis would be benefit from the deployment of moorings similar to that of Lucas et al. (2014), but which cover the cross-shore extent of St Helena Bay, thereby capturing the full extent of the cross-shore variability predicted by the numerical experiments presented in this thesis.

Bibliography

Aguiar-González, Borja et al. (Aug. 2011). "Diurnal–Inertial Motions and Diapycnal Mixing on the Portuguese Shelf". en. In: *Continental Shelf Research* 31.11, pp. 1193–1201. ISSN: 02784343. DOI: `10.1016/j.csr.2011.04.015`.

Alford, Matthew H. (Aug. 2001). "Internal Swell Generation: The Spatial Distribution of Energy Flux from the Wind to Mixed Layer Near-Inertial Motions". en. In: *Journal of Physical Oceanography* 31.8, pp. 2359–2368. ISSN: 0022-3670, 1520-0485. DOI: `10.1175/1520-0485(2001)031<2359:ISGTSD>2.0.CO;2`.

Alford, Matthew H. et al. (Jan. 2016). "Near-Inertial Internal Gravity Waves in the Ocean". en. In: *Annual Review of Marine Science* 8.1, pp. 95–123. ISSN: 1941-1405, 1941-0611. DOI: `10.1146/annurev-marine-010814-015746`.

Bernard, S. et al. (2006). "12 The Requirements for Forecasting Harmful Algal Blooms in the Benguela". en. In: *Large Marine Ecosystems*. Vol. 14. Elsevier, pp. 273–294. ISBN: 978-0-444-52759-2. DOI: `10.1016/S1570-0461(06)80017-0`.

Bonicelli, Jessica et al. (Oct. 2014). "Spatial Differences in Thermal Structure and Variability within a Small Bay: Interplay of Diurnal Winds and Tides". en. In: *Continental Shelf Research* 88, pp. 72–80. ISSN: 0278-4343. DOI: `10.1016/j.csr.2014.07.009`.

Burchard, Hans and Tom P. Rippeth (Apr. 2009). "Generation of Bulk Shear Spikes in Shallow Stratified Tidal Seas". en. In: *Journal of Physical Oceanography* 39.4, pp. 969–985. ISSN: 0022-3670, 1520-0485. DOI: `10.1175/2008JPO4074.1`.

Burls, N. and C.J.C. Reason (Nov. 2008). "Modelling the Sensitivity of Coastal Winds over the Southern Benguela Upwelling System to Different SST Forcing". en. In: *Journal of Marine Systems* 74.1-2, pp. 561–584. ISSN: 09247963. DOI: `10.1016/j.jmarsys.2008.04.009`.

Capet, X. J., P. Marchesiello, and J. C. McWilliams (2004). "Upwelling Response to Coastal Wind Profiles". en. In: *Geophysical Research Letters* 31.13. ISSN: 1944-8007. DOI: `10.1029/2004GL020123`.

Carr, Matthew, Tarron Lamont, and Marjolaine Krug (2020). "Satellite Sea Surface Temperature Product Comparison for the Southern African Marine Region". en. In: *Remote Sensing* 12, p. 23.

Chavez, Francisco P. and Monique Messié (Dec. 2009). "A Comparison of Eastern Boundary Upwelling Ecosystems". en. In: *Progress in Oceanography*. Eastern Boundary Upwelling Ecosystems: Integrative and Comparative Approaches 83.1, pp. 80–96. ISSN: 0079-6611. DOI: `10.1016/j.pocean.2009.07.032`.

Chen, Changsheng and Liusen Xie (1997). "A Numerical Study of Wind-Induced, near-Inertial Oscillations over the Texas-Louisiana Shelf". en. In: *Journal of Geophysical Research: Oceans* 102.C7, pp. 15583–15593. ISSN: 2156-2202. DOI: `10.1029/97JC00228`.

Chen, Shengli, Daoyi Chen, and Jiuxing Xing (Oct. 2017). "A Study on Some Basic Features of Inertial Oscillations and Near-Inertial Internal Waves". en. In: *Ocean Science* 13.5, pp. 829–836. ISSN: 1812-0792. DOI: `10.5194/os-13-829-2017`.

Cockcroft, A. C. et al. (2000). "A Mass Stranding, Orwalk out'of West Coast Rock Lobster, Jasus Lalandii, in Elands Bay, South Africa: Causes, Results, and Implications". In: *Biodiversity Crisis and Crustacea*, pp. 673–688.

Craig, Peter D. (Nov. 1989). "A Model of Diurnally Forced Vertical Current Structure near 30° Latitude". en. In: *Continental Shelf Research* 9.11, pp. 965–980. ISSN: 02784343. DOI: `10.1016/0278-4343(89)90002-2`.

D'Asaro, Eric A. (Aug. 1985). "The Energy Flux from the Wind to Near-Inertial Motions in the Surface Mixed Layer". In: *Journal of Physical Oceanography* 15.8, pp. 1043–1059. ISSN: 0022-3670. DOI: `10.1175/1520-0485(1985)015<1043:TEFFTW>2.0.CO;2`.

D'Asaro, Eric A. et al. (Nov. 1995). "Upper-Ocean Inertial Currents Forced by a Strong Storm. Part I: Data and Comparisons with Linear Theory". In: *Journal of Physical Oceanography* 25.11, pp. 2909–2936. ISSN: 0022-3670. DOI: `10.1175/1520-0485(1995)025<2909:UOICFB>2.0.CO;2`.

de Souza, Joao Marcos Azevedo Correia et al. (Jan. 2020). “Evaluation of Four Global Ocean Reanalysis Products for New Zealand Waters–A Guide for Regional Ocean Modelling”. en. In: *New Zealand Journal of Marine and Freshwater Research*, pp. 1–24. ISSN: 0028-8330, 1175-8805. DOI: `10.1080/00288330.2020.1713179`.

Debreu, Laurent et al. (June 2012). “Two-Way Nesting in Split-Explicit Ocean Models: Algorithms, Implementation and Validation”. en. In: *Ocean Modelling* 49-50, pp. 1–21. ISSN: 14635003. DOI: `10.1016/j.ocemod.2012.03.003`.

Demarcq, H, R Barlow, and L Hutchings (Aug. 2007). “Application of a Chlorophyll Index Derived from Satellite Data to Investigate the Variability of Phytoplankton in the Benguela Ecosystem”. en. In: *African Journal of Marine Science* 29.2, pp. 271–282. ISSN: 1814-232X, 1814-2338. DOI: `10.2989/AJMS.2007.29.2.11.194`.

Desbiolles, F. et al. (Apr. 2016). “Response of the Southern Benguela Upwelling System to Fine-Scale Modifications of the Coastal Wind”. en. In: *Journal of Marine Systems* 156, pp. 46–55. ISSN: 09247963. DOI: `10.1016/j.jmarsys.2015.12.002`.

Dufois, François et al. (Jan. 2012). “On the Warm Nearshore Bias in Pathfinder Monthly SST Products over Eastern Boundary Upwelling Systems”. en. In: *Ocean Modelling* 47, pp. 113–118. ISSN: 1463-5003. DOI: `10.1016/j.ocemod.2012.01.007`.

Ekman, V. W. (1905). “On the Influence of the Earth’s Rotation on Ocean Currents”. In: *Arkiv för Matematik, Astronomi och Fysik* 2.11, pp. 1–53.

Elipot, Shane, Rick Lumpkin, and Germán Prieto (Sept. 2010). “Modification of Inertial Oscillations by the Mesoscale Eddy Field”. In: *Journal of Geophysical Research: Oceans* 115.C9. ISSN: 0148-0227. DOI: `10.1029/2009JC005679`.

Fairall, C. W. et al. (Feb. 1996). “Bulk Parameterization of Air-Sea Fluxes for Tropical Ocean-Global Atmosphere Coupled-Ocean Atmosphere Response Experiment”. en. In: *Journal of Geophysical Research: Oceans* 101.C2, pp. 3747–3764. ISSN: 01480227. DOI: `10.1029/95JC03205`.

Fairall, C. W. et al. (Feb. 2003). “Bulk Parameterization of Air–Sea Fluxes: Updates and Verification for the COARE Algorithm”. en. In: *Journal of Climate* 16.4, pp. 571–591. ISSN: 0894-8755, 1520-0442. DOI: `10.1175/1520-0442(2003)016<0571:BPOASF>2.0.CO;2`.

Fanning, Kent A., Kendall L. Carder, and Peter R. Betzer (Aug. 1982). “Sediment Resuspension by Coastal Waters: A Potential Mechanism for Nutrient Re-Cycling on the Ocean's Margins". en. In: *Deep Sea Research Part A. Oceanographic Research Papers* 29.8, pp. 953–965. ISSN: 0198-0149. DOI: `10.1016/0198-0149(82)90020-6`.

Fawcett, A et al. (Oct. 2007). "Contrasting Wind Patterns and Toxigenic Phytoplankton in the Southern Benguela Upwelling System". en. In: *Marine Ecology Progress Series* 348, pp. 19–31. ISSN: 0171-8630, 1616-1599. DOI: `10.3354/meps07027`.

Fawcett, A.L., G.C. Pitcher, and F.A. Shillington (May 2008). "Nearshore Currents on the Southern Namaqua Shelf of the Benguela Upwelling System". en. In: *Continental Shelf Research* 28.8, pp. 1026–1039. ISSN: 02784343. DOI: `10.1016/j.csr.2008.02.005`.

Flynn, R. F. et al. (2020). "On-Shelf Nutrient Trapping Enhances the Fertility of the Southern Benguela Upwelling System". en. In: *Journal of Geophysical Research: Oceans* 125.6, e2019JC015948. ISSN: 2169-9291. DOI: `10.1029/2019JC015948`.

Furevik, T. and A. Foldvik (1996). "Stability at M2 Critical Latitude in the Barents Sea". In: DOI: `10.1029/96JC00081`.

García-Reyes, M. et al. (2013). "Relative Influence of Oceanic and Terrestrial Pressure Systems in Driving Upwelling-Favorable Winds". en. In: *Geophysical Research Letters* 40.19, pp. 5311–5315. ISSN: 1944-8007. DOI: `10.1002/2013GL057729`.

Garzoli, S. L. and A. L. Gordon (1996). "Origins and Variability of the Benguela Current". en. In: *Journal of Geophysical Research: Oceans* 101.C1, pp. 897–906. ISSN: 2156-2202. DOI: `10.1029/95JC03221`.

Gille, Sarah T. (2003). "Measuring the Sea Breeze from QuikSCAT Scatterometry". en. In: *Geophysical Research Letters* 30.3. ISSN: 0094-8276. DOI: `10.1029/2002GL016230`.

– (2005). "Global Observations of the Land Breeze". en. In: *Geophysical Research Letters* 32.5. ISSN: 0094-8276. DOI: `10.1029/2004GL022139`.

Gruber, Nicolas et al. (Nov. 2011). "Eddy-Induced Reduction of Biological Production in Eastern Boundary Upwelling Systems". en. In: *Nature Geoscience* 4.11, pp. 787–792. ISSN: 1752-0908. DOI: `10.1038/ngeo1273`.

Haney, Robert L. (Apr. 1991). "On the Pressure Gradient Force over Steep Topography in Sigma Coordinate Ocean Models". en. In: *Journal of Physical Oceanography* 21.4, pp. 610–619. ISSN: 0022-3670. DOI: `10.1175/1520-0485(1991)021<0610:OTPGFO>2.0.CO;2`.

Herbert, R. A. (Oct. 1999). "Nitrogen Cycling in Coastal Marine Ecosystems". en. In: *FEMS Microbiology Reviews* 23.5, pp. 563–590. ISSN: 0168-6445. DOI: `10.1111/j.1574-6976.1999.tb00414.x`.

Hubbart, Bernadette et al. (Dec. 2012). "Toxigenic Phytoplankton and Concomitant Toxicity in the Mussel Choromytilus Meridionalis off the West Coast of South Africa". en. In: *Harmful Algae* 20, pp. 30–41. ISSN: 1568-9883. DOI: `10.1016/j.hal.2012.07.005`.

Huggett, Jenny et al. (2003). "Modelling the Transport Success of Anchovy <em>Engraulis Encrasicolus</Em> Eggs and Larvae in the Southern Benguela:: The Effect of Spatio-Temporal Spawning Patterns". In: *Marine Ecology Progress Series* 250, pp. 247–262. ISSN: 0171-8630.

Hyder, P. et al. (Oct. 2011). "Observations over an Annual Cycle and Simulations of Wind-Forced Oscillations near the Critical Latitude for Diurnal–Inertial Resonance". en. In: *Continental Shelf Research* 31.15, pp. 1576–1591. ISSN: 02784343. DOI: `10.1016/j.csr.2011.06.001`.

Jackett, David R. and Trevor J. Mcdougall (Apr. 1995). "Minimal Adjustment of Hydrographic Profiles to Achieve Static Stability". In: *Journal of Atmospheric and Oceanic Technology* 12.2, pp. 381–389. ISSN: 0739-0572. DOI: `10.1175/1520-0426(1995)012<0381:MAOHPT>2.0.CO;2`.

Jarosz, E., Z.R. Hallock, and W.J. Teague (Nov. 2007). "Near-Inertial Currents in the DeSoto Canyon Region". en. In: *Continental Shelf Research* 27.19, pp. 2407–2426. ISSN: 02784343. DOI: `10.1016/j.csr.2007.06.014`.

Jury, M. R. (June 1985). "Mesoscale Variations in Summer Winds over the Cape Columbine — St Helena Bay Region, South Africa". en. In: *South African Journal of Marine Science* 3.1, pp. 77–88. ISSN: 0257-7615. DOI: `10.2989/025776185784461162`.

Kämpf, Jochen (May 2019). "Extreme Bed Shear Stress during Coastal Downwelling". en. In: *Ocean Dynamics* 69.5, pp. 581–597. ISSN: 1616-7341, 1616-7228. DOI: `10.1007/s10236-019-01256-4`.

Kämpf, Jochen and Piers Chapman (2016). *Upwelling Systems of the World*. en. Cham: Springer International Publishing. ISBN: 978-3-319-42522-1 978-3-319-42524-5. DOI: `10.1007/978-3-319-42524-5`.

Kaplan, David M. et al. (June 2003). "Large Diurnal Temperature Fluctuations in the Nearshore Water Column". en. In: *Estuarine, Coastal and Shelf Science* 57.3, pp. 385–398. ISSN: 02727714. DOI: `10.1016/S0272-7714(02)00363-3`.

Kelly, Samuel M. (Nov. 2019). "Coastally Generated Near-Inertial Waves". en. In: *Journal of Physical Oceanography* 49.11, pp. 2979–2995. ISSN: 0022-3670, 1520-0485. DOI: `10.1175/JPO-D-18-0148.1`.

Klein, Patrice, Stefan Llewellyn Smith, and Guillaume Lapeyre (2004). "Organization of Near-Inertial Energy by an Eddy Field". en. In: *Quarterly Journal of the Royal Meteorological Society* 130.598, pp. 1153–1166. ISSN: 1477-870X. DOI: `10.1256/qj.02.231`.

Lamont, T. et al. (Apr. 2015). "Hydrographic Variability in the St. Helena Bay Region of the Southern Benguela Ecosystem: Hydrographic Variability in the Benguela". en. In: *Journal of Geophysical Research: Oceans* 120.4, pp. 2920–2944. ISSN: 21699275. DOI: `10.1002/2014JC010619`.

Large, W. G. and S. Pond (Mar. 1981). "Open Ocean Momentum Flux Measurements in Moderate to Strong Winds". In: *Journal of Physical Oceanography* 11.3, pp. 324–336. ISSN: 0022-3670. DOI: `10.1175/1520-0485(1981)011<0324:OOMFMI>2.0.CO;2`.

Lennard, Christopher et al. (Aug. 2015). "Development of a Numerical Wind Atlas for South Africa". en. In: *Energy Procedia* 76, pp. 128–137. ISSN: 18766102. DOI: `10.1016/j.egypro.2015.07.873`.

Lincoln, B. J., T. P. Rippeth, and J. H. Simpson (Aug. 2016). "Surface Mixed Layer Deepening through Wind Shear Alignment in a Seasonally Stratified Shallow Sea: Wind-Driven Mixed Layer Deepening". en. In: *Journal of Geophysical Research: Oceans* 121.8, pp. 6021–6034. ISSN: 21699275. DOI: `10.1002/2015JC011382`.

Lucas, Andrew J. et al. (Mar. 2014). "The Influence of Diurnal Winds on Phytoplankton Dynamics in a Coastal Upwelling System off Southwestern Africa". en. In: *Deep Sea Research Part II: Topical Studies in Oceanography* 101, pp. 50–62. ISSN: 09670645. DOI: `10.1016/j.dsr2.2013.01.016`.

Lutjeharms, J. R. E. and J. M. Meeuwis (June 1987). "The Extent and Variability of South-East Atlantic Upwelling". en. In: *South African Journal of Marine Science* 5.1, pp. 51–62. ISSN: 0257-7615. DOI: `10.2989/025776187784522621`.

Marchesiello, Patrick, James C. McWilliams, and Alexander Shchepetkin (Jan. 2001). “Open Boundary Conditions for Long-Term Integration of Regional Oceanic Models”. en. In: *Ocean Modelling* 3.1-2, pp. 1–20. ISSN: 14635003. DOI: `10.1016/S1463-5003(00)00013-5`.

– (Apr. 2003). “Equilibrium Structure and Dynamics of the California Current System”. en. In: *Journal of Physical Oceanography* 33.4, pp. 753–783. ISSN: 0022-3670, 1520-0485. DOI: `10.1175/1520-0485(2003)33<753:ESADOT>2.0.CO;2`.

Meneghesso, Claudia et al. (Feb. 2020). “Remotely-Sensed L4 SST Underestimates the Thermal Fingerprint of Coastal Upwelling”. en. In: *Remote Sensing of Environment* 237, p. 111588. ISSN: 0034-4257. DOI: `10.1016/j.rse.2019.111588`.

Millot, C and M Crépon (1981). “Inertial Oscillations on the Continentral Shelf Aof the Gulf of Lions - Observations and Theory”. In: *Journal of Physical Oceanography* 11, pp. 639–657.

Nam, SungHyun and Uwe Send (Mar. 2013). “Resonant Diurnal Oscillations and Mean Alongshore Flows Driven by Sea/Land Breeze Forcing in the Coastal Southern California Bight”. en. In: *Journal of Physical Oceanography* 43.3, pp. 616–630. ISSN: 0022-3670, 1520-0485. DOI: `10.1175/JPO-D-11-0148.1`.

Nelson, G. and L. Hutchings (Jan. 1983). “The Benguela Upwelling Area”. en. In: *Progress in Oceanography* 12.3, pp. 333–356. ISSN: 00796611. DOI: `10.1016/0079-6611(83)90013-7`.

Oceans and Coastal Research (2017). *Preliminary Processed Downcast CTD Data from the St Helena Bay Monitoring Line Cruises from 2000 to 2017*.

Orlić, Mirko and Zoran Pasarić (June 2011). “A Simple Analytical Model of Periodic Coastal Upwelling”. en. In: *Journal of Physical Oceanography* 41.6, pp. 1271–1276. ISSN: 0022-3670, 1520-0485. DOI: `10.1175/JPO-D-10-05000.1`.

OSISAF (2015). “GHRSST Level 3C Atlantic Subskin Sea Surface Temperature from the Spinning Enhanced Visible and Infrared Imager (SEVIRI) on MSG-3 Weather Satellite (GDS2 Version)”. In: DOI: `10.5067/GHSEV-3C001`.

Pauly, D and V Christensen (1995). “Primary Production Required to Sustain Global Fisheries”. en. In: *Nature* 374, p. 4.

Penven, P et al. (2001). “A Regional Hydrodynamic Model of Upwelling in the Southern Benguela”. en. In: *South African Journal of Science*, p. 4.

Penven, Pierrick et al. (2000). “Simulation of a Coastal Jet Retention Process Using a Barotropic Model”. en. In: *Oceanologica Acta*, p. 21.

Pettigrew, Neal Robert (1980). *The Dynamics and Kinematics of the Coastal Boundary Layer off Long Island*. en. Woods Hole, MA: Massachusetts Institute of Technology and Woods Hole Oceanographic Institution. DOI: `10.1575/1912/3727`.

Pinkel, R. et al. (Mar. 2011). “The Wirewalker: A Vertically Profiling Instrument Carrier Powered by Ocean Waves”. en. In: *Journal of Atmospheric and Oceanic Technology* 28.3, pp. 426–435. ISSN: 0739-0572, 1520-0426. DOI: `10.1175/2010JTECHO805.1`.

Pitcher G. C., G and A. J. Boyd (1996). “Accross-Shelf and Alongshore Dinoflagellate Distributions and the Mechanisms of Red Tide Formation within the Southern Benguela Upwelling System”. In: *Harmful and Toxic Algal Blooms*, pp. 243–246.

Pitcher, G. C. and D. Calder (June 2000). “Harmful Algal Blooms of the Southern Benguela Current: A Review and Appraisal of Monitoring from 1989 to 1997”. en. In: *South African Journal of Marine Science* 22.1, pp. 255–271. ISSN: 0257-7615. DOI: `10.2989/025776100784125681`.

Pitcher, Gc et al. (1998). “Subsurface Dinoflagellate Populations, Frontal Blooms and the Formation of Red Tide in the Southern Benguela Upwelling System”. en. In: *Marine Ecology Progress Series* 172, pp. 253–264. ISSN: 0171-8630, 1616-1599. DOI: `10.3354/meps172253`.

Pitcher, G.C. et al. (Apr. 2010). “The Physical Oceanography of Upwelling Systems and the Development of Harmful Algal Blooms”. en. In: *Progress in Oceanography* 85.1-2, pp. 5–32. ISSN: 00796611. DOI: `10.1016/j.pocean.2010.02.002`.

Pitcher, Grant C. and Greville Nelson (Nov. 2006). “Characteristics of the Surface Boundary Layer Important to the Development of Red Tide on the Southern Namaqua Shelf of the Benguela Upwelling System”. en. In: *Limnology and Oceanography* 51.6, pp. 2660–2674. ISSN: 00243590. DOI: `10.4319/lo.2006.51.6.2660`.

Pitcher, Grant C. and Trevor A. Probyn (Nov. 2011). “Anoxia in Southern Benguela during the Autumn of 2009 and Its Linkage to a Bloom of the Dinoflagellate Ceratium Balechii”. en. In: *Harmful Algae* 11, pp. 23–32. ISSN: 15689883. DOI: `10.1016/j.hal.2011.07.001`.

Pitcher, Grant C. and Scarla J. Weeks (Jan. 2006). “7 The Variability and Potential for Prediction of Harmful Algal Blooms in the Southern Benguela Ecosystem”. In:

Large Marine Ecosystems. Ed. by Vere Shannon et al. Vol. 14. Benguela. Elsevier, pp. 125–146. DOI: `10.1016/S1570-0461(06)80012-1`.

Pitcher, Grant C. et al. (Apr. 2014). "Dynamics of Oxygen Depletion in the Nearshore of a Coastal Embayment of the Southern Benguela Upwelling System". en. In: *Journal of Geophysical Research: Oceans* 119.4, pp. 2183–2200. ISSN: 21699275. DOI: `10.1002/2013JC009443`.

Pollard, R. T. (Mar. 1980). "Properties of Near-Surface Inertial Oscillations". In: *Journal of Physical Oceanography* 10.3, pp. 385–398. ISSN: 0022-3670. DOI: `10.1175/1520-0485(1980)010<0385:PONSIO>2.0.CO;2`.

Pollard, R.T. (Aug. 1970). "On the Generation by Winds of Inertial Waves in the Ocean". en. In: *Deep Sea Research and Oceanographic Abstracts* 17.4, pp. 795–812. ISSN: 00117471. DOI: `10.1016/0011-7471(70)90042-2`.

Pollard, R.T. and R.C. Millard (Aug. 1970). "Comparison between Observed and Simulated Wind-Generated Inertial Oscillations". en. In: *Deep Sea Research and Oceanographic Abstracts* 17.4, pp. 813–821. ISSN: 00117471. DOI: `10.1016/0011-7471(70)90043-4`.

Ragoasha, Natalie et al. (July 2019). "Lagrangian Pathways in the Southern Benguela Upwelling System". en. In: *Journal of Marine Systems* 195, pp. 50–66. ISSN: 0924-7963. DOI: `10.1016/j.jmarsys.2019.03.008`.

Rainville, Luc and Robert Pinkel (June 2001). "Wirewalker: An Autonomous Wave-Powered Vertical Profiler". In: *Journal of Atmospheric and Oceanic Technology* 18.6, pp. 1048–1051. ISSN: 0739-0572. DOI: `10.1175/1520-0426(2001)018<1048:WAAWPV>2.0.CO;2`.

Renault, Lionel, Alex Hall, and James C. McWilliams (Jan. 2016). "Orographic Shaping of US West Coast Wind Profiles during the Upwelling Season". en. In: *Climate Dynamics* 46.1-2, pp. 273–289. ISSN: 0930-7575, 1432-0894. DOI: `10.1007/s00382-015-2583-4`.

Richter, Ingo (2015). "Climate Model Biases in the Eastern Tropical Oceans: Causes, Impacts and Ways Forward". In: *Wiley Interdisciplinary Reviews: Climate Change* 6.3, pp. 345–358.

Robertson, Robin and Paul Hartlipp (Dec. 2017). “Surface Wind Mixing in the Regional Ocean Modeling System (ROMS)”. en. In: *Geoscience Letters* 4.1. ISSN: 2196-4092. DOI: `10.1186/s40562-017-0090-7`.

Rykaczewski, Ryan R. and David M. Checkley (Feb. 2008). “Influence of Ocean Winds on the Pelagic Ecosystem in Upwelling Regions”. en. In: *Proceedings of the National Academy of Sciences* 105.6, pp. 1965–1970. ISSN: 0027-8424, 1091-6490. DOI: `10.1073/pnas.0711777105`.

SAF, OSI (2018). *OSI-250L3C Hourly Sea Surface Temperature (GHRSST) Data Record Release 1 - MSG*. en. DOI: `10.15770/EUM_SAF_OSI_0004`.

Saha, Suranjana et al. (Jan. 2010). *NCEP Climate Forecast System Reanalysis (CFSR) Selected Hourly Time-Series Products, January 1979 to December 2010*. DOI: `10.5065/D6513W89`.

Shannon, L. V. (1985). “The Benguela Ecosystem Part 1: Evolution of the Benguela, Physical Features and Processes”. In: *Oceanographic and Marine Biology Annual Review* 23, pp. 105–182.

Shannon, L. V. and G. Nelson (1996). “The Benguela: Large Scale Features and Processes and System Variability”. en. In: *The South Atlantic: Present and Past Circulation*. Ed. by Gerold Wefer et al. Berlin, Heidelberg: Springer, pp. 163–210. ISBN: 978-3-642-80353-6. DOI: `10.1007/978-3-642-80353-6_9`.

Shchepetkin, Alexander F. and James C. McWilliams (Jan. 2005). “The Regional Oceanic Modeling System (ROMS): A Split-Explicit, Free-Surface, Topography-Following-Coordinate Oceanic Model”. en. In: *Ocean Modelling* 9.4, pp. 347–404. ISSN: 14635003. DOI: `10.1016/j.ocemod.2004.08.002`.

Shearman, R. Kipp (Feb. 2005). “Observations of Near-Inertial Current Variability on the New England Shelf”. en. In: *Journal of Geophysical Research: Oceans* 110.C2. ISSN: 2156-2202. DOI: `10.1029/2004JC002341`.

Shelton, P. A. and L. Hutchings (May 1982). “Transport of Anchovy, Engraulis Capensis Gilchrist, Eggs and Early Larvae by a Frontal Jet Current”. en. In: *ICES Journal of Marine Science* 40.2, pp. 185–198. ISSN: 1054-3139, 1095-9289. DOI: `10.1093/icesjms/40.2.185`.

Simpson, J. H. et al. (Jan. 2002). “Forced Oscillations near the Critical Latitude for Diurnal-Inertial Resonance”. en. In: *Journal of Physical Oceanography* 32.1, pp. 177–

187. ISSN: 0022-3670, 1520-0485. DOI: `10.1175/1520-0485(2002)032<0177:FONTCL>2.0.CO;2`.

Small, R. Justin et al. (2015). "The Benguela Upwelling System: Quantifying the Sensitivity to Resolution and Coastal Wind Representation in a Global Climate Model". In: *Journal of Climate* 28.23, pp. 9409–9432.

Smit, Albertus J. et al. (Dec. 2013). "A Coastal Seawater Temperature Dataset for Biogeographical Studies: Large Biases between In Situ and Remotely-Sensed Data Sets around the Coast of South Africa". en. In: *PLoS ONE* 8.12. Ed. by Inés Álvarez, e81944. ISSN: 1932-6203. DOI: `10.1371/journal.pone.0081944`.

Strub, P. T. et al. (June 1998). "Satellite Comparison of the Seasonal Circulation in the Benguela and California Current Systems". en. In: *South African Journal of Marine Science* 19.1, pp. 99–112. ISSN: 0257-7615. DOI: `10.2989/025776198784126836`.

Stuart-Menteth, Alice C., Ian S. Robinson, and Peter G. Challenor (May 2003). "A Global Study of Diurnal Warming Using Satellite-derived Sea Surface Temperature". en. In: *Journal of Geophysical Research: Oceans* 108.C5. ISSN: 2156-2202. DOI: `10.1029/2002JC001534`.

Taunton-Clark, J. (1985). "The Formation, Growth and Decay of Upwelling Tongues in Response to the Mesoscale Wind Field during Summer". In: *South African ocean colour and upwelling experiment*, pp. 47–61.

Tintoré, J. et al. (June 1995). "Near-Inertial Motions in the Coastal Ocean". en. In: *Journal of Marine Systems* 6.4, pp. 301–312. ISSN: 09247963. DOI: `10.1016/0924-7963(94)00030-F`.

Umlauf, L. and H. Burchard (Mar. 2003). "A Generic Length-Scale Equation for Geophysical Turbulence Models". en. In: *Journal of Marine Research* 61.2, pp. 235–265. ISSN: 15439542, 00222402. DOI: `10.1357/002224003322005087`.

Umlauf, Lars and Hans Burchard (May 2005). "Second-Order Turbulence Closure Models for Geophysical Boundary Layers. A Review of Recent Work". In: *Continental Shelf Research*. Recent Developments in Physical Oceanographic Modelling: Part II 25.7, pp. 795–827. ISSN: 0278-4343. DOI: `10.1016/j.csr.2004.08.004`.

Veitch, Jennifer, Pierrick Penven, and Frank Shillington (Sept. 2010). "Modeling Equilibrium Dynamics of the Benguela Current System". en. In: *Journal of Physical*

Oceanography 40.9, pp. 1942–1964. ISSN: 0022-3670, 1520-0485. DOI: `10.1175/2010JPO4382.1`.

Veitch, Jennifer A. and Pierrick Penven (2017). “The Role of the Agulhas in the Benguela Current System: A Numerical Modeling Approach”. en. In: *Journal of Geophysical Research: Oceans* 122.4, pp. 3375–3393. ISSN: 2169-9291. DOI: `10.1002/2016JC012247`.

Viljoen, A. and P. Monteiro (2004). *Development of an Operational Capacity for Real-Time Observation and Forecasting of Harmful Algal Blooms in the Benguela Current Large Marine Ecosystem Region: Utility of Models in Forecasting Harmful Algal Blooms*. Tech. rep. CSIR REPORT ENV-S-C 2004-066. Centre for Marine Studies, University of Cape Town.

Viljoen, Anel (2006). “Investigation of the Near-Shore Episodic Poleward Current in the Southern Benguela: A Numerical Modelling Approach”. Masters Thesis. University of Cape Town.

Walter, Ryan K. et al. (Feb. 2017). “Local Diurnal Wind-Driven Variability and Upwelling in a Small Coastal Embayment: LOCAL WIND-DRIVEN VARIABILITY”. en. In: *Journal of Geophysical Research: Oceans* 122.2, pp. 955–972. ISSN: 21699275. DOI: `10.1002/2016JC012466`.

Weeks, Sj et al. (Nov. 2006). “Remotely Sensed Variability of Temperature and Chlorophyll in the Southern Benguela: Upwelling Frequency and Phytoplankton Response”. en. In: *African Journal of Marine Science* 28.3-4, pp. 493–509. ISSN: 1814-232X, 1814-2338. DOI: `10.2989/18142320609504201`.

Weller, Robert A. (Oct. 1982). “The Relation of Near-Inertial Motions Observed in the Mixed Layer During the JASIN (1978) Experiment to the Local Wind Stress and to the Quasi-Geostrophic Flow Field”. en. In: *Journal of Physical Oceanography* 12.10, pp. 1122–1136. ISSN: 0022-3670, 1520-0485. DOI: `10.1175/1520-0485(1982)012<1122:TRONIM>2.0.CO;2`.

Williams, Charlotte et al. (Oct. 2013). “Wind-Driven Nutrient Pulses to the Subsurface Chlorophyll Maximum in Seasonally Stratified Shelf Seas: Wind-Driven Nitrate Fluxes”. en. In: *Geophysical Research Letters* 40.20, pp. 5467–5472. ISSN: 00948276. DOI: `10.1002/2013GL058171`.

Woodson, C. B. et al. (Nov. 2007). “Local Diurnal Upwelling Driven by Sea Breezes in Northern Monterey Bay”. en. In: *Continental Shelf Research* 27.18, pp. 2289–2302. ISSN: 0278-4343. DOI: `10.1016/j.csr.2007.05.014`.

Xing, Jiuxing, Alan M. Davies, and Philippe Fraunie (Jan. 2004). “Model Studies of Near-Inertial Motion on the Continental Shelf off Northeast Spain: A Three-Dimensional/Two-Dimensional/One-Dimensional Model Comparison Study”. In: *Journal of Geophysical Research: Oceans* 109.C1. ISSN: 0148-0227. DOI: `10.1029/2003JC001822`.

Xu, Zhigang (2002). *Ellipse Parameters Conversion and Velocity Profiles for Tidal Currents in Matlab*. Ocean Science Division, Fisheries and Oceans Canada. URL https://www.mathworks.com/ma Quebec, Canada.

Zhang, Xiaoqian et al. (Jan. 2010). “A Numerical Study of Sea-Breeze-Driven Ocean Poincare Wave Propagation and Mixing near the Critical Latitude”. en. In: *Journal of Physical Oceanography* 40.1, pp. 48–66. ISSN: 0022-3670, 1520-0485. DOI: `10.1175/2009JPO4216.1`.